AFRL-AFOSR-UK-TR-2019-0029

Aeroservoelastic Optimization of Aircraft Wings with Load Alleviation Systems

Andrew Wynn
IMPERIAL COLLEGE OF SCIENCE TECHNOLOGY & MEDICINE
EXHIBITION RD
LONDON, SW7 2BT
GB

05/31/2019
Final Report

DISTRIBUTION A: Distribution approved for public release.

Air Force Research Laboratory
Air Force Office of Scientific Research
European Office of Aerospace Research and Development
Unit 4515 Box 14, APO AE 09421

REPORT DOCUMENTATION PAGE	*Form Approved* *OMB No. 0704-0188*

The public reporting burden for this collection of information is estimated to average 1 hour per response, including the time for reviewing instructions, searching existing data sources, gathering and maintaining the data needed, and completing and reviewing the collection of information. Send comments regarding this burden estimate or any other aspect of this collection of information, including suggestions for reducing the burden, to Department of Defense, Executive Services, Directorate (0704-0188). Respondents should be aware that notwithstanding any other provision of law, no person shall be subject to any penalty for failing to comply with a collection of information if it does not display a currently valid OMB control number.
PLEASE DO NOT RETURN YOUR FORM TO THE ABOVE ORGANIZATION.

1. REPORT DATE *(DD-MM-YYYY)* 31-05-2019	**2. REPORT TYPE** Final	**3. DATES COVERED** *(From - To)* 01 Mar 2014 to 28 Feb 2018

4. TITLE AND SUBTITLE Aeroservoelastic Optimization of Aircraft Wings with Load Alleviation Systems	**5a. CONTRACT NUMBER**
	5b. GRANT NUMBER FA9550-14-1-0055
	5c. PROGRAM ELEMENT NUMBER 61102F
6. AUTHOR(S) Andrew Wynn, Rafael Palacios	**5d. PROJECT NUMBER**
	5e. TASK NUMBER
	5f. WORK UNIT NUMBER
7. PERFORMING ORGANIZATION NAME(S) AND ADDRESS(ES) IMPERIAL COLLEGE OF SCIENCE TECHNOLOGY & MEDICINE EXHIBITION RD LONDON, SW7 2BT GB	**8. PERFORMING ORGANIZATION REPORT NUMBER**
9. SPONSORING/MONITORING AGENCY NAME(S) AND ADDRESS(ES) EOARD Unit 4515 APO AE 09421-4515	**10. SPONSOR/MONITOR'S ACRONYM(S)** AFRL/AFOSR IOE
	11. SPONSOR/MONITOR'S REPORT NUMBER(S) AFRL-AFOSR-UK-TR-2019-0029

12. DISTRIBUTION/AVAILABILITY STATEMENT
A DISTRIBUTION UNLIMITED: PB Public Release

13. SUPPLEMENTARY NOTES

14. ABSTRACT

To aid in the investigation of new simultaneous optimisation strategies for flexible vehicles and their control systems, a two-dimensional aerofoil optimisation which demands minimal computational effort is studied. Although computationally simple, the design allows for optimisation over multiple disciplines: the structure can be designed by varying the stiffness of supporting springs; the control architecture through weightings in a LQR controller; the observer by means of the placement of pressure sensors; and the aerodynamics via the shaping of the compliant trailing edge. Optimising over all these fields simultaneously is compared to a sequential methodology of optimising the open-loop characteristics first and subsequently
adding a closed-loop controller. Parametrisation of the design vector and variable selection often require user input and are fixed during optimisation. Our research aims to automate this process. Furthermore, we investigate whether varying the parametrisation and number of design variables during the optimisation can lead to improvements in the final design.
This parametrisation is shown to make the optimisation more robust with respect to the initial design, and facilitate an automated variable selection methodology. This variable selection allows for the dimension of the problem to be reduced temporarily and it is shown that this makes the optimisation more robust. The second half of the work focuses on the
derivation of a cantilever model. The model consists of a geometrically-nonlinear, slenderbeam described by a one-dimensional reference line that can deform in three-dimensional space; a two-dimensional, potential flow model defined over the span of the beam; and trailing edge flaps that can vary in size and position. The intrinsic beam formulation is chosen as it results in equations of motion with at most quadratic nonlinearities, which

15. SUBJECT TERMS
EOARD, Aeroservoelastic, Design optimization

16. SECURITY CLASSIFICATION OF:			**17. LIMITATION OF ABSTRACT**	**18. NUMBER OF PAGES**	**19a. NAME OF RESPONSIBLE PERSON** GARNER, DAVID
a. REPORT	**b. ABSTRACT**	**c. THIS PAGE**			
Unclassified	Unclassified	Unclassified	SAR		**19b. TELEPHONE NUMBER** *(Include area code)* 011-44-1895-616021

Standard Form 298 (Rev. 8/98)
Prescribed by ANSI Std. Z39.18

Imperial College London
Department of Aeronautics

Design Optimisation of Controlled Aeroelastic Aerofoils and Wings

Jacob James Broughton-Venner

This thesis is submitted for the degree of Doctor of Philosophy
and the Diploma of Imperial College London
October 2018

Declaration

I hereby declare that I am the author of this thesis, and that it is the product of my own work. This dissertation has not been submitted for consideration towards any other degree or award. Where appropriate, I have fully acknowledged the ideas and results from the work of other people.

The copyright of this thesis rests with the author and is made available under a Creative Commons Attribution Non-Commercial No Derivatives licence. Researchers are free to copy, distribute or transmit the thesis on the condition that they attribute it, that they do not use it for commercial purposes and that they do not alter, transform or build upon it. For any reuse or redistribution, researchers must make clear to others the licence terms of this work.

Jacob James Broughton-Venner

Mathematicians may flatter themselves that they possess new ideas which mere human language is yet unable to express. Let them make the effort to express these ideas in appropriate words without the aid of symbols, and if they succeed they will not only lay us laymen under a lasting obligation, but, we venture to say, they will find themselves very much enlightened during the process, and will even be doubtful whether the ideas as expressed in symbols had ever quite found their way out of the equations of their minds.

James Clerk Maxwell

Acknowledgements

I have been privileged that I had not one but two acutely attentive supervisors, Dr. Andrew Wynn and Dr. Rafael Palacios, throughout this degree. Both have given immeasurable guidance, imparted tremendous knowledge and have been an utter pleasure to work with over the years.

Andy was also the supervisor to my Masters project and hence has endured hundreds of weekly meetings with me to date. The positivity with which he approached each one was always noticed and always appreciated. In all my works Andy has offered substantial corrections and suggestions. Writing has never been a strong point of mine, but I had hoped that over the course of 5 years my first drafts would return from Andy with fewer corrections. They have not. Being optimistic this implies that the rate of improvement in my writing is equal to Andy's rate of improvement in correcting my writing.

Rafa has been an outstanding mentor not only for this degree but in a wider sense. He has given invaluable advise on academia in general and specifically helped me finding my next position. I have always felt that I could go to Rafa for advise on anything be it personal, academic or professional. Rafa's unwavering positivity and caring nature has always impressed even in the midst of having a new born baby he would consistently lighten the mood of the room.

To my mum, Tania Broughton, to who I owe the most in life. For each year I mature the more I come to appreciate how much you have sacrificed for me. You have always supported me in the way you thought best. Not only have you provided me with roof and been there as a mother throughout this degree (and my whole life) but you have been a close friend.

Confined to one page I could not possibly thank all those who have made this possible, however, I will end thanking a few who have directly affected my education. To my grandmother, Lois Edwards, who supported me through my masters, my high school maths teacher Sharon Pawsey, and Jim Cramp, thank you all!

Further acknowledgements go to the funders of this project the European Office of Aerospace Research and Development (EOARD) Grant number FA9550-14-0055.

Abstract

To aid in the investigation of new simultaneous optimisation strategies for flexible vehicles and their control systems, a two-dimensional aerofoil optimisation which demands minimal computational effort is studied. Although computationally simple, the design allows for optimisation over multiple disciplines: the structure can be designed by varying the stiffness of supporting springs; the control architecture through weightings in a LQR controller; the observer by means of the placement of pressure sensors; and the aerodynamics via the shaping of the compliant trailing edge. Optimising over all these fields simultaneously is compared to a sequential methodology of optimising the open-loop characteristics first and subsequently adding a closed-loop controller. Parametrisation of the design vector and variable selection often require user input and are fixed during optimisation. Our research aims to automate this process. Furthermore, we investigate whether varying the parametrisation and number of design variables during the optimisation can lead to improvements in the final design. This parametrisation is shown to make the optimisation more robust with respect to the initial design, and facilitate an automated variable selection methodology. This variable selection allows for the dimension of the problem to be reduced temporarily and it is shown that this makes the optimisation more robust. The second half of the work focuses on the derivation of a cantilever model. The model consists of a geometrically-nonlinear, slender-beam described by a one-dimensional reference line that can deform in three-dimensional space; a two-dimensional, potential flow model defined over the span of the beam; and trailing edge flaps that can vary in size and position. The intrinsic beam formulation is chosen as it results in equations of motion with at most quadratic nonlinearities, which is exploited for deriving analytic derivatives. These derivatives are used to demonstrate how adjoint-based methods can accelerate aeroelastic calculations.

https://www.overleaf.com/project/5c39e68aafe81053a81f59f5

Contents

Acknowledgements **7**

Abstract **7**

1 Introduction **25**

1.1 Literature Review 31

1.1.1 Aeroservoelastic modelling of flexible aircraft 32

1.1.2 Optimisation 39

1.1.3 Optimisation of Aeroservoelastic Systems 42

1.2 Open Research Questions 44

1.3 Thesis Outline 46

1.4 Publications based on this work 50

2 Aeroservoelastic Optimisation 51

2.1 Aeroservoelastic Problem Description 51

2.2 Optimisation Problem Description 55

2.2.1 Design Vector 55

2.2.2 Objective function and Constraints 59

2.3 Simultaneous and Sequential Optimisation Strategies 61

2.4 Parametrisation and Variable Selection 64

2.4.1 Reduced order methods 64

2.4.2 Proper Orthogonal Decomposition 64

3 Two Dimensional Aeroservoelastic Model 68

3.1 Aeroelastic Model 69

3.1.1 Deformation Representation 70

3.1.2 Pressure 71

3.1.3 Non-Circulatory Potential 72

3.1.4 Circulatory Potential 74

3.1.5 Aerodynamic States 77

3.1.6 Forces and Moments 78

3.1.7 Heave Motion and Pitch Motion 79

3.1.8 Compliant aerofoil structural model 80

3.1.9 Open-loop State-Space form 82

3.2 Aeroservoelastic Model 83

3.2.1 Trailing edge state 83

3.2.2 Mass distribution 86

3.2.3 Controller and Observer 87

3.2.4 Model Parameters 88

3.3 Optimisation 89

3.3.1 Design variables 89

3.3.2 Cost function 90

3.3.3 Constraints 91

3.4 Optimisation Implementation 93

3.4.1 Solution method 93

3.4.2 Optimisation acceleration 94

4 Design Optimisation of an Aeroservoelastic Aerofoil 96

4.1 Model Verification 97

4.2 Structural Optimisation 98

4.2.1 Constraints for Closed-Loop Performance 102

4.3 Aeroservoelastic Design Optimisation 108

4.3.1 Simultaneous and Sequential Optimisation Strategies 108

4.3.2 Physical interpretation of the optimal results 113

4.3.3 Parametrisation 113

4.3.4 Variable Selection 115

4.4 Concluding Remarks 117

5 Cantilever Model 120

5.1 Structural Model 121

5.2 Aerodynamic Model 123

5.3 Linearisation 126

5.4 Gust Model 129

5.5 Flap Input 130

5.6 Galerkin Projection 131

5.6.1 Linear Normal Modes 131

5.6.2 Aerodynamic states 133

5.6.3 State-Space Formulation 134

5.7 Concluding Remarks 138

6 Adjoint-based Optimisation 140

6.1 Derivatives 141

6.2 Equilibrium Under Constant Aerodynamic Forcing 147

6.2.1 Sensitivity of $\boldsymbol{x}_2(L)$ to $\boldsymbol{x}_2(0)$ 150

6.2.2 Nonlinear equilibrium evaluation 154

6.3 Concluding Remarks 155

7 Cantilever Model Results 156

7.1 Validation 156

7.1.1 Model Inputs 156

7.1.2 Linear Stability Analysis of the Goland Cantilever Wing 159

7.1.3 Time domain solutions with gust input 161

7.1.4 Adjoint-based validation 164

7.2 Acceleration from Adjoint-Based Method 166

7.3 Concluding Remarks 169

8 Conclusion 170

8.1 Summary 170

8.2 Significant Contributions 175

8.3 Recommendations for Future Work 179

8.3.1 Continued exploration of POD based optimisation strategies 180

8.3.2 Design optimisation of cantilever model 181

Bibliography 182

Appendices 200

A Transfer function from gust input to flap input 201

List of Tables

3.1 Remaining model parameters. 89

4.1 Relative errors (in percentage) from sequential to simultaneous optimisations. 109

4.2 Relative error (as a percentage) from the original basis optimisations to the POD rotated optimisations and original basis optimisations to the reduction method. 116

7.1 Inputs to the aeroelastic model. 157

7.2 Structural properties required. 158

7.3 Required inputs that are fixed for the remainder of this work. 158

7.4 Inputs used for the Goland wing validation. 159

7.5 Flutter velocity and frequency for the Goland wing with $n_{mo} = 8$ and $n_{sp} = 60$. 160

7.6 Input exceptions for Section 7.1.3. 161

7.7 Time differences between time-domain method and adjoint-based method. . . 168

List of Figures

1.1 Concept aircraft that are attempting to attenuate large deflections of high-aspect-ratio wings. 29

1.2 Comparison between the X-HALE project and the NASA Helios aircraft. . . . 30

1.3 Aerodynamic modelling used in aeroservoelasticity. 33

2.1 Definition of Γ as the intersection of the fluid domain $\Omega_{\mathcal{F}}$ and structural domain $\Omega_{\mathcal{S}}$. 52

2.2 Open-loop aeroelastic system with input $\boldsymbol{u}$ and output $\boldsymbol{z}$. 53

2.3 Aeroservoelastic model made from connecting the system in Figure 2.2 to a feedback-controller $\mathcal{K}(\boldsymbol{y})$. 55

2.4 Examples of *engineering variables* for a cantilever wing. 56

2.5 Example of different parametrisation choices. Top: mass variation at discrete wing locations and linear interpolation between known values. Bottom: three mass shape functions and the corresponding mass distributions $m(s) = \sum_{i=1}^{3} m_i(s)$. 57

3.1 Visualisation of aerofoild model. 69

3.2 Definition of the trailing edge shape and its physical meaning. 85

4.1 Non-dimensional flutter speed, $V_f/\left(b\omega_\alpha\right)$ against a non-dimensionalised hinge spring frequency, $\omega_\beta/\omega_\alpha$ for a flat plate, flat flap camberline model. The current code is compared to results from [131]. 98

4.2 (a) Convergence of gradient-based optimisation trajectories to minimize $\omega_\alpha^2 + \omega_y^2$ subject to a flutter constraint with $\omega_\beta = 5$. (b) Neighbourhood of the global minimum its basis of attraction (light-gray area). 100

4.3 (a) Convergence of trajectories through three-dimensional design space and the feasible set corresponding to $\omega_\beta = 14$ (dashed lines). (b) Value of ω_β for the optimisation trajectories identified in (a) 101

4.4 Heave response and control input under a "$1 - \cos$" disturbance, with and without control saturation. 103

4.5 The effect of constraining $\|T_{wu}\|_\infty$: percentage of converged designs (dashed line) satisfying the time-domain performance metric; and mean value $\bar{f}$ of metric for converged designs (with standard errors). 105

4.6 Feasible regions of a 2D slice (left) and zoomed area (right). Colour indicates design is feasible for neither (dark grey), one (light grey) or both (white) values of $C_2 = 1, 10$. 106

4.7 Iteration paths from numerous close initial conditions from a sequential method, blue, and a simultaneous method, green. The final design points of the simultaneous method are marked with dark green circles. A convex hull has been plotted around these points along with its projections in the $\omega_y - \omega_\alpha$, $\omega_\alpha - \omega_\beta$ and $\omega_y - \omega_\beta$ planes. 111

4.8 Closed-loop responses of aerofoils with the same design vector but varied centre of gravity and $V_\infty = 4.5\, ms^{-1}$. Centre of gravity is displaced a distance equal to 5% of the chord towards the tail in Tail Heavy case and displaced the same distance towards the nose for the Nose Heavy case. 114

4.9 The lowest cost function found from each method, normalised by the lowest found by the training set with $\epsilon = 1 \times 10^{-8}$ and shown for a range of values for the training set stopping condition ϵ. 114

4.10 Fraction of variance Λ described by a subset of $d - r$ POD basis vectors. . . . 116

4.11 Percentage difference between the final designs from the original basis and Reduction method with $X = [\omega_y,\, \omega_\alpha,\, \omega_\beta,\, Q_y,\, Q_\alpha,\, s_2,\, s_3,\, p_1,\, p_2,\,]^\top$ 117

5.1 Definition of the global frame $[\boldsymbol{e}_x, \boldsymbol{e}_y, \boldsymbol{e}_z]^\top$ and local frame $[\boldsymbol{e}_1, \boldsymbol{e}_2, \boldsymbol{e}_3]^\top$. 122

7.1 Root locus of the linear Goland wing with $n_{mo} = 8$ and $n_{sp} = 60$. Free-stream velocity from $5ms^{-1}$ to $150ms^{-1}$ in $5ms^{-1}$ increments. 160

7.2 Tip displacement of the Long-Goland wing due to gust input described in (7.3), with $L_{GU} = 20\,m$ and $w_0 = 17.07\,ms^{-1}$. The blue line is the current implementation and the red line is taken from Figure 11 by Simpson et al. [62]. 162

7.3 Root strains of the Long-Goland wing due to gust input described in (7.3), with $L_{GU} = 20\,m$ and $w_0 = 17.07\,ms^{-1}$. The blue line is the current implementation and the red line is taken from Figure 12 by Simpson et al. [62]. 162

7.4 Steady state displacement in the $\boldsymbol{e}_3$ direction over the span of Long-Goland wing due to the control surface defined in (7.1.4) with deflection β. 165

7.5 Steady state displacement in the $\boldsymbol{e}_3$ direction over the span of the Long-Goland *wing-1* and *wing-2*. 167

7.6 Elastic energy across *wing-1* given a flap deflection β in degrees—normalised by U_0 the elastic energy that occurs with $\beta = 10°$. 168

Chapter 1

Introduction

The field of AeroServoElasticity (ASE) is concerned with the mathematical modelling and control of interactions between the disciplines of aerodynamics, structural dynamics and rigid body mechanics and is especially important in the modelling of flexible aircraft. Neglecting these interactions in the design of flexible aircraft can, and historically has proven to, lead to at best undesirable consequences — such as reduced control effectiveness, explained in Section 1.1.1 — and at worst instability and structural failure. Cases of catastrophic failure with flexible aircraft are numerous and well known, for example, the 2004 NASA Helios prototype developed an excessive dynamic response, leading to structural failure, due to a gust eliciting an unexpected wing configuration. The subsequent investigative report highlighted the need for: *...more advanced multidisciplinary (structures, aeroelastic, aerodynamics, atmospheric, materials, propulsion, controls, etc.) "time-domain" analysis methods appropriate to highly flexible, morphing, vehicles and procedures to control wing dihedral in flight* [1].

Historically ASE considerations were not needed as early aircraft designs tended to be relatively stiff — characterised by over-sized, stiff structures [2] and heavy materials — this allowed uncertainties and aeroelastic effects to be ignored during modelling and design [3]. However, early designs did not shy from the use of active control systems. The use of sensors on an aircraft to feed back information to a control system that can automatically regulate lifting surfaces to alter the dynamics has been an active research topic for over 70 years [4]. Not only have controllers been used to change the dynamic behavior of aircraft but they have made it possible to fly inherently unstable aircraft such as the General Dynamics F-16, which first flew in 1974 [5]. However, such dramatic reliance on the controllers is extremely rare outside of military applications, due to regulations on aircraft safety.

There are multiple objectives one could have when designing an aircraft, for example one could desire: speed, maneuverability or a long lifespan. Another commonly sought attribute is *efficiency*, a term we will use in a general sense to avoid highly design specific goals. Instead, we use *efficiency* to group together several objectives such as: minimising fuel needed for a specific mission profile; maximising an aircraft's range; or maximising the length of time an aircraft can stay aloft. These objectives might be subtly different but their design solutions often share similar characteristics.

Progress towards more efficient aircraft has been made since the aforementioned early designs, streamlining the over-stiffening and over-sizing, enabling the production of lighter aircraft with each new generation. For example, the Boeing 787 Dreamliner was one of the first commercial aircraft to construct the airframe primarily from composite materials, contributing to approximately a 50% reduction in total structural weight, relative to previous generations. The manufacture claimed that this, among other design features — such as more economical engines — was able to reduce operational cost and CO_2 emissions. However, weight reduction and engine economy are not the only ways to increase efficiency: major gains are possible by improving aerodynamic efficiency [6], which is normally quantified using the *lift-to-drag ratio* of the aircraft. Creating lift requires lifting surfaces, thus, is indirectly constrained by weight. Increasing aerodynamic efficiency can instead be thought as pursuing a reduction in drag. An estimate of the drag coefficient C_D of an aircraft can be made via the drag polar equation [7], which can be reduced to

$$C_D - C_{D_0} \propto \frac{C_L^2}{AR}, \tag{1.1}$$

where C_{D_0} is the zero-lift-drag coefficient — a function of profile, friction and pressure drag on all the aircraft parts, for example, the engines, fuselage and landing gears — C_L is the lift coefficient and AR is the wing aspect ratio, i.e. the ratio of wing length to the mean chord length. Thus, increasing aspect ratio decreases drag and is a key characteristic when seeking ever more efficient aircraft. This is evident when looking at commercial jet designs over time, where one can see an increase in aspect ratio, either by increased wingspan or by the addition of wingtip devices [8]. Current examples of high-aspect-ratio commercial jets include the Airbus A320 and the Boeing 747. A more extreme example of a manned long-endurance aircraft is the SolarStratos: a two-seater solar aircraft with a wingspan of $24m$, weight of $450kg$ and a planned endurance of more than 24 hours. Yet, manned aircraft are heavily constrained by current aviation regulations, impeding the progress towards more efficient aircraft. For example, it has long been known that Active Flutter Suppression (AFS) has the potential for major weight savings [9], but agencies such as the European Aviation Safety Agency (EASA) restrict the use of AFS on commercial manned aircraft. However, the safety margins for unmanned aircraft do not restrict the design space as much and as such far greater endurance has been seen in unmanned aerial vehicles (UAVs).

Classically UAVs have predominately be used in military settings, either for weapon or reconnaissance based platforms. Notable platforms in the military market include: the

Global Hawk — with over 100,000 hours flown above combat zones, a record endurance of over 33 hours and a wingspan of $35.4m$; and the Phantom Eye — a liquid hydrogen powered UAV, with a wingspan of $46m$ and a 4 days (at $20km$) endurance goal. Recently as the accessibility and reliability of commercial UAVs comes to fruition the civilian use of UAVs has become more common. For example, the telecoms market (including Google, Facebook and Vodafone) has made investments into long-endurance UAVs. The telecoms industry has seen an impressive rate of growth in the past decade. Mobile data traffic has grown 18-fold over the past 5 years with almost half a billion mobile devices and connections added in 2016 [10]. Telecommunication companies aim to further perpetuate growth by using UAVs, reaching customers in remote areas where the logistics or costs of setting up traditional communication networks are prohibitory. One of the platforms closest to market is the commercially-available Airbus Zephyr, a solar powered UAV capable of altitudes of up to $22.5km$, and a record of over 14 days of continuous flight without refueling.

Longer endurance can also be made possible by flying at higher altitudes. The Global Hawk, Phantom eye, and the Zephyr are all examples of High-Altitude Long-Endurance (HALE) aircraft. At altitudes of over $20km$ the air density is less than 10% that at sea level, which greatly reduces drag. Moreover, the higher altitude is an enticing vantage point for both surveillance and communication. Furthermore, wind and gusts are less extreme and more predictable at these altitudes [11]. However, lower air density also causes a decrease in lift. To overcome this a larger wing area is required, and coupled with the desired high-aspect-ratio can lead to large wing bending moments. Combined with the goal of low structural weight typically produces flexible aircraft designs that can suffer from large wing deflections. Attempts to reduce the deflection of high-aspect-ratio, low-weight aircraft have included braced or joined-wing concepts. For example, the truss-braced wing concept of the SUGAR Volt hybrid aircraft Figure 1.1a and the joined wing Lockhead Boxwing concept Figure 1.1b.

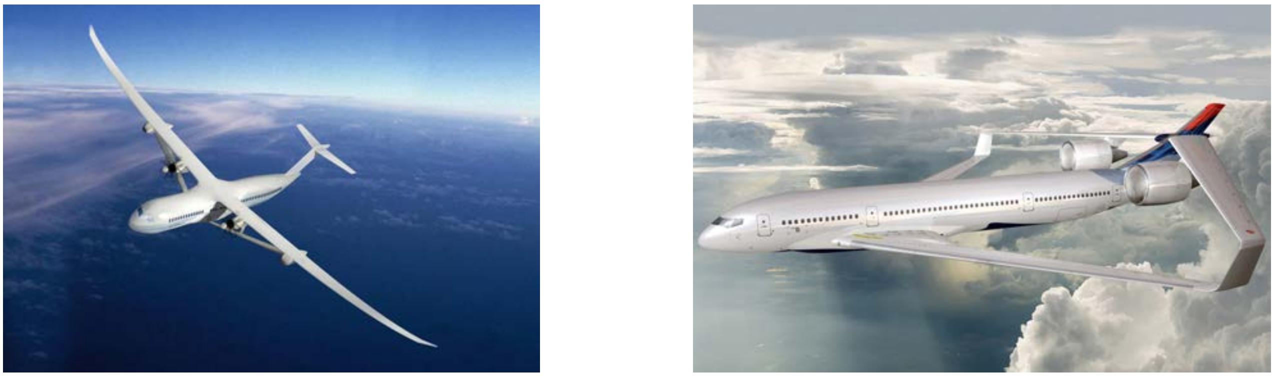

(a) SUGAR Volt hybrid
Image credit: Boeing

(b) Lockhead Boxwing
Images credit: Lockhead

Figure 1.1: Concept aircraft that are attempting to attenuate large deflections of high-aspect-ratio wings.

These concepts may be promising for large transport platforms that require a fuselage for passengers and/or payloads. However, HALE UAVs tend to have small, if any, fuselages meaning that designs with flexible wings are typically considered.

With stiffer structures it can be adequate to use linear structural models that linearise the structural dynamics around the cruising conditions. As one considers more flexible aircraft, new nonlinear effects become pronounced. The most obvious are the geometric-nonlinearities due to the large deflections of the wing [12]. Another phenomenon that has been observed is strong coupling between bending modes of the wing and the flight dynamic modes [13]. This occurs as the natural frequencies of the wings decrease (lower natural frequencies are associated with more flexible wings) and become comparable to the natural frequencies of the flight dynamics. Regardless of where, when or how nonlinearities become significant, greater accuracy can be expected from using a time-domain formulation instead of a frequency-domain formulation [14]. The importance of nonlinearities in flexible aircraft greatly increases the need for more sophisticated models which are typically more computationally demanding. Access to the required mathematical and computational tools has only become available in the past decade or two [15]. However, at present the literature

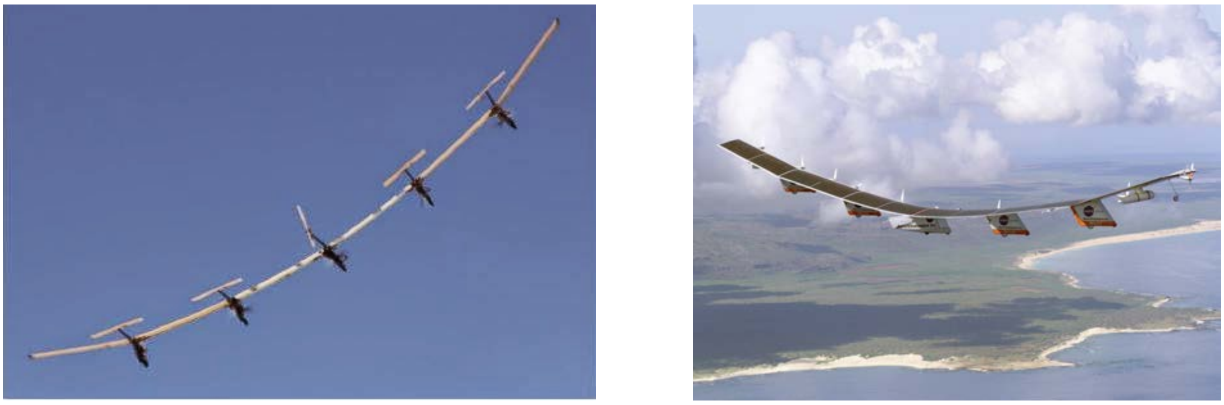

(a) X-HALE
Image credit: University of Michigan

(b) NASA Helios
Images credit: NASA

Figure 1.2: Comparison between the X-HALE project and the NASA Helios aircraft.

has reached a point in which the mathematical and computation tools have outgrown what has been tested and hence lacks practical validation. Cesnik et al. [16] states: *...there has been no validation of the integrated solution that brings the coupling effects between nonlinear aeroelasticity and flight dynamics, since no data is available for such an exercise.* This is why Cesnik et al. have made an effort to design an Experimental HALE (X-HALE) aircraft Figure 1.2a as a platform to collect such data. Note the similarities with the NASA Helios Figure 1.2b.

The design of a flexible aircraft requires several processes including, but not limited to: wind tunnel testing, manufacturing logistics, flight testing, concept design and Multidisciplinary Design Optimisation (MDO) — the focus of this work. Design optimisation is the field that aims to improve, with respect to merits defined in a cost-function, current designs via mathematical modelling and optimisation techniques. MDO is concerned about applying design optimisation to designs that possess multiple distinct sub-disciplines, for example, an aeroservoelastic flexible aircraft model has at least three interacting sub-disciplines: aerodynamics, structural mechanics and control theory. Clearly advances in optimisation techniques have a direct effect on the ability to design increasingly more efficient aircraft. A recent example of this is the purported $1000kg$ worth of weight savings from using a tool called topology optimisation, discussed in Section 1.1.2, in the design of the Airbus A380 [17].

Although the tools to model flexible aircraft have been available for a number of years, the design of such aircraft requires many evaluations of said models — demanding substantially more computation power than is typically available. Hence, using the most sophisticated models, discussed in Section 1.1.1, in the design process is still not feasible and is very rarely performed in practice. One purpose of this thesis is to accept that current computational power means the latest modelling techniques are infeasible for the design of flexible aircraft so instead seeks and tests, on simple models, mathematical techniques that may lessen the computational burden.

1.1 Literature Review

Design optimisation of controlled aeroelastic systems is a research interest that spans many topics. We characterise this research interest into the disciplines of aerodynamics, structural mechanics, control theory and optimisation. Each on of these disciplines can be acknowledged as a separate and principle research area. As such, this literature review initially considers these research areas independently before ending with a review of the combined subject—optimisation of aeroservoelastic systems.

1.1.1 Aeroservoelastic modelling of flexible aircraft

Unsteady aerodynamics

There are numerous ways aerodynamic forces can be modelled and, although we introduce the techniques separately here, it is not uncommon for a mixture of techniques to be used on the same model or in different stages in the design process. The highest fidelity method is Direct Numerical Simulation (DNS) of the full Navier-Stokes equations [18]. DNS demands significant computational effort since it requires a relatively fine mesh to resolve turbulent flow. In theory, DNS methods can predict all aerodynamic non-linearities including phenomena, such as shock-induced boundary-layer separation [19], that can cause Limit Cycle Oscillations (LCO) [20]. LCO's or their considerations are common in flexible aircraft, hence, having an ASE model that demonstrates LCO's is useful in our context of designing HALE aircraft. Improvements in computational efficiency can be made without significant compromise of the simulation accuracy by using Large-Eddy Simulation (LES) [21]. LES calculates the largest eddies directly then uses turbulence models of the smaller scales. However, due to the intense computational requirements of DNS and LES methods they are very rarely used in aeroelastic models. Instead, they are used in only small, non-dynamic segments, e.g. aerofoil shape optimisation [22], noise reduction optimisations [23] or for validating simpler codes and methods. For the remainder of this Section the methods depicted in Figure 1.3, which are commonly used in aeroelastic models, are described.

Often when designing, especially on a system wide aircraft level, compromises with the level of fidelity in the aerodynamic model must be made so that simulations are quick enough for an optimisation. Larger systems, for example a full wing design, are only computationally feasible if less costly methods, such as a Reynolds-averaged Navier-Stokes (RANS) method

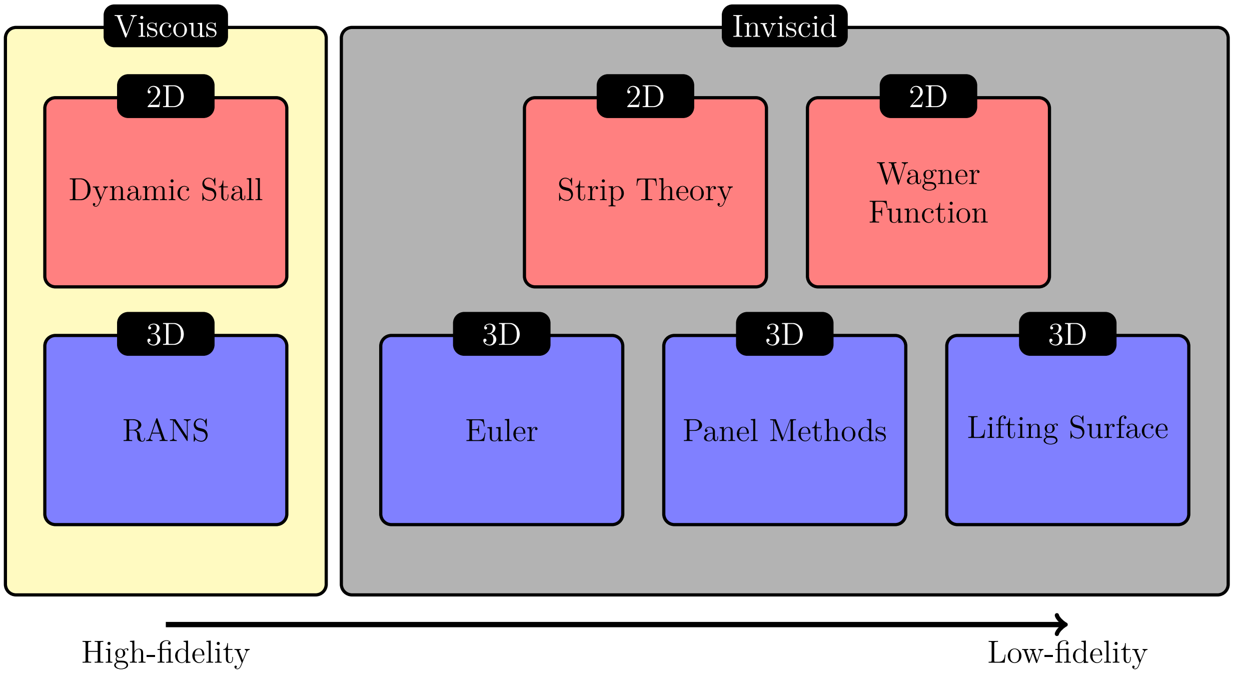
Viscous
2D
Dynamic Stall
3D
RANS
Inviscid
2D
Strip Theory
2D
Wagner Function
3D
Euler
3D
Panel Methods
3D
Lifting Surface
High-fidelity
Low-fidelity

Figure 1.3: Aerodynamic modelling used in aeroservoelasticity.

[24], are employed. RANS methods [25] simplify the Navier-Stokes equation by averaging, in time, the turbulent parts of the flow. The turbulent parts are then modelled by semi-empirical formulae. Furthermore, RANS methods retain all the viscous terms, hence, can capture moderate flow separation and thus aerodynamic stall [26]. Models that account for stall will often exhibit LCO in certain flight envelopes [27]. This can be due to stall limiting the amplitude of unstable oscillations. Another method considered high fidelity is the solution to the Euler equations [28]. The Euler equations describe inviscid, compressible and rotational flows. They can also be linearised around a mean flow which can be useful for flutter calculations. Note that flutter calculations are extremely common in aircraft modelling and design, as flutter instabilities can cause sudden and catastrophic failure of aircraft. Although aeroelastic modelling with RANS and Euler methods is not uncommon [29] they tend not to be used for ASE optimisation, at least for full aircraft models, due to being too computationally expensive.

The last of the methods to be described that can model three-dimensional effects are Panel [30] and Lifting-surface methods [31]. Panel methods are techniques for solving incompressible, inviscid potential flow over thick 2D and 3D geometries. Geometries are discretised into vortex sheets which give rise to circulation and hence lift. The main advantage of panel methods compared to lifting-surface methods is that thickness effects can be used in the calculation of profile drag. However, stream-wise motion and hence drag has minimal effect in aeroelastic calculations [32]. Lifting-surface methods are useful for gust response and dynamic stability of flexible aircraft [33]. In particular, they can give accurate results for HALE aircraft at low speeds with attached flow, where viscous effects are small. The Doublet Lattice Method (DLM) [34] is frequently used in industry for linear subsonic aeroelasticity. This method assumes that the wake is flat and convected downstream at the constant free-stream velocity. However, DLM does not capture in-plane motion sufficiently to be used, for example, in the analysis of T-tail flutter [35]. Moreover, the flat wake does not capture phenomenon such as wake roll up. The Vortex Lattice Method (VLM) [36], another lifting-surface method, is capable of modelling in-plane motion. This is accomplished with the use of vortex panels and horse-shoe vortices. One can extend the VLM to the Unsteady Vortex Lattice Method (UVLM) [37]. The UVLM is a time-domain method and models the wake to be free, i.e. the wake is convected with the local flow velocity. Hence, it can model wake roll up or interaction between the wake and other surfaces. A phenomena called wing rock [38] can be captured using UVLM, wing rock has been shown to induce LCOs [39]. Lifting-surface methods are reviewed in [40], where it is also shown that they can be reduced to a finite state space form. This is highly compatible with the design of active control systems and for dynamic time domain analysis. Recently, UVLM has been used extensively for fully coupled aircraft flight dynamics and aeroservoelastic models [41, 42, 43].

Finally, we discuss two-dimensional methods. Strip theory [44] splits the wing into finite portions and a two-dimensional potential flow is calculated for each section. The sections can then be integrated over the span of the wing. Two-dimensional flow cannot predict three-dimensional phenomena such as tip effects. However, tip effects become negligible for high-aspect-ratio wings, and thus, many HALE aircraft models have used strip theory [45, 46, 47]. Although possible, it is difficult to include aerodynamic coefficient calculations or stall models with UVLM. Whereas, two-dimensional flows around aerofoils are well documented allowing for semi-empirical corrections to be made. Tip and stall corrections are possible with Peters' [48] induced flow model, a finite state model which uses the aerodynamic data of the wing cross-sections. Two-dimensional stall models that are still in use include the ONERA [49] and Beddoes-Leishman [50] methods. The lowest fidelity models simply use the rational function approximations and state-space fitting methods of Theodorsen [51] and Wagner [52]. These are capable of modelling unsteady, inviscid aerodynamic forcing on thin aerofoils up to small angles.

Structural Dynamics

Typically, it is the solution to the aerodynamics that dictates the computational time required for simulating aeroelastic problems. The level of fidelity of the structural model has limited consequences on the coupled analysis. Hence, structural modelling decisions tend to be problem specific as opposed to restricted by computational time. Structural analysis require first a kinematic assumption, for example assuming a structure can be modelled as one-dimensional beam, then a discretisation scheme. Geometrically-Exact Beam Models (GEBM) can be used to describe geometrically non-linear, three-dimensional dynamics of a reference line, depicted in Figure **??**. Non-linear beam theories have been used to model helicopter blades [53], large wind turbine blades [54] and high-aspect-ratio wings [55]. Beam theory, typically uses deflections and rotations as primary variables. However, finite rotations can lead to large errors when integrated over. Instead, some alternative formulations known as intrinsic theory use velocities and strains as primary variables [56]. The disadvantage of these primary variables is the need to integrate velocities if displacements are required. Palacios et al [57] review the use of different primary variables on a flexible aircraft model. Even though beams can model three-dimensional dynamics, they themselves are predominantly one-dimensional objects and hence lack the ability to model chord and thickness effects.

Structural solutions are typically based on Finite Element (FE) methods, which are not restricted to one-dimensional formulations. Geometries are discretised into a finite number of sections. Local equations for each section are integrated over, with variational methods, to give the global properties of the structure. FE methods have been used extensively in the modelling of aircraft [58, 59, 60] and are common in industry. Hodges produced a review of composite rotor blade modelling that includes a discussion on FE based approaches [61].

Numerous software packages now exist that are capable of modelling complete aircraft models in which flight dynamics and non-linear aeroelastic effects are coupled. For example, SHARPy (Simulation of High-Aspect-Ratio Planes in Python) [62], UM/NAST (the University of Michigan's Non-linear Aeroelastic Simulation Toolbox) [63], Virginia Tech's NATASHA (Non-linear Aeroelastic Trim and Stability if HALE Aircraft) [64] and NANSI (Non-linear Aerodynamics/Non-linear Structure Interaction) [65].

Control Theory

Control theory aims to change the behavior of a dynamical system, typically referred to as the *the plant*, via the design of a *controller*, a system that can affect the plant's dynamics. It has wide application across a range of scientific and engineering fields, for example: biology

[66], robotics [67], chemical engineering [68], financial models [69] and fluid dynamics [70]. A control system can either be described as open-loop or closed-loop. Open-loop systems do not monitor outputs from the plant to determine the control. To give a simple example, most toasters allow the operator to change a numerical value, and once chosen the toaster will carry out a predetermined routine that does not monitor the toaster's current state. However, there are many unknowns and uncertainties in this system — such as the thickness or type of bread and the temperature or humidity of the room — which may lead to an undesired output of toast. To account for these one could design a toaster that uses closed-loop control. Closed-loop controllers monitor outputs from the plant and adjusts the controls in response. The operator of a closed-loop toaster would input a desired level of toasting, the toaster could then adjust the heating appropriately as it senses the current level of toasting.

Within aeroservoelasticity, open-loop control is commonly used in the study of maneuvers, for example, [71] investigated a *rolling maneuver* in which ailerons were deflected so that the rolling performance could be maximised. Closed-loop control has been employed for gust load alleviation [72], flight control [73], and active flutter suppression [74]. Historically, control systems have been added to aeroelastic systems once the aeroelastic design has been fixed — this is typically referred to as a sequential design. This strategy assures that the aircraft has good performance even without control, however, this approach cannot fully exploit the benefits of closed-loop control design. Furthermore, this methodology is likely to be sub-optimal compared to the simultaneous optimisation of the entire design-space [75]. Nevertheless, the sequential approach may be sufficient when the coupling between the different components of the system is weak. However, such couplings are significant for flexible aircraft in comparison to traditional *rigid-body* aircraft, that typically possess relatively stiff wings. The increase in coupling complicates design since the natural frequency of the first bending mode of a traditional aircraft compared to its flight dynamics will often be separated by at least an order of magnitude. This allows the structural and flight dynamic design processes to be separated. Conversely, flexible wings which possess natural frequencies comparable to those of the flight dynamics lead to strong coupling characteristics [76], in which a simultaneous design could be beneficial or even necessary for flight integrity. This paper will demonstrate the advantages and limitations of simultaneous design of coupled aeroservoelastic optimisation.

There are a further two techniques for solving plant and control optimisation problems, iterative [77] and nested [78] (sometimes called bi-level) strategies. Iterative methods alternate between optimising either the plant or the controller. For example: given a structural design first minimise some control cost; next, determine the sensitivity of the optimal control cost with respect to the structural variables; finally, use these sensitivities to redesign the structural design; this process is repeated until the designer is satisfied. Nested methods consist of a inner and outer optimisation loop. The outer loop optimises the overall objectives such as minimising mass, while, the inner loop finds the optimal controller for every plant generated by the outer loop. Fathy et al. [79] theoretically and numerical review sequential, iterative, nested and simultaneous strategies — sequential and iterative methods fail to guarantee the overall objectives optimality, whereas nested and simultaneous do.

Other complications in controller design, in ASE systems, are the static aeroelastic effects of control effectiveness or control reversal [80]. This is when the effect of a control surface is reduced or even reversed depending on the current state of the aircraft. For example, a trailing-edge control-surface on an aerofoil creates both an aerodynamically lift and moment when deflected. If the operator requires an upward motion they may deflect the control-surface to create an upward lift, however, in certain states the control-surface would also created a moment large enough to angle the aerofoil down, causing a downward motion. Further control design considerations are control surface saturation and controller free-play [81]. Saturation and free-play are non-linearities that can be added to the modelling; saturation is when the control input is limited to a finite amount, for example, a control surface being restricted to only deflecting by 5%; free-play is when a control surface can deflects without structural resistance around its desired input. Even with the lowest-fidelity models, LCOs may be observed when either free-play or saturation are present. This work will show, in Chapter 4, how control saturation can cause a LCO, even if it is the only source of non-linearity in a simple aeroelastic model.

Finally, it is worth discussing non-linearities in control theory. Non-linear control theory is an established subject [82], however, typically, ASE models have too many states or are too computationally demanding to take advantage of most non-linear control methods. Recently, non-linear methods have become more common with the ASE literature, for example, Wang et al. [83] used Model-Predictive Control (in which an optimisation problem is solved each time the control law requires updating) on a flexible aircraft model that contained quadratic non-linearities. Due to the fact that MPC requires on-line solution of optimisation problems, it can only be applied if the underlining system model is relatively low order. To achieve this, Reduced Order Methods (ROM) can be used. For example, methods to reduce model size were explored by Da Ronch et al. [83, 84], who reduced the size of a large-order, non-linear flexible aircraft model so that control design is practical.

1.1.2 Optimisation

As new aircraft surpass their current limitations the interdisciplinary coupling between the aerodynamics, structure and control become more influential. In light of this it is natural to explore a combined design methodology, such as Multidisciplinary Design Optimization

(MDO). A simultaneous MDO approach is increasingly used in a widening range of fields as increased computational resources have rendered solvable what were once prohibitively computationally expensive problems now. Applications of MDO include global optimisation of naval design [85], optimal design of large power and water distribution [86, 87], and multiobjective approaches in turbomachinary design [88]. However, the most-used engineering application has been within aircraft design. Current momentum for MDO within the aeronautics community is driven by three primary motivations: competition for better aerodynamic efficiency; the use of system wide objective functions, e.g. cost of production or fuel efficiency; and designs that rely on dynamic control systems to meet objectives. Efficiency is of paramount importance within the public aviation industry due to the rise in annual passenger traffic [89] and predictions that aviation's share of human caused climate change could be as high as 15% of the total by 2050 [90].

It has yet to be decided what class of optimiser is best suited for MDO of ASE problems and as such, many have been employed. Classically, most optimisation problems were solved with descent methods that used the gradients of the objective function (or approximations to the gradient) to find solutions that satisfied the Karush-Kuhn-Tucker (KKT) conditions. These are necessary conditions for a stationary point of a constrained non-linear objective function, but in general do not guarantee globally optimal solutions. Recently, non-gradient based optimisations have been used for aeroservoelastic design. These methods usually rely on using numerous candidate solutions that are spread throughout the design space. For example, a Particle Swarm Optimisation (PSO) method was used by Haghighat et al. [91] on a linear, flexible aircraft model; PSO iteratively attempts to improve the best known solution by using a population of particles (candidate solutions) that update their position and velocity through the design space according to both their local information and information on the population's (swarm's) best known positions. Genetic Algorithms (GA) for optimal wing designs were used by Manan et al. [92] and Nam et al. [93]. Again, GA's do not require gradient information and use instead a population of candidate solutions, each of which contain a set of characteristics that can randomly mutate or mix with other solutions. The advantage of non-gradient based methods is that they are able to sample large portions of design space, gathering global information. However, these methods can quickly become infeasible if function evaluations are computationally expensive and/or if there are many design variables. The strategies introduced in this thesis are gradient based but take advantage of globally collected data.

Every engineering problem has some inherent uncertainty and this can be taken into consideration by amending a classical optimisation problem by introducing stochastic variables and creating a non deterministic version of the problem. This can be performed on either the constraints, in what is known as Reliability-Based Design Optimisation (RBDO), or the objective function, which is known as Robust Design Optimisation (RDO). A comparison, using a wing design optimisation, between a RDO approach and a RBDO approach is made by Paiva et al. [94]. It was found that the RDO and RBDO solutions differed greatly, compared to the deterministic counterpart, even for conservative values of uncertainty.

Topology optimisation is commonly used to minimise the weight of airframes and is believed to have led to significant weight savings in the Airbus A380 [95]. Topology optimisation has yet to be used in an ASE optimisation. When designs have multiple, and usually conflicting, objective functions a branch of optimisation called multiobjective optimisation is used. One method for multiobjective problems is Goal Programming (GP), which was used by Suzuki et al. [96] for the design of a wing with a gust load alleviation system subject to multiple objectives. GP relies on the user defining priority levels for the objective functions, objectives are then minimised as long as they do not infringe on objectives with higher priority than them.

A major hurdle in the automation of design optimisation is automating the selection or prioritisation of variables. Traditionally, design variables are chosen from a large set of parameters from engineering experience. Since this could limit the potential in new concept designs, automating this choice with a more meticulous process may lead to improvements, as studied in Tu et al [97]. As an approximate model is being constructed, the variable space is sampled and variables that are likely to be dominant are kept and less influential ones are dropped. A variable screening process could become imperative as the number of design variables increases, especially if the complexity of the design-space is prohibiting the potential of a simultaneous design. More recently, a variable reduction technique has been investigated by Ghisu et al.[98]. Their work shows how a re-parametrisation based on a Proper Orthogonal Decomposition (POD) of initial optimisations can accelerate a design optimisation. Their paper is a clear proof of concept that a general parametrisation can be used to not only to facilitate the optimisation, but also to aid variable selection. However, it does not investigate in which situations this technique can lead to improvements, why it can accelerate optimisation and how best to choose a sample of data for the POD. Furthermore, the method is not yet fully automated as the number of variables removed is dependent on an arbitrarily chosen user input.

1.1.3 Optimisation of Aeroservoelastic Systems

A key difficulty is that even though a sequential design is expected to be sub-optimal, the increased design-space complexity associated with a simultaneous optimisation approach may itself make the optimisation problem intractable. For this reason, early studies in ASE optimisation often used simple models and output-feedback control systems, which allowed simultaneous optimisation over plant and controller. Suzuki [96] optimised the design of a cantilever wing by varying spar thickness and control gain, while constraining the system's open and closed loop stability, the spar stress and the control surface deflection angle; whereas Nam et al. [93] used a wide range of design variables (ply orientation of the composite layer, actuator placement and sizing) to minimise the root mean square of gust responses for various airspeeds. An early investigation in aeroelastic and control system optimisation for rotor flight [58] compared sequential and simultaneous optimisation techniques, confirming that rotor design and control design are strongly coupled and benefit from simultaneous optimisation. Although in these cases a simultaneous plant/controller optimisation is employed, only relatively simple control feedback is synthesised, in which controllability and observability conditions are not considered. Furthermore, observer dynamics were not included in the optimisation; instead, observer gains and sensor placement were chosen prior to the design. It was not investigated if adding complexity in these models would still allow a simultaneous approach to be advantageous.

An attempt to increase controller complexity included the modelling of parameter uncertainty, as considered by Moulin et al.[99]. This incorporates modern methods of robust MIMO control synthesis into a multidisciplinary design optimisation problem. However, this comes at the sacrifice of having to use a simpler sequential optimiser. A recent attempt to include more advanced control design [91] used the internal weighting matrices of an LQR problem as design variables for a linear, flexible aircraft model. This study sought to optimise a metric of endurance (a function of the lift-drag ratio and fuel fraction) over symmetric manoeuvres and gusts. Optimal actuation within aircraft manoeuvres was also studied by Maraniello et al. [71] using a nonlinear geometrically exact beam model and UVLM. Here a pre-programmed open-loop actuation is optimised via parameterising the deflection of control surfaces with a set of B-splines. Most authors use symmetric maneuvers and gusts within objective functions and constraints, due to the fact that linear models tend to not be accurate enough to model asymmetric aeroelastic simulations. This was investigated by Shearer et al [12]. who showed that a linearised model was insufficient to model a flexible aircraft performing asymmetric maneuvers. In these cases, more complex control architecture is incorporated into the optimisation, however the studies lack observer design, actuator/sensor sizing, and actuator/sensor placement considerations, problems well studied outside of the ASE literature. For example, the optimal placement of multiple actuators under $\mathcal{H}_\infty$-control has been studied by Kasinathan et al.[100] and conditions for the convergence, to an exact optimal performance, for a sequence of approximations are discussed. Similar existence and convergence proofs are not found within the ASE literature, despite the fact that it was shown in Demetriou [101] that placement of sensors can significantly change overall system performance.

System wide objective functions are crucial in concepts similar to the Boeing X-48, its blended wing body produces a problem not conducive to a segmented approach, i.e. an approach in which each part is designed separately and then aggregated. Instead, it is natural to chose system wide objectives and employ simultaneously design [102]. The Lockheed Martin X-56A [103], with its active flutter suppression, and the design of flapping wings [104] rely on their control systems, i.e. the underlying open-loop system cannot function. When the control dynamics are significant a simultaneous design outperforms sequential as they couple with the plants dynamics [79, 88].

1.2 Open Research Questions

Question 1. What would be the simplest but representative aeroservoelastic model that can be used to investigate simultaneous optimisation methods?

In order to investigate high volumes of optimisation trajectories it would be beneficial to design a model that requires minimal computational effort. In the context of aeroservoelastic design optimisation a balance between model complexity and computational requirements will be needed to ensure that the problem remains relevant. An obvious tactic to reduce computation burden would be to use a two-dimensional camberline model. However, this level of simplicity would normally limit the choice of design variables. Yet, we present such a model in Chapter 3 that does allow for design optimisation over all the aeroservoelastic fields.

Question 2. What are the trade-offs between problem complexity and performance improvements between simultaneous and sequential optimisation methodologies?

Increasing the problem complexity by using a simultaneous optimisation strategy or increasing the dimensionality of design space will not reduce the performance of possible designs and may indeed mean higher performing designs exist. But the existence of a better global minimum does not imply an optimiser will converge to better solutions. So although a sequential method is known to be a sub-optimal strategy it might outperform a simultaneous method depending on the design space.

Question 3. Is there a reparameterisation strategy that improves the optimisation trajectory in a complex design space?

Traditionally, design variables are intuitively chosen engineering variables, such as, masses and lengths. From a numerical point of view this might not be optimal. The choice of parametrisation should maximise the accessibility and connectedness of the design space but minimise its complexity, for example, the number of local minima. These goals are often conflicting. In this work we investigate whether a method that reparameterises a user inputted design vector can affect optimistion trajectories.

Question 4. How can the dimensionality of an optimisation problem be reduced in a problem independent manner?

As mentioned in **Question 2** design space complexity can limit optimiser performance. So although reducing the dimensionality of an optimisation problem might be sub-optimal it could promote the optimiser to converge to better solutions. Intimate knowledge of the design optimisation problem or physics may allow a user to prioritise and hence select only the most advantageous design variables. Nonetheless it would be favorable to be able to quantify and automate this process, independent of the model or optimisation being studied.

Question 5. Can early modelling choices be exploited to accelerate design optimisation?

Often the model selection and the optimisation problem definition are independent choices. We will show how model parametrisation or the choice of state-variables can accelerate aeroelastic calculations and design optimisations.

1.3 Thesis Outline

The remainder of the thesis can be summarised as such:

Chapter 2: establishes notation, frameworks and algorithms used in the thesis. It introduces aeroelastic systems as a set of Partial Differential Equations (PDE)'s for a fluid domain and a set of PDE's for a structural domain that are coupled due to interaction on a fluid-structure boundary. It then defines aerosevoelastic systems that have aeroelastic plants and a closed-loop controller — that has its own PDE and couplings.

Chapter 2 continues with defining the design variables, objective function and constraints. The concept of how to parametrise the design vector is introduced here and what consequences that could have on how an optimiser might converge. The Chapter then includes characterisations and Algorithms for Sequential and Simultaneous design optimisation strategies. Finally, a method that uses Proper Orthogonal Decomposition is described that is able to automate a reparameterisation and temporary variable reduction of the design vector.

Chapter 3: derives equations for a computationally inexpensive aeroservoelastic model that allows for design optimisation over aerodynamic, control and structural variables. A two-dimensional potential flow is used and a finite approximation is employed to approximated a linear, unsteady wake effect. The structure is modelled as a camberline, attached to linear heave and torsional springs, with a smoothly attached trailing edge control surface. This compliant trailing edge allows for design of the aerodynamic shaping as its deformations can be represented as polynomial of arbitrary finite size. As well as control variables, in the form of weightings in an Linear Quadratic Regulator problem, the positions of pressure readings allow the design over the observer dynamics of the closed-loop aeroservoelastic system.

Chapter 3 also defines an optimisation problem consisting of: a weighted cost function between a static metric, of the total aerofoil mass, and a dynamic metric, of the performance in rejecting a "$1-cos$" vertical gust; a constraint on the linear flutter velocity; constraints on the design variables directly to ensure they remain physical, for example, that the pressure readings are taken on the aerofoil.

Chapter 4: begins with a validation of the model described in Chapter 3. A simple optimisation of an open-loop system is then considered. This simple problem is used to demonstrate some of the difficulties expected from the full aerosevoelastic design optimisation, such as, how the complexity of the design space can influence the performance of a gradient-based optimiser. The Chapter continues by investigating the effect of including control saturation, a non-linearity, into the model. We show that it is possible that the saturated model can have a divergent time-domain response even if it has linear stable eigenvalues.

Chapter 4 also examines the advantages and disadvantages to the Algorithms defined in Chapter 2. Specifically, the chapter compares the difference between simultaneous and sequential optimisation strategies over a range of free-stream velocities — concluding that even though a sequential optimisation should be sub-optimal it can sometimes produce better results. When a simultaneous optimisation strategy is advantageous it is able to identify unintuitive but favorable design characteristics. Finally, the reparameterisation and temporary variable reduction techniques, introduced in Chapter 2, are explored. Both strategies were shown to be beneficial, especially in reducing the sensitivity of the final design with respect to the initial design.

Chapter 5: introduces a cantilever model of a wing that could be used for aeroservoelastic design optimisation, which is outlined in the Future Work Section of Chapter 8. Instead, in this work the cantilever model is used to derive analytic derivatives. The model consists of structural, slender beam equations, using velocities and forces as primary variables, and two-dimensional aerodynamic forces, including gust and control surface inputs. The use of the intrinsic formulations means only quadratic non-linearities are present in the equations, which is used to facilitate the derivation of derivatives in Chapter 6. The equations are linearised about the forward flight conditions and a truncated Galerkin projection is used to project the degrees of freedom into a finite space so that the equations of motion can be written in state-space form.

Chapter 6: explores the use of analytic expressions for derivatives to accelerate aeroelastic calculations. In past chapters *blackbox* optimisation solvers such as Matlab's `fmincon` were used to solve the design optimisation problems. These solvers use numerical methods to approximate derivatives, which can be time consuming as multiple function evaluations per design variable are required to approximate the gradient of said function. The chapter derives equations and an algorithm to efficiently calculate the non-linear equilibrium states of the cantilever model PDE, described at the start of Chapter 5.

Chapter 7: first verifies the state-space equations, linearised from the coupled intrinsic beam and two-dimensional aerodynamics PDEs in Chapter 5, by comparing the flutter speed and frequency predicted with values found in the literature. Furthermore, time-domain responses of the state-space equations demonstrated agree well with other authors using similar methods. Then the adjoint-based method in Chapter 6 is compared with results from time-domain solutions from the equations in Chapter 5 and are shown to be good agreement, hence, validating the analytic derivative expressions from Chapter 6. Finally, an example of how the adjoint-based method can accelerate aeroelastic calculations is presented.

Chapter 8: A summary of the work, it's contributions and conclusions are presented here.

1.4 Publications based on this work

1. Jacob J Broughton-Venner, Andrew Wynn, and Rafael Palacios. “Aeroservoelastic Optimisation of Cantilever Wings via Reparameterization and Variable Selection”. In: *under preparation* (2018)
2. Jacob J Broughton-Venner, Andrew Wynn, and Rafael Palacios. “Aeroservoelastic Optimisation of Aerofoils with Compliant Flaps via Reparameterization and Variable Selection”. In: *AIAA Journal* 56.3 (Dec. 2017), pp. 1146–1157. ISSN: 0001-1452. DOI: `10.2514/1.J056141`. URL: `https://doi.org/10.2514/1.J056141`
3. Jacob J Broughton-Venner, Andrew Wynn, and Rafael Palacios. “Aeroservoelastic optimisation of an aerofoil with active compliant flap via reparametrisation and variable selection”. In: *58th AIAA/ASCE/AHS/ASC Structures, Structural Dynamics, and Materials Conference.* 2017, p. 572
4. Jacob J Broughton-Venner, Andrew Wynn, and Rafael Palacios. “Aeroservoelastic Optimisation of an Aerofoil with Active Compliant Flap via Reparametrisation and Variable Selection”. In: *17th AIAA/ISSMO Multidisciplinary Analysis and Optimization Conference.* 2016, p. 3511

Chapter 2

Aeroservoelastic Optimisation

2.1 Aeroservoelastic Problem Description

In the pursuit of consistency and clarity, the purpose of this section is to introduce notation that will facilitate the comparison of various optimisation methods on different aeroservoelastic models. Problems in aeroelasticity involve the coupled analysis of both fluid dynamics and structural mechanics. Define the state variables for the fluid and structural domains respectively, as $\boldsymbol{f}$ and $\boldsymbol{s}$. These variables define the current state of the fluid and structural systems. Common state variables for these two fields are fluid velocities, fluid density, temperature and structural displacements. These domains interact with each other over a boundary $\Gamma = \Omega_{\mathcal{F}} \cap \Omega_{\mathcal{S}}$, where $\Omega_{\mathcal{F}}$ and $\Omega_{\mathcal{S}}$ are the fluid and structural domains – this is shown in Figure 2.1. Any force imparted by the fluid on the boundary Γ causes a deformation in the structure, i.e. a change in $\boldsymbol{s}$. This deformation in turn will affect the fluid's state $\boldsymbol{f}$. We define partial differential equations for the fluid dynamics and structural

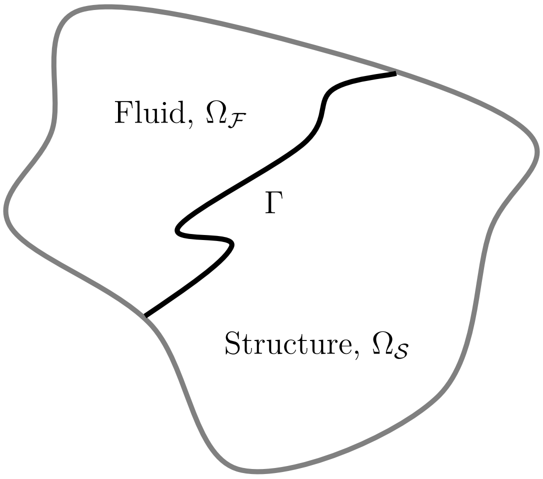
Fluid, $\Omega_{\mathcal{F}}$
Γ
Structure, $\Omega_{\mathcal{S}}$

Figure 2.1: Definition of Γ as the intersection of the fluid domain $\Omega_{\mathcal{F}}$ and structural domain $\Omega_{\mathcal{S}}$.

mechanics, respectively, as $\mathcal{F}$ and $\mathcal{S}$. The fields are coupled due to their interaction over the boundary Γ, hence, the partial differential equations are expressed as a function of their own state variables and of the state of the other field. Furthermore, we define an input $\boldsymbol{u}$ for this aeroelastic system. We will consider two types of input: the first are *extraneous-inputs*, these external and cannot be influenced and cover phenomena such as vertical gusts; the second are *controlled-inputs* that can be chosen, for instance, control surface deflection. One must thus solve

$$\mathcal{F}\left(\boldsymbol{f}, \boldsymbol{s}; \boldsymbol{u}\right) = 0 \quad \text{and} \quad \mathcal{S}\left(\boldsymbol{s}, \boldsymbol{f}; \boldsymbol{u}\right) = 0, \tag{2.1}$$

where the notation $\mathcal{F}\left(\boldsymbol{f}, \boldsymbol{s}; \boldsymbol{u}\right) = 0$ means that the variables before the semicolon have to be solved for, while, variables after are prescribed. The notation $(\cdot; \cdot)$ will be used throughout this work. For brevity, we equate the solution of the separate PDE's in (2.1) as the solution to

$$\mathcal{A}\left(\boldsymbol{f}, \boldsymbol{s}; \boldsymbol{u}\right) = 0. \tag{2.2}$$

We will also be considering an output $\boldsymbol{z}$ from this system. In theory this could be all the state variables $\boldsymbol{x} := [\boldsymbol{f}, \boldsymbol{s}, \boldsymbol{u}]^{\top}$, however, in reality (where obtaining real-time information about all states is impossible/impractical) it is a measured quantity $\boldsymbol{z} = \boldsymbol{z}(\boldsymbol{x})$, such as readings from

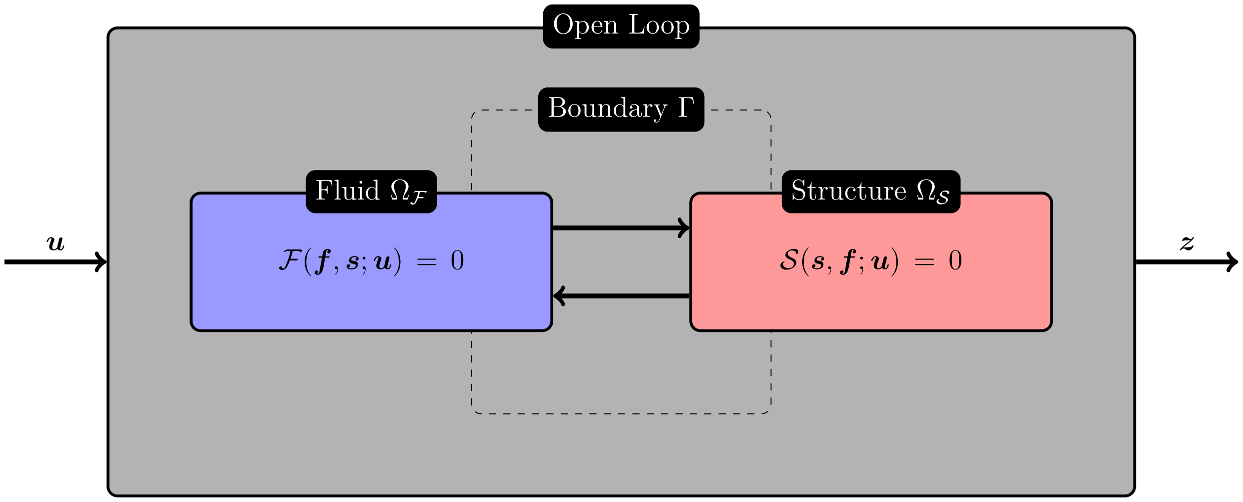
Open Loop
Boundary Γ
Fluid $\Omega_{\mathcal{F}}$
Structure $\Omega_{\mathcal{S}}$
$\boldsymbol{u}$
$\mathcal{F}(\boldsymbol{f}, \boldsymbol{s}; \boldsymbol{u}) = 0$
$\mathcal{S}(\boldsymbol{s}, \boldsymbol{f}; \boldsymbol{u}) = 0$
$\boldsymbol{z}$

Figure 2.2: Open-loop aeroelastic system with input $\boldsymbol{u}$ and output $\boldsymbol{z}$.

pressure or accelerometer sensors. The input/output relationship of this generic open-loop aeroelastic system is shown in Figure 2.2.

There are multiple combinations of modeling assumptions and equations one could use, for example, one could couple the Navier-Stokes [109], Euler or potential flow equations for the fluid with structural solutions bases on full solid mechanics, model decompositions or beam equations.

Two principle methods exist to solve such systems, monolithic and partitioned. Monolithic methods require a single system of discrete equations to be derived from the physics of both fields and their couplings. Consequently, the boundary conditions over Γ are always satisfied. However, if the scaling (e.g. the required time or space discretisation) between the fluid and structural problem differs significantly this approach can lead to computationally inefficient solutions [110]. This is because a monolithic method has to solve both problems using the same scaling. Thus, a decision has to be made to maintain accuracy but over-resolve one discipline, or to sacrifice accuracy. Instead, partitioned methods solve the fluid and structure problems independently, hence, allowing different scalings to be used for each sub-problem. This leads to more efficient solution times [111]. However, solving the fluid and structure equations separately in this manner introduces the obstacle of matching the solutions at the boundary Γ. This can be achieved by exchanging information in an alternating method between time steps. For example: at time step t_0 the fluid equation is solved and the corresponding tractions $\mathbf{t}_\Gamma(\boldsymbol{f}_0)$ on the current structure deflections $\boldsymbol{s}_0$ are calculated, where $\boldsymbol{f}_0$ are the fluid states at time step t_0; these tractions are then inputed into the structural equations that are solved at t_1, to give the deflections $\boldsymbol{s}_1$ which are sent to the fluid solver for the solution at the next time step; this is then repeated as desired. This type of coupling is referred to as weak and is an explicit method that can suffer from instabilities [112], whereas the coupling in monolithic methods are implicitly included in the equations and are often more robust [113].

This work is primarily concerned with aeroservoelastic systems, that is, aeroelastic systems with active control systems. Hence, we introduce the closed loop system in Figure 2.3 with extraneous-input $\boldsymbol{w}$ and controlled-input $\boldsymbol{u} = \mathcal{K}(\boldsymbol{y})$ that is a function of the measured output $\boldsymbol{y}$. The solution to this closed loop model will equivalent to solving

$$\bar{\mathcal{A}}\left(\boldsymbol{f}, \boldsymbol{s}, \boldsymbol{u}\right) = \bar{\mathcal{A}}\left(\boldsymbol{x}\right) = 0, \tag{2.3}$$

note that $\boldsymbol{u}$ (or at least some of $\boldsymbol{u}$) has to be solved for now.

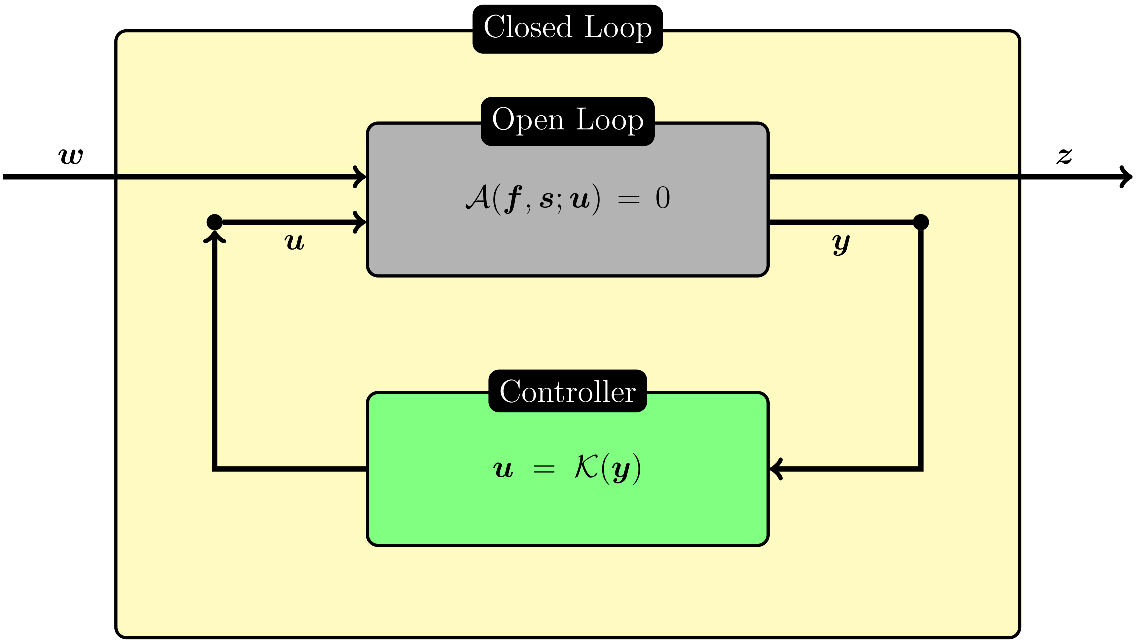
Closed Loop
Open Loop
$\mathcal{A}(\boldsymbol{f}, \boldsymbol{s}; \boldsymbol{u}) = 0$
$\boldsymbol{w}$
$\boldsymbol{z}$
$\boldsymbol{u}$
$\boldsymbol{y}$
Controller
$\boldsymbol{u} = \mathcal{K}(\boldsymbol{y})$

Figure 2.3: Aeroservoelastic model made from connecting the system in Figure 2.2 to a feedback-controller $\mathcal{K}(\boldsymbol{y})$.

2.2 Optimisation Problem Description

2.2.1 Design Vector

Design Optimisation is the process of finding the *best* design (or at least improving upon a current design) that *meets the requirements* for the design's purpose. A simple aeroelastic example would be to find the lightest wing (*best*) that is able to lift a certain mass but that does not fail under any expected loads (*meets the requirements*). To achieve this objective one needs to be able to distinguish between competing designs. This is achieved by parameterising the designs by a set of *design variables*. We define the initial design vector as $\tilde{X} \in \mathbb{R}^d$ as the set of all the design variables. Furthermore, the design vector is to be a concatenation of design variables from the three fields described in Section 2.1: the fluid dynamics, structural mechanics and control architecture, respectively, $\tilde{X} = [F, S, U]$. In a

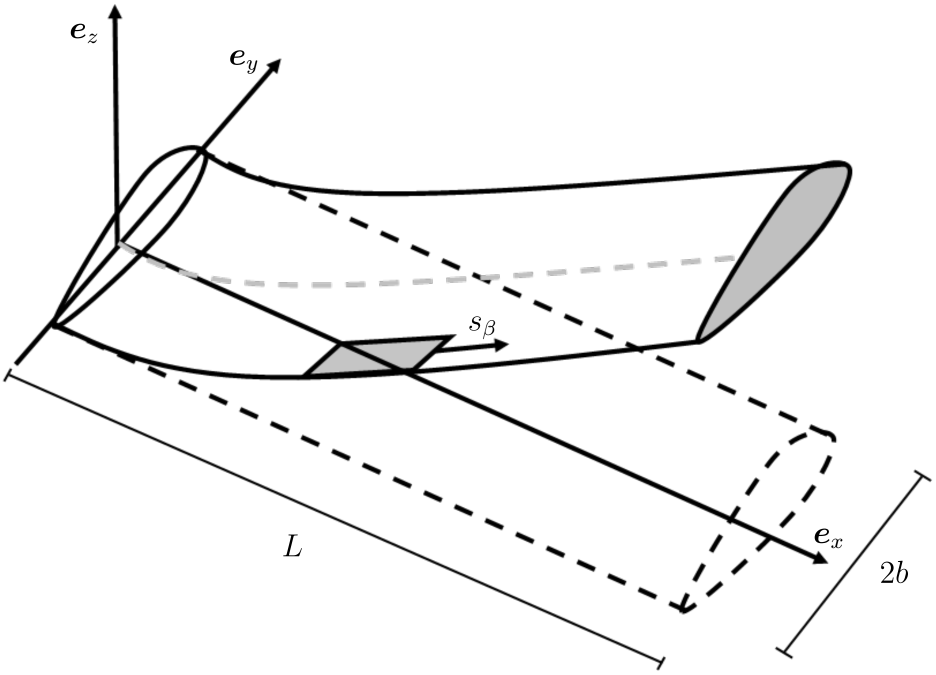

Figure 2.4: Examples of *engineering variables* for a cantilever wing.

typical cantilevel model, for example, this design vector could consist of: the wing twist, which affects the lift distribution; the structural mass and/or stiffness, which affects both the weight and structural response of the wing; and the sizing of a control surface, which influences the authority of the controlled response. During the design process an optimiser will seek to change the design vector as to test whether it has found the *best* design (or improved upon the previous design).

Traditionally, the design vector would be a collection of *engineering variables*, quantitative qualities that are an intuitive choice for a person, for example, chord-length L, span-length $2b$ or positions of control surfaces s_β, all of which are depicted in Figure 2.4. Clearly the choice of what aspects of the design will be varied will affect the structure of the optimisation problem. However, even the manner in which the design variables are parameterised can alter the final design. Consider the cantilever model again. How should the structural mass distribution be parametrised? One could simply define the mass $m(s_i)$ at a finite number of positions along the wing $\{s_i\}$ as design variables, and then interpolate the mass between these locations. Alternatively and slightly less intuitively, one could define a finite set of *mass shape functions* $m_i(s)$, where s is the span-wise distance along the wing, such that the mass at any point of the wing would be $\sum_i a_i m_i(s)$ and a_i would be the design variable sent to the optimiser. One can see an example of the difference such parameterisations would have on the mass distribution along a wing in Figure 2.5.

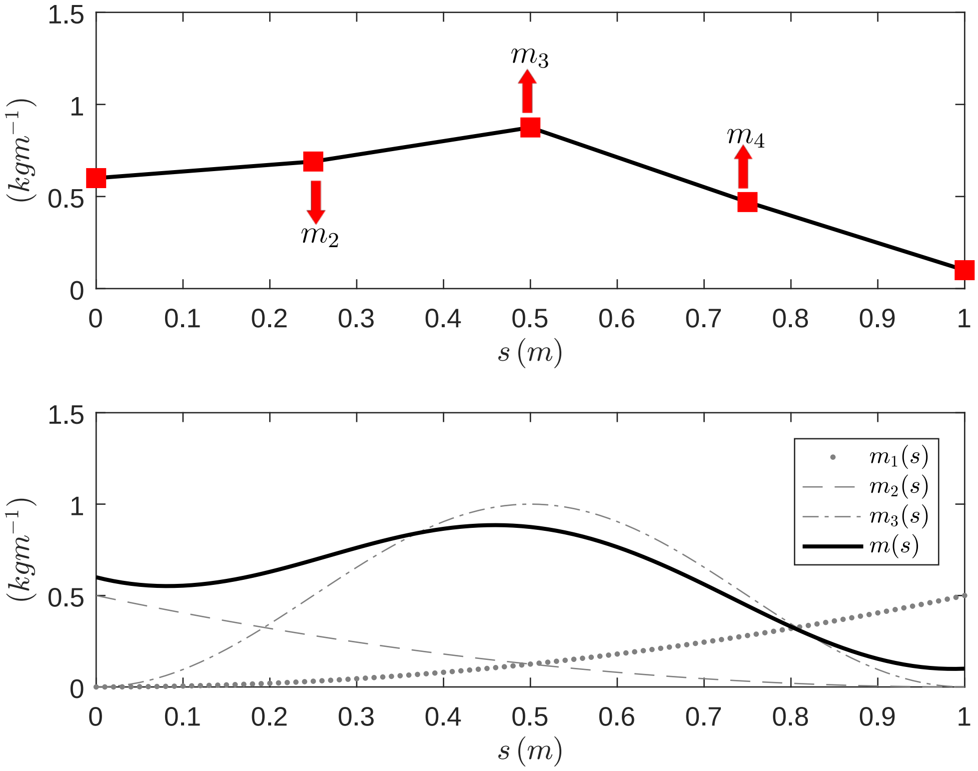

Figure 2.5: Example of different parametrisation choices. Top: mass variation at discrete wing locations and linear interpolation between known values. Bottom: three mass shape functions and the corresponding mass distributions $m(s) = \sum_{i=1}^{3} m_i(s)$.

Parametrisation choices can also affect the optimisation and final design, as was shown by Maraniello et al. [114] when comparing the use of B-splines and discrete sines as sets of basis functions to parametrise the actuating torque input of a flexible pendulum. In the wing mass and pendulum examples the choice of parameterisation changes the available design space, when choosing a parametrisation, maximising how much of the design-space is accessible and connected is key but so is minimising the design space complexity. These are often conflicting goals. For instance, in the first cantilever example above, what is the most appropriate number of locations s_i? Clearly the more locations used the larger the variety of possible designs. However, this will increase the design space complexity, possibly creating local minima that would terminate a gradient based optimiser at a sub-optimal design, compared to using fewer locations s_i.

The question of how to choose an appropriate design vector parametrisation for a given optimisation problem is often challenging. It might not be practical or optimal using traditional methods, i.e. when design variables are picked from experience and knowledge, especially when considering the design of novel platforms that may call for unintuitive solutions. Hence, it may improve the performance of an automated Multidisciplinary Design Optimisation (MDO) technique if the design vector parametrisation is, at least in part, automatically selected within the optimiser. One option for this is to simply to choose an alternative basis for the design vector. Suppose an alternative basis of $\mathbb{R}^d$ is represented by a orthogonal matrix $H \in \mathbb{R}^{d\times d}$ whose columns $\{h_i\}_{i=1}^d \subset \mathbb{R}^d$ are the elements of the basis. Now, for any vector $\tilde{X} \in \mathbb{R}^d$ it is possible to express

$$\tilde{X} = \sum_{i=1}^{d} \alpha_i h_i := X, \tag{2.4}$$

where $\alpha_i = (H^\top \tilde{X})_i \in \mathbb{R}$ and we define X as the design vector post this parametrisation.

2.2.2 Objective function and Constraints

This work is concerned with the design optimisation of aeroservoelastic systems. Design optimisation requires a definition of merit so that one can differentiate which design is best — this is performed via an objective function J. The objective function is constructed depending on the goals of the design/designer. For instance, while considering the optimal design of a flexible aircraft the objective of Haghighat et al. [91] was to surpass current aircraft endurance limits. Hence, they defined an appropriate cost function that preferences low weight but high aerodynamic efficiency. More frequently in MDO, objective functions built on higher-level concepts less directly based on the aircraft can be found, such as, Tetzloff et al. [115] who consider fleet-wide objectives on direct operation cost, carbon dioxide emissions and noise metrics. It might be the case that this type of objective function would also benefit from an automated design vector parametrisation, since the link between objective function and engineering variables is further removed.

In this work, we define the objective function as

$$J = J\left(\boldsymbol{x}(X),\, X\right). \tag{2.5}$$

It can be seen that the objective function is both explicitly a function of the design vector and implicitly through the model's state variables $\boldsymbol{x}(X)$. Suppose that in the cantilevel example the objective function is total mass, while the design variables are masses along the wing and the sizing of a control surface. The masses along the wing would explicitly appear in the objective function but the sizing of the control surface could implicitly affect the objective function (for example, perhaps a larger control surface could *meet the requirements* of the design with a lower total mass).

At best, the objective function will be minimised, constrained to the governing equations described by $\bar{\mathcal{A}}$, which now are a function of the design vector also, i.e.

$$\min_{X} J\left(\boldsymbol{x}(X),\, X\right) \tag{2.6}$$

$$\text{such that } \bar{\mathcal{A}}\left(\boldsymbol{x}(X),\, X\right) = 0. \tag{2.7}$$

Usually further constraints are needed for the design to be practical, for example, ensuring that there are no structural failures. Often these constraints require extra physics and can possibly be represented by non-linear inequality constraints:

$$c\left(\boldsymbol{x}(X),\, X\right) \leq c_i, \tag{2.8}$$

where $c,\, c_i \in \mathbb{R}^{N_i}$ and $N_i \in \mathbb{Z}_{>0}$ is the number of such constraints. A typical case, using the cantilever example, of a constraint that would require further physics would be the introduction of a constraint that ensures the wing does not buckle under expected loads. Buckling constraints can be found in [116] where optimisation of a wing is undertaken with mass, strength, and buckling under consideration. Constraints placed directly upon the design variables will referred to as *bounds* and be denoted as

$$c_l \leq X \leq c_u, \tag{2.9}$$

where $c_l,\, c_u \in \mathbb{R}^d$. Such constraints are needed to assure conditions such as the control surfaces are at least smaller than the wing or to stop an optimiser testing negative masses.

2.3 Simultaneous and Sequential Optimisation Strategies

Historically, control systems have been added to aeroelastic systems once the aeroelastic design has been fixed, which is typically referred to as a sequential design methodology. This is likely to be sub-optimal compared to the simultaneous optimisation of the entire design-space [75]. The sequential approach may be sufficient when the coupling between the different components of the system is weak. However, such couplings are typically more prominent with recently developed very flexible airframe concepts in comparison to traditional airframes, that were built with relatively stiff wings.

In the cantilever wing example — with wing twist F, mass S and control surface sizing U as design variables — a classical sequential approach would be to first optimise the model only considering the wing twist and mass variables, the open loop properties. Once a wing has been designed, i.e. a F^* and S^* have been found a meeting all requirements, a second optimisation problem would be solved to select the control sizing variables U. The effect of this optimisation might be to improve the objective function, but the restriction of the initial design of the open loop variables may limit any significant gains. On the other hand, a simultaneous approach would simply optimise the entire design vector $X = [F,\, S,\, U]^\top$. The relaxation of no fixed open-loop structure may allow the optimiser to explore areas of design space that lead to substantial gains in the objective function.

For brevity, denote one step of a gradient-based optimiser satisfying $\bar{\mathcal{A}}(\boldsymbol{x}(X); X) = 0$ with input $\boldsymbol{w}$, the aeroservoelastic system described in (2.3) and Figure 2.3, from the current design variables $X = [F,\, S,\, U]^\top \in \mathbb{R}^d$ to its subsequent value $X^+ = [F^+,\, S^+,\, U^+]^\top$ by

$$X^+ = \bar{\varphi}(X, H), \tag{2.10}$$

where $H \in \mathbb{R}^{d\times d}$ is the basis in which the gradients are to be computed. Algorithm 1 produces a trajectory of design variables $\bar{\varphi}_\epsilon(X^0, H) \in \mathbb{R}^{d\times n+1}$ corresponding to convergence of a *simultaneous* optimisation to a tolerance ϵ, from initial condition X^0, where n is the total number of algorithm iterations required to reach the chosen tolerance.

Algorithm 1 Convergence of a simultaneous optimisation.

```
inputs $X^0 \in \mathbb{R}^d$ satisfying $0 \leq X^0 \leq 1$, $\epsilon > 0$, $n = 0$, $\bar{\mathcal{A}}(\boldsymbol{x})$, $\boldsymbol{U}_\infty$.
repeat
    $X^{n+1} \leftarrow \bar{\varphi}(X^n, H)$
    $n \leftarrow n + 1$
until $|X^n - X^{n-1}| < \epsilon$
$\bar{\varphi}^*_\epsilon(X^0, H) \leftarrow X^n$
$\bar{\varphi}_\epsilon(X^0, H) \leftarrow [X^0, X^1, \ldots, X^n]$
return $\bar{\varphi}_\epsilon(X^0, H) \in \mathbb{R}^{d\times n+1}$ and $\bar{\varphi}^*_\epsilon(X^0, H) \in \mathbb{R}^d$.
```

Alternatively, we define one step of a gradient-based optimiser satisfying $\mathcal{A}(\boldsymbol{f}, \boldsymbol{s}; \boldsymbol{u}_0) = 0$ (i.e. the open-loop aeroelastic system described in Figure 2.2) from the current design variables $X = [F,\, S,\, U]^\top \in \mathbb{R}^d$ to its subsequent value $X^+ = [W^+,\, Z^+,\, U]^\top$, noting the control variables remain unchanged, by

$$X^+ = \varphi(X, H), \tag{2.11}$$

Subsequently we define Algorithm 2 to create a trajectory of design variables $\varphi_{\epsilon_1,\epsilon_2}(X^0, H) \in$

$\mathbb{R}^{d\times n+1}$ corresponding to convergence of a *sequential* optimisation firstly for the open loop variables to a tolerance ϵ_1, then to a tolerance ϵ_2, from initial condition $X^0 = [F^0, S^0, U^0]^\top$, where n_1 is the number iterations required for the initial open loop optimisation for convergence to a tolerance ϵ_1 and n is the number total number of iterations required for both stages in the optimisation.

Algorithm 2 Convergence of a sequential optimisation.

```
**inputs** $X^0 \in \mathbb{R}^d$ satisfying $0 \leq X^0 \leq 1$, $\epsilon_1 > 0$, $\epsilon_2 > 0$, $n = 0$, $\mathcal{A}(\boldsymbol{f}, \boldsymbol{s}; \boldsymbol{u_0})$.
**repeat**
    $X^{n_1+1} = [F^{n_1}, S^{n_1}, U^0]^\top \leftarrow \varphi(X^{n_1}, H)$
    $n \leftarrow n + 1$
**until** $|X^{n_1} - X^{n_1-1}| < \epsilon_1$
$\varphi^*_{\epsilon_1}(X^0, H) \leftarrow X^{n_1} = [F^{n_1}, S^{n_1}, U^0]^\top$
$\varphi_{\epsilon_1}(X^0, H) \leftarrow [X^0, X^1, \ldots, X^{n_1}]$
$n \leftarrow n_1$
$X^n \leftarrow \varphi^*_{\epsilon_1}(X^0, H)$
**repeat**
    $X^{n+1} \leftarrow \bar{\varphi}(X^n, H)$
    $n \leftarrow n + 1$
**until** $|X^n - X^{n-1}| < \epsilon_2$
$\varphi^*_{\epsilon_1,\epsilon_2}(X^0, H) \leftarrow X^n$
$\varphi_{\epsilon_1,\epsilon_2}(X^0, H) \leftarrow [X^0, X^1, \ldots, X^n]$
**return** $\varphi_{\epsilon_1,\epsilon_2}(X^0, H) \in \mathbb{R}^{d\times n+1}$ and $\varphi^*_{\epsilon_1,\epsilon_2}(X^0, H) \in \mathbb{R}^d$.
```

2.4 Parametrisation and Variable Selection

2.4.1 Reduced order methods

Due to the computational demand of aeroelastic models it is common to use ROMs both for analysis and control design. These can be used system wide or to parts of the model, for example, Wang et al. [117] reduces a large finite element description of a large aeroelastic structural model to a geometrically-nonlinear beam description. A frequently used ROM is the Proper Orthogonal Decomposition (POD) [118, 119], in which a sample of a high-fidelity model (or experimental data) is used to find the coefficients in an expansion of basis functions. This method is useful for capturing high-fidelity physics in a relatively low order manner. Other methods include Volterra theory [120], multi-fidelity meta-modeling [121] eigen-system realization algorithm [122] and harmonic balance [123]; all of which are summarised in [124].

2.4.2 Proper Orthogonal Decomposition

Starting with a set of engineering variables it would be helpful to find a parametrisation that facilitates the choosing of a subset of variables that minimises the number of dimensions needed to describe the design well enough so that the design-space is still able to be adequately explored. One method of achieving this is to use Proper Orthogonal Decomposition (POD). POD is a powerful data analysis tool that is often used to achieve a low dimensional representation of high dimensional data. This method is sometimes called Principal Component Analysis or Empirical Orthogonal Functions and is used in many fields, including turbulent flow analysis [125] and image processing [126]. POD uses a sample of points to create an orthogonal basis in which the first basis vector maximises the projection of the sample data, i.e. a basis $\boldsymbol{H} = [h_1, h_2, \ldots, h_d]$ with $\boldsymbol{H}^\top \boldsymbol{H} = \boldsymbol{I}$ is found such that its first basis vector h_1 satisfies,

$$\max_{h_1} \left(h_1, \boldsymbol{X}\right)^2 \quad \text{s.t. } h_1^\top h_1 = 1, \tag{2.12}$$

where $\boldsymbol{X}$ is the sample data and $(\cdot, \cdot)$ is the scalar inner product operator on $\mathbb{R}^d$. The second basis vector maximises the projection of sample data again but is constrained to be orthogonal to the first vector. This process continues until an orthogonal basis is formed with the last vector pointing in the direction that describes the least amount of variance.

With this new basis, optimisation can now be performed with the intention that the rotation will yield a faster and more robust optimisation routine. Furthermore, this method offers a method with which to make informed decisions on the removal of dimensions, namely by removing the least variant directions. Not only does this POD method output the least variant directions but also, for each basis vector, there is an associated eigenvalue λ_i which is proportional to the variance in that direction. Hence one can calculate the percentage of variance described from removing one or more of these POD dimensions by,

$$\Lambda = \frac{\sum\limits_{i=1}^{r<d} \lambda_i}{\sum\limits_{i=1}^{d} \lambda_i} = \text{Fraction of variance described}, \tag{2.13}$$

where d is the dimension of the design vector and r a positive integer less than d. This leads to a natural way of deciding which and how many dimensions to remove. Prior to optimisation, a total variance described by a reduced problem can be set and then subsequently the maximum number of dimensions can be removed while this percentage is still described. The optimiser can then converge in this smaller space, the removed dimensions can then be considered again and the full optimisation restarted at this point.

Firstly, to use a POD technique a sample of points is needed. In this work, we denote the POD basis calculated from a collection of vectors $\boldsymbol{X} = [X_1, \ldots, X_k] \in \mathbb{R}^{d \times k}$ by $\{\lambda_i, h_i\}_{i=1}^{d} = \mathrm{POD}(\boldsymbol{X})$. Here, $\lambda_i \in \mathbb{R}$ are the singular values corresponding to each $h_i \in \mathbb{R}^d$. The ensemble of vectors to be passed to the POD analysis are a collection of iteration paths from preliminary optimisations starting from $\{X_j^0\}_{j=1}^{N}$, i.e. $\varphi_{\epsilon_1}(\boldsymbol{X}^0) = [\varphi_{\epsilon_1}(X_1^0, I), \ldots, \varphi_{\epsilon_1}(X_N^0, I)]$, where $I \in \mathbb{R}^{d \times d}$ is the identity matrix and $\boldsymbol{X}^0 = [X_1^0, \ldots, X_N^0]$. This $\varphi_\epsilon(\boldsymbol{X}^0)$ is referred to as *the training set* with *training set tolerance* ϵ_1. This methodology closely follows that in Ghisu et al.[98]. The aim of such a transformation is that a rotation of basis such that the first basis vector points in the dominant direction of the observed optimisation paths may help with the numerical conditioning of the problem.

This work will make use of Algorithm 3 which describes a three-step algorithm which makes use of basis rotation and reduction. Given a set of initial conditions $\{X_i^0\}_{i=1}^{N}$, a preliminary ensemble of optimisation trajectories *in the original basis* are computed using Algorithm 1 to a relatively large tolerance $\epsilon_1 > 0$. Next, POD is applied to this ensemble of trajectories to determine the most dominant optimisation directions and a reduction proportion $0 < \Lambda \leq 1$ is selected. A new basis H is formed of the POD vectors and an initial optimisation, to tolerance ϵ_1, is performed in only a fraction Λ of the most dominate directions. Using the outputs of this initial, coarse, optimisation as initial conditions a final set of optimisations are then performed in the full rotated basis to a *convergence tolerance* $0 < \epsilon_2 < \epsilon_1$. Note finally that applying Algorithm 3 with $\Lambda = 1$ results in a rotated basis with no dimension reduction.

Algorithm 3 Simultaneous optimisation in a rotated/reduced basis.

```
inputs $\{X_i^0\}_{i=1}^N \subset \mathbb{R}^d$ satisfying $0 \leq X_i^0 \leq 1$, $0 < \epsilon_2 < \epsilon_1$, $0 < \Lambda \leq 1$.
for $i = 1$ to $N$ do
  $\boldsymbol{X}_i \leftarrow \bar{\varphi}_{\epsilon_1}(X_i^0)$
end for
$\{h_j, \lambda_j\}_{j=1}^d \leftarrow \mathrm{POD}\left([\boldsymbol{X}_1, \ldots \boldsymbol{X}_N]\right)$
$H \leftarrow [h_1, \ldots, h_d]$
$$r \leftarrow \underset{1 \leq s \leq N}{\operatorname{argmax}} \left\{ \frac{\sum_{j=1}^s \lambda_j}{\sum_{j=1}^N \lambda_j} \leq \Lambda \right\}$$
for $i = 1$ to $N$ do
  $Y_i \leftarrow \bar{\varphi}_{\epsilon_1}^* \left( H^\top X_i^0, \{h_j\}_{j=1}^r \right)$
  $Y_i \leftarrow \bar{\varphi}_{\epsilon_2}^* \left( Y_i, H \right)$
  $X_i^* \leftarrow Y_i$
end for
return $\{X_i^*\}_{i=1}^N \subset \mathbb{R}^d$.
```

Chapter 3

Two Dimensional Aeroservoelastic Model

This Chapter introduces a common aeroelastic model, composed of a thin aerofoil with a compliant trailing edge and mounted on springs, which will be used to investigate the optimisation strategies of Chapter 2. The aerodynamic model used is able to describe a thin aerofoil undergoing arbitrary deformations, however, here it is limited to describe the motion of the compliant trailing edge. Once the state-space equations for the open-loop system are derived it is coupled to an LQG controller which relies on values of the pressure difference over the camberline to build an observer state. Control is achieved, albeit saturated, through the position of the trailing edge. A full aeroservoelastic design optimisation is then defined for the closed-loop system. Design variables are chosen to span the three ASE fields, i.e. structural, aerodynamic and control. This chapter introduces the mathematical model and optimisation problem that are subsequently investigated in Chapter 4.

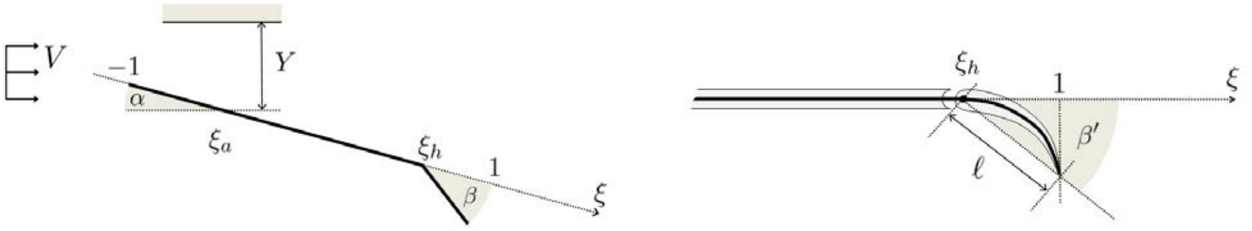

(a) Camberline description (b) Trailing edge description

Figure 3.1: Visualisation of aerofoild model.

3.1 Aeroelastic Model

This section details how the aeroelastic forces are derived for the model in Figure 3.1. The model assumes that an aerofoil can be represented by its camberline and the fluid can be approximated by a 2D potential flow. The model can be written in state-space form, which allows for the addition of a controller and for external gust excitation. A camberline approximation works well when the flow remains attached, which requires small angles of attack and small deformations. Furthermore, 2D potential flow is incompressible, irrotational and inviscid. In physical terms this corresponds to high Reynolds number and low mach-numbers. A review of several aerodynamic modelling methods was included in [127]. It compared the difference in gust responses between steady 2D theory; unsteady 2D theory with Wagner and Küssner functions; Unsteady Vortex Lattice Method (UVLM); and Doublet-Lattice Method (DLM). Kier [127] concluded that the steady strip theory is fastest to react to the gust load while the unsteady strip theory is the slowest. Steady strip theory and VLMs (Vortex Lattice Methods) tend to overestimate loads. The aerofoil's structural support is modeled by linear pitch and plunge springs connected to the elastic axis, at a distance ξ_a from its centre. The aerofoil has a half chord length of b and has a streamwise velocity of V_∞. The trailing edge can deform smoothly from the point labeled ξ_h in Figure 3.1. Note that ξ, the chordwise direction, will be defined non-dimensionally, with $\xi = -1$ and $\xi = 1$ corresponding to the leading edge and tail, respectively.

3.1.1 Deformation Representation

So that this model can be reduced to a state space form, the shape of the aerofoil is assumed to lie in the span of a finite basis of functions. Such *mode shapes*, $y_i\left(\xi\right)$, will be superimposed to describe the aerofoil's shape. The mode shapes can be chosen arbitrarily but it will be shown in Section 3.1.8 that it is advantageous for them to be orthogonal under some metric. Once mode shapes have been selected, the displacement $y(\xi, t)$ of any point on the chord can be described by,

$$y\left(\xi,t\right)=y_Y\left(\xi\right)Y\left(t\right)+y_\alpha\left(\xi\right)\alpha\left(t\right)+\sum_{i=3}^{n_{mo}}y_i\left(\xi\right)D_i\left(t\right),\quad -1\leq\xi\leq 1,\quad t\leq 0. \tag{3.1}$$

The mode shapes y_i, y_Y, y_α are functions of the chordwise direction ξ only, while the temporal coefficients $Y(t)$, $\alpha(t)$, $D_i\left(t\right)$ depend on t, the time coordinate. Note that we retain specific notation for the heave and pitch degrees of freedom. In particular, $Y\left(t\right)$ is the temporal coefficient of the heave degree of freedom and $\alpha\left(t\right)$ is the temporal coefficient of the the pitch degree of freedom. The mode shapes associated with the heave and pitch motion are given by,

$$y_Y\left(\xi\right)=1\quad\text{and}\quad y_\alpha\left(\xi\right)=b\left(\xi_{ea}-\xi\right). \tag{3.2}$$

Note that only a finite number of mode shapes, n_{mo}, are used and, hence, only deformations that belong to the space spanned by $\{y_i\left(\xi\right)\}_{i=3}^{n_{mo}}$ are possible. For brevity, we will interchangeably denote $y_Y(\xi)=y_1(\xi)$, $y_\alpha(\xi)=y_2(\xi)$, $Y(t)=D_1(t)$ and $\alpha(t)=D_2(t)$. Hence the motion of the camberline can be described by,

$$\dot{y}\left(\xi,t\right)=\sum_{i=1}^{n_{mo}}y_i\left(\xi\right)\dot{D}_i\left(t\right)\quad\text{and}\quad\ddot{y}\left(\xi,t\right)=\sum_{i=1}^{n_{mo}}y_i\left(\xi\right)\ddot{D}_i\left(t\right), \tag{3.3}$$

where $\dot{(\cdot)}:=\frac{d}{dt}$.

3.1.2 Pressure

The unsteady 2D forces on the aerofoil are derived from the distribution of pressure above and below the plate. The pressure can be found via the unsteady Bernoulli equation,

$$p\left(\xi,t\right)=-\rho\left(\frac{u^{2}\left(\xi,t\right)}{2}+\dot{\varphi}\left(\xi,t\right)\right)+p_{0}. \tag{3.4}$$

The Bernoulli equation holds when the flow is irrotational and the density, ρ, is constant. Here u is the local flow velocity on the velocity, $\varphi(\xi,t)$ is the flow potential and p_0 an irrelevant constant since only the pressure difference, Δp, is needed to construct the eventual state-space model for the aerofoil's motion, defined in (3.6). The local flow velocity, i.e. the velocity the aerofoil experiences locally, is given by

$$u(\xi,t)=V_{\infty}+\varphi'\left(\xi,t\right). \tag{3.5}$$

Now, (3.4) can be used with (3.5) to obtain an expression for the pressure difference over the aerofoil,

$$\Delta p\left(\xi,t\right):=p_{lower}-p_{upper}=2\rho\left(\dot{\varphi}\left(\xi,t\right)+V_{\infty}\varphi'\left(\xi,t\right)\right). \tag{3.6}$$

Note that this is an exact expression and not a linearisation, since the quadratic terms simply cancel out. An expression for pressure will be useful later to mimic pressure readings along the aerofoil for the input to a dynamic observer.

3.1.3 Non-Circulatory Potential

To begin, an expression for the velocity potential, φ needs to be derived. The full derivation can be found in [128] and follows the same method as [51]. The velocity potential is split into two contributions arising from non-circulatory effects φ^{nc} and circulatory effects φ^{c}, such that, $\varphi(\xi,t) = \varphi^{nc}(\xi,t)+\varphi^{c}(\xi,t)$. The potentials φ^{nc} and φ^{c} are built from point flow sources such that all the modeled boundary conditions are satisfied, for example no flow is allowed to pass through the camberline. For completeness a derivation of the non-circulatory potential, φ^{nc}, is presented here. Physically, the non-circulatory potential arises due to the fact that air cannot pass through the aerofoil. Its effects are instantaneous and lead to the extra apparent mass an aerofoil experiences due to the air around it.

It can be shown [51] that a sheet of sources with strength $\sigma\left(\xi_1,t\right)$ on the upper side of the camberline and a sheet of sources with strength $-\sigma\left(\xi_1,t\right)$ on the lower side leads to the potential,

$$\varphi^{nc}\left(\xi,t\right) = \frac{b}{4\pi}\int_{-1}^{1}\sigma\left(\xi_1,t\right)\ln\left(\frac{\left(\xi-\xi_1\right)^2+\left(\sqrt{1-\xi^2}-\sqrt{1-\xi_1^2}\right)^2}{\left(\xi-\xi_1\right)^2+\left(\sqrt{1-\xi^2}+\sqrt{1-\xi_1^2}\right)^2}\right)d\xi_1. \tag{3.7}$$

The source strength will be chosen so that there is no fluid velocity through the camberline. This is achieved by a Neumann boundary condition on the camberline of the aerofoil i.e.

$$\mathbf{u}(\xi,t).\mathbf{n}(\xi,t) = V_y(\xi,t), \tag{3.8}$$

where $\mathbf{u}$ is the fluid velocity on the camberline, $\mathbf{n}$ is the normal vector of the camberline and V_y is the surface velocity normal to the camberline. Since, a source strength of $\sigma\left(\xi,t\right)$

corresponds to a normal flow velocity of

$$V_y\left(\xi,t\right)=\frac{\sigma\left(\xi,t\right)}{2},\tag{3.9}$$

we can choose the source strength such that it matches the surface normal velocity V_y corresponding to a camberline $y(\xi,t)$, defined in (3.1), in a free-stream flow of V_∞. Physically this V_y can be thought as arising from two contributions. The first arises from vertical motion of the camberline, i.e $\dot{y}\left(\xi,t\right)$, given in (3.3)

$$V_y^1\left(\xi,t\right)=\sum_{i=1}^{n_{mo}}\dot{D}_i\left(t\right)y_i\left(\xi\right).\tag{3.10}$$

The second is due a vertical component of the free-stream velocity V_∞ being induced by the curvature of the camberline, this is given by

$$V_y^2\left(\xi,t\right)=V_\infty\sum_{i=1}^{n_{mo}}D_i\left(t\right)y_i'\left(\xi\right),\tag{3.11}$$

where $()' := \frac{d}{d\xi}$. These two contributions V_y^1, V_y^2 can be summed and used in (3.9) for an expression for $\sigma\left(\xi,t\right)$ that can be substituted into (3.7). This leads to the following:

$$\varphi^{nc}\left(\xi,t\right)=\varphi^1\left(\xi,t\right)+\varphi^2\left(\xi,t\right),\tag{3.12}$$

where

$$\varphi^1\left(\xi,t\right)=\frac{b}{2\pi}\sum_{i=1}^{n_{mo}}\dot{D}_i\left(t\right)f_{y,i}\left(\xi\right)\tag{3.13}$$

and

$$\varphi^2\left(\xi,t\right)=\frac{b}{2\pi}V_\infty\sum_{i=1}^{n_{mo}}D_i\left(t\right)f_{\partial y,i}\left(\xi\right),\tag{3.14}$$

with $f_{y,i}(\xi)$ and $f_{\partial y,i}(\xi)$ defined as

$$f_{y,i}(\xi) = \int_{-1}^{1} y_i(\xi_1) \ln\left(\frac{(\xi-\xi_1)^2 + \left(\sqrt{1-\xi^2} - \sqrt{1-\xi_1^2}\right)^2}{(\xi-\xi_1)^2 + \left(\sqrt{1-\xi^2} + \sqrt{1-\xi_1^2}\right)^2}\right) d\xi_1 \tag{3.15}$$

$$f_{\partial y,i}(\xi) = \int_{-1}^{1} y_i'(\xi_1) \ln\left(\frac{(\xi-\xi_1)^2 + \left(\sqrt{1-\xi^2} - \sqrt{1-\xi_1^2}\right)^2}{(\xi-\xi_1)^2 + \left(\sqrt{1-\xi^2} + \sqrt{1-\xi_1^2}\right)^2}\right) d\xi_1. \tag{3.16}$$

Note that these integrals come from the integral in (3.7) and are functions of only the predetermined $y_i(\xi)$, hence, can be calculated prior to any temporal simulations. Efficient time simulations are vital if they are to be used within a design optimisation algorithm.

3.1.4 Circulatory Potential

The circulatory potential is driven by the unsteady wake that is convected downstream of the aerofoil. This wake contains information about the history of the flow around the aerofoil and it is assumed that the wake convects downstream linearly at the free stream velocity V_∞. The derivation on the circulatory potential follows the same principles as the non-circulatory, with the aerofoil modeled as a distribution of point vortices and a Neumann boundary condition being enforced. However, a further condition, on the fluid's circulation, is enforced to physically realise the flow. Circulation is defined by a closed-path line integral,

$$\Gamma := \oint_{\Omega_{\mathcal{F}}} \mathbf{u}.d\boldsymbol{\xi}. \tag{3.17}$$

Whenever Bernoulli's equations holds the flow will have a constant circulation for a given fixed closed-path, this is often refereed to as *Kelvin's Theorem.* Hence, we can also enforce the condition that

$$\frac{d\Gamma}{dt} = 0. \tag{3.18}$$

This is achieved by including a unsteady wake, modeled as a distribution of point vortices being convected downstream from the trailing edge. The magnitude of the wake vortices is equal to the circulation created on the aerofoil, by the dynamic motion, but opposite in sign thus keeping the circulation constant. A further condition also needs to be enforced, namely the *Kutta Condition*. This ensures the flow is unique and that the flow is not singular at the trailing edge, i.e

$$\lim_{\xi \to 1} \left| \frac{\partial \varphi\left(\xi\right)}{\partial \xi} \right| < \infty. \tag{3.19}$$

Theodorsen [51] showed that the velocity potential at ξ due to a point vortex of strength $-\Delta\gamma$ located at $1 < \xi_0 < \infty$ and one of strength $\Delta\gamma$ at $\frac{1}{\xi_0}$ is given by,

$$\varphi_{\xi_0}\left(\xi\right) = -\frac{\Delta\gamma}{2\pi} \arctan\left(\frac{\sqrt{1-\xi^2}\sqrt{\xi_0^2 - 1}}{1 - \xi\xi_0} \right). \tag{3.20}$$

Although $\Delta\gamma$ is still unknown fluid field resulting from this potential does satisfy Kelvin's Theorem (3.18). If we define $\Delta\gamma := \gamma\left(\xi_0\right) d\xi_0$ we can then sum the effect of these point vortices over the wake, i.e. from $\xi_0 = 1$ to $\xi_0 = \infty$, for an expression for the circulatory potential

$$\varphi^c(\xi, t) = -\frac{1}{2\pi} \int_1^\infty \gamma(\xi_0) \arctan\left(\frac{\sqrt{1-\xi^2}\sqrt{\xi_0^2 - 1}}{1 - \xi\xi_0} \right) d\xi_0. \tag{3.21}$$

The non-circulatory potential (3.12) and the circulatory potential from the whole wake are summed and differentiated to give,

$$\begin{aligned}\lim_{\xi\to 1}\frac{\partial\varphi\left(\xi\right)}{\partial\xi} &= \lim_{\xi\to 1}\frac{\partial}{\partial\xi}\left(\varphi^{nc}\left(\xi\right)+\varphi^{c}\left(\xi\right)\right)\\ &= \lim_{\xi\to 1}\left(\frac{1}{\sqrt{1-\xi}}\left[\frac{1}{2\pi}\int_{1}^{\infty}\frac{\sqrt{\xi_0+1}}{\sqrt{\xi_0-1}}\gamma\left(\xi_0\right)d\xi_0+\frac{1}{2\pi}V_\infty\sum_{i=1}^{N}D_i\left(t\right)H_{dyd\xi,i}\dots\right.\right.\\ &\qquad\left.\left.+\frac{1}{2\pi}\sum_{i=1}^{N}\dot{D}\left(t\right)H_{y,i}\right]\right),\end{aligned} \tag{3.22}$$

where the mode shape integrals $H_{y,i}$ and $H_{dy,i}$ are given by,

$$H_{y,i} = -2\int_{-1}^{1}\frac{y_i\left(\xi_1\right)\sqrt{1-\xi_1^2}}{\xi_1-1}d\xi_1 \tag{3.23}$$

$$H_{dy,i} = -2\int_{-1}^{1}\frac{y'\left(\xi_1\right)\sqrt{1-\xi_1^2}}{\xi_1-1}d\xi_1. \tag{3.24}$$

Now $\gamma(\xi_0)$ can be chosen, implicitly, using the Kutta condition in (3.19), so that (3.22) is finite. We define

$$Q := \frac{1}{2\pi}\int_{1}^{\infty}\frac{\sqrt{\xi_0+1}}{\sqrt{\xi_0-1}}\gamma\left(\xi_0\right)d\xi_0 = -\frac{1}{2\pi}V_\infty\sum_{i=1}^{N}D_i\left(t\right)H_{dy,i}-\frac{1}{2\pi}\sum_{i=1}^{N}\dot{D}\left(t\right)H_{y,i}. \tag{3.25}$$

Since this is only a implicit expression for $\gamma\left(\xi_0\right)$ a new function **C**, Theodorsen's function [51], is defined so the circulatory lift and circulatory moment do not directly depend on $\gamma\left(\xi_0\right)$. Theodorsen's function is defined as,

$$\mathbf{C}\left(\gamma\right) = \frac{\int_{1}^{\infty}\frac{\xi}{\sqrt{\xi^2-1}}\gamma\left(\xi\right)d\xi}{\int_{1}^{\infty}\frac{\xi+1}{\sqrt{\xi^2-1}}\gamma\left(\xi\right)d\xi}. \tag{3.26}$$

Theodorson [51] continues to show that if $\gamma\left(\xi_0\right)$ is assumed to take the form of a traveling wave, i.e. $\gamma\left(\xi\right) = \gamma_0 e^{i\left(k\left(V_\infty t-\xi\right)\right)}$, then the integrals in (3.26) are known and reduce to a ratio of Hankel functions

$$\mathbf{C}\left(k\right)=\frac{H_1^{(2)}\left(k\right)}{H_1^{(2)}\left(k\right)+iH_0^{(2)}\left(k\right)}, \tag{3.27}$$

where $k=\omega b/V_\infty$ is a reduced frequency.

3.1.5 Aerodynamic States

For the unsteady wake effects, captured within the circulatory potential, to be written in state-space form they must be approximated, as in the work of Von Karman and Sears [129]. This is achieved in two parts. Firstly, one could use a rational function approximation of (3.27) or equivalently, as is done here, approximate the Wagner function $\Phi(s)$, which is simply a Laplace transformation the of the Theodorson function, with an exponential series, i.e

$$\Phi\left(s\right)=1-\sum_{j=1}^{n_{\text{in}}}a_j\exp\left(-b_js\right) \tag{3.28}$$

where $s=\frac{Vt}{b}$ is the non-dimensional time, $\{a_j\}\in\mathbb{R}$ and $\{b_j\}\in\mathbb{R}$ are curve fitted by least squares to the Wagner function and n_{in} is the number of approximation terms used. The second step is to introduce a new set of variables that allow the time lag effects to be linearised. New states are introduced, namely the *aerodynamic states*, so an approximation on the product of Q, from (3.25), and $\mathbf{C}$, from (3.27), can be be made such that,

$$Q\mathbf{C}=Q\left(t\right)\left(1-\sum_{j=1}a_j\right)+\sum_{j=1}z_j. \tag{3.29}$$

The z_j make up the Duhamel integral part of the time-lag effects and can be written as

$$z_j\left(t\right)=\frac{b_ja_jV_\infty}{b}\int_0^t\left(Q\left(t'\right)e^{-\frac{b_jV}{b}\left(t-t'\right)}\right)dt'. \tag{3.30}$$

When the aerodynamic states are written explicitly in this form it is easy to see that they contain information of the history of the aerodynamics, since the integral is from $t' = 0$ until $t' = t$ (3.30) can be differentiated to find a linear ordinary differential equation for the aerodynamic states, i.e

$$\dot{z}_j + \frac{b_j V_\infty}{b} z_j = \frac{b_j a_j V_\infty}{b} Q(t) . \tag{3.31}$$

Equation (3.31) shows that the aerodynamic states decay exponentially, when unforced, with inputs from the rigid body motion and deformation states.

3.1.6 Forces and Moments

By integrating over the pressure difference, (3.6), the following expressions for the normal force, $\mathcal{N}$, and moment about the leading edge, $\mathcal{M}_{LE}$, are arrived at,

$$\mathcal{N} = b \int_{-1}^{1} \Delta p(\xi) \, d\xi \tag{3.32}$$

and

$$\mathcal{M}_{LE} = -b^2 \int_{-1}^{1} (\xi + 1) \Delta p(\xi) \, d\xi, \tag{3.33}$$

here we define a clockwise moment as positive. The moment about any point, $-1 \leq \xi \leq 1$, is given by,

$$\mathcal{M}(\xi) = \mathcal{M}_{LE} + \mathcal{N} b (1 + \xi) . \tag{3.34}$$

The normal force due to non-circulatory effects is given by,

$$\begin{aligned}\mathcal{N}^{nc} &= \int_{-1}^{1} \Delta p^{nc} d\xi \\ &= b\int_{-1}^{1} 2\rho\left(\dot{\varphi} + V_{\infty}\varphi'\right) d\xi \\ &= \sum_{i=1}^{n_{mo}} b\int_{-1}^{1} 2\rho\left(\left[\frac{b}{2\pi}\ddot{D}_i f_{y,i} + \frac{b}{2\pi}V_{\infty}\dot{D}_i f_{\partial y,i}\right] + V_{\infty}\varphi'\right) d\xi \\ &= \frac{\rho b^2}{\pi}\sum_{i=1}^{n_{mo}}\left(\ddot{D}_i\left(t\right)F_{y,i} + V_{\infty}\dot{D}_i\left(t\right)F_{\partial y,i}\right) + 2\rho V_{\infty}\underbrace{\left[\varphi\left(\xi\right)\right]_{-1}^{1}}_{=0},\end{aligned} \tag{3.35}$$

the last term vanishes due to its definition in (3.7), while the new terms are defined as

$$F_{y,i} = \int_{-1}^{1} f_{y,i}\left(\xi\right) d\xi \tag{3.36}$$

and

$$F_{\partial y,i} = \int_{-1}^{1} f_{\partial y,i}\left(\xi\right) d\xi. \tag{3.37}$$

The lift, $\mathcal{N}$, and moment force, $\mathcal{M}$, can be thought as an input to the rigid body motion in heave and pitch. They are functions of the aerodynamics only and will act as forcing terms to the structure.

3.1.7 Heave Motion and Pitch Motion

With expressions for the lift and moment lineraised with the aid of the additional aerodynamic states the equations of motion for heave and pitch can be formulated. Firstly, any point on the aerofoil will experience a local accelation of,

$$\Omega\left(\xi, t\right) = \ddot{Y}\left(t\right) + \ddot{\alpha}\left(t\right)\left(\xi_{ea} - \xi\right)b + \sum_{i=3}^{n_{mo}}\ddot{D}_i\left(t\right)y_i\left(\xi\right). \tag{3.38}$$

Hence, using Newton's second law of motion one can write,

$$\int_{-1}^{1} m(\xi)\,\Omega(\xi,t)\,d\xi + k_Y Y(t) = \mathcal{N}(t) \tag{3.39}$$

where $\mathcal{N}$ is the total normal force given by (3.32) and k_Y is the heave linear spring stiffness. Similarly, the equation for pitch motion is given by

$$b\int_{-1}^{1} (\xi-\xi_a)\,m(\xi)\,\Omega(\xi,t)\,d\xi + k_\alpha \alpha(t) = \mathcal{M}(\xi_{ea}) \tag{3.40}$$

where $M(\xi_{ea})$ is defined in (3.34) and k_α is the pitch linear spring stiffness.

3.1.8 Compliant aerofoil structural model

The deformation of the of the aerofoil $\tilde{y}(\xi,t)$ is defined as the motion of the camberline independent of the heave and pitch motion. The dynamics of the deformations are approximated using an Euler-Bernoulli model,

$$\frac{\partial^2}{\partial\xi^2}\left(EI\frac{\partial^2\tilde{y}}{\partial\xi^2}\right) + \rho(\xi)\frac{\partial^2\tilde{y}}{\partial t^2} = \Delta p(\xi,t) + P_{fi}(\xi,t), \tag{3.41}$$

where $\rho(\xi)$ is the local density of the beam and P_{fi} are the local fictitious inertial force due to the beam not being in an inertial frame, i.e. the beam will feel forces due to its own acceleration. The second order derivative in time leads to oscillating solutions (when stable), which is physically what would be expected of stiff beam. The acceleration of the local frame of reference is given by

$$\Omega_{\text{frame}}(\xi,t) = \ddot{Y}(t) + \ddot{\alpha}(t)(\xi_{ea}-\xi)\,b, \tag{3.42}$$

which implies

$$P_{fi} = -\Omega_{\text{frame}}(\xi, t)\,\rho(\xi) = -\left(\ddot{Y}(t) + (\xi_{ea} - \xi)\,b\ddot{\alpha}(t)\right)\rho(\xi)\,. \tag{3.43}$$

Since the Euler-Bernoulli equation is an infinite dimensional, locally defined, PDE, it is useful approximate the equation by projecting it onto a finite space as already done for the aerodynamic in (3.1). A typical method is to use the beam's free vibration modes $\{y_i(\xi)\}_{i=3}^{n_{mo}}$ so that the beam's motion is approximated by

$$\tilde{y}(\xi, t) \approx \sum_{i=3}^{n_{mo}} y_i(\xi) D_i(t). \tag{3.44}$$

Physically, if the beam was held in vacuum in the shape of an eigenmode $y_i(\xi)$ it would oscillate at a frequency of ω_i when released. The vibration modes are defined by (3.45),

$$\frac{\partial^2}{\partial \xi^2}\left[EI\frac{\partial^2 y_i}{\partial \xi^2}\right] - \omega_i^2 m_i y_i = 0 \qquad \text{for } i = 3, \ldots, n_{mo}. \tag{3.45}$$

where the modal mass m_k is defined by,

$$\int_{-1}^{1} y_i \rho y_k d\xi = m_i \delta_{ik} \qquad \text{for } k = 3, \ldots, n_{mo}. \tag{3.46}$$

Note that (3.46) also shows that the modes are orthogonal. Thus, the beam dynamics can be separated into $n_{mo} - 2$ ordinary differential equations that describe the aerofoil non-locally. To achieve this separation, (3.41) is multiplied by y_k and integrated over the length of the aerofoil,

$$m_i \ddot{D}_i + m_i \omega_i^2 D_i - b\int_{-1}^{1} y_k P_{fi}(\xi, t) d\xi - b\int_{-1}^{1} y_k \Delta p(\xi, t)\, d\xi = 0. \tag{3.47}$$

for $i, k = 3...n_{mo}$. To reduce (3.47) to an ODE the ξ and t dependencies still need to be separated in the integral terms. This is simple for the first integral,

$$\int_{-1}^{1} y_k P_{fi}(\xi, t) d\xi = -\ddot{Y}(t) \int_{-1}^{1} y_k \rho(\xi) d\xi - \ddot{\alpha}(t) b \int_{-1}^{1} y_k (\xi_{ea} - \xi) \rho(\xi) d\xi. \tag{3.48}$$

One can see that all the integrals (3.48) are constant once the mode shapes y_k and density ρ are chosen. Hence, they can be calculated ahead of any time domain simulations. The second integral, which uses the pressure difference defined in (3.6), also decomposes into a similar, albeit much longer, form. However, a key point that this work takes advantage of is that majority of the required integrals are linear in $y_i(\xi)$, as with the integrals in (3.48). Five of the integrals, all of which can be found in [128], are non-linear in $y_i(\xi)$, one such example is

$$PI9_{i,k} = \int_{-1}^{1} \frac{\partial f_{y,k}}{\partial \xi}(\xi_1) y_i(\xi_1) d\xi_1, \tag{3.49}$$

where $f_{y,i}(\xi)$ is defined in (3.15) and is a function of $y_i(\xi)$. The fact that most the integrals are linear in $y_i(\xi)$ will be used to accelerate the optimisation of an aerofoil with a compliant trailing edge flap as explained in Section 3.4.2.

This derivation from a one-dimensional Euler-Bernoulli allows for the modelling of 2D, potential, aerodynamics forces over an arbitrarily deforming camberline. Specifically, this approximation is only valid when the flow remains attached, i.e. high Reynolds numbers and low mach-numbers.

3.1.9 Open-loop State-Space form

To complete the formation of the aeroelastic model a external, a vertical gust model is included. This requires the introduction of new states $\{g_j\}_{j=1}^{n_{\mathrm{gu}}}$ similar to the aerodynamic states in Section 3.1.5. These new states are used as a finite approximation to the Küssner function so that unsteady effects of a vertical gust can be modeled.

The states are now aggregated into a single state vector,

$$\boldsymbol{x} = \left[Y, \alpha, \dot{Y}, \dot{\alpha}, D_1 ..., D_{n_{mo}}, \dot{D}_1 ..., \dot{D}_{n_{mo}}, z_1 ..., z_{n_{\mathrm{in}}} ..., g_1 ..., g_{n_{\mathrm{gu}}}\right]^\top, \tag{3.50}$$

where $\boldsymbol{x} \in \mathbb{R}^n$, with $n = 4 + 2n_{mo} + n_{\mathrm{in}} + n_{\mathrm{gu}}$. Note that the derivatives are also included in the state vector, this allows the system to be written as a first order ODE,

$$\dot{\boldsymbol{x}}\left(t\right) = A\boldsymbol{x}\left(t\right) + B_w w(t), \tag{3.51}$$

where $A \in \mathbb{R}^{n \times n}$, $B_w \in \mathbb{R}^n$ and the gust input $w(t) \in \mathbb{R}$. This system is built from the heave (3.39) and pitch (3.40) equations in Section 3.1.7, the beam model equations 3.47 in Section 3.1.8, the aerodynamic states equations (3.31) in Section 3.1.5 and a similar set equations for the unsteady gust input.

3.2 Aeroservoelastic Model

3.2.1 Trailing edge state

The use of multiple mode shapes to approximate the camberline can be used to model a flexible beam under aerodynamic forcing and fixed to springs at the elastic axis, as in [128]. Instead, we only concerned in creating a model that can be used in a computationally inexpensive aeroservoelastic design optimisation, rather than modelling chordwise flexibility. This can be achieved by using only one mode shape $y_i(\xi)$ to describe the motion of a compliant trailing edge flap. This does not limit the validity of the aerodynamics over this shape nor does it limit this model to a trivial design space. In fact, with the considerations made in this sub-section, the shape of the smoothly attached trailing edge flap can be designed with arbitrary precision. Although, it is unlikely that the manufacturing of a trailing edge flap that deforms as such is physically realisable it does allow this work to investigate a sufficiently computationally simple design optimisation that includes optimisation over aerodynamic design variables. In the context of more complex models with many degrees of freedom one could instead use aerodynamics design variables such as aspect ratio, wing twist, wing sweep etc.

The shape of the flap is defined by

$$y(t) := S\left(\xi\right) = \begin{cases} 0 & \text{for } \; -1 \leq \xi \leq \xi_h, \\ S_\beta\left(\xi\right) & \text{for } \quad \xi_h \leq \xi \leq 1, \end{cases} \tag{3.52}$$

where ξ is non-dimensionalised by the half-chord length, so that $-1 \leq \xi \leq 1$ from the leading edge to the trailing edge and ξ_h is the hinge point of the actuator. The shape function, $S_\beta\left(\xi\right)$, is defined by an arbitrary number of parameters s_r within a polynomial expansion about ξ_h,

$$S_\beta\left(\xi\right) = \frac{\left(1-\xi_h\right)}{\sum_{r=2}^{p} s_r} \sum_{r=2}^{p} s_r \frac{\left(\xi-\xi_h\right)^r}{\left(1-\xi_h\right)^r}. \tag{3.53}$$

Note that the series starts at $r = 2$ to ensure that the trailing edge attaches smoothly to the camberline. This formalisation allows for an aerodynamic variable to be optimised via the parameters s_r. The shape of the aerofoil at time t is given by,

$$\tilde{y}(\xi, t) := s\left(\xi, t\right) = \beta\left(t\right) S\left(\xi\right). \tag{3.54}$$

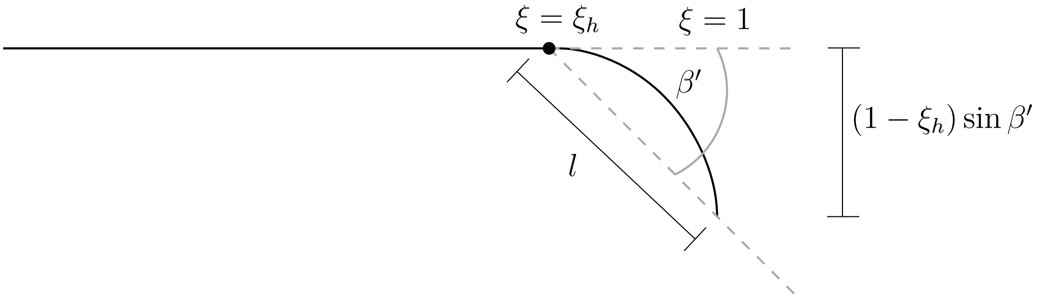

Figure 3.2: Definition of the trailing edge shape and its physical meaning.

Since the system is linear the scaling of this function is arbitrary. It has been chosen so that $S_\beta(1) = 1 - \xi_h$, meaning that for small angles the state $\beta(t)$ is approximately the angle of the flap. This is clarified in Figure 3.2: given an input $\beta(t)$, the angle β' made by joining the trailing edge of the aerofoil to the hinge point can be approximated by

$$\beta' \approx \sin\beta' = \frac{(1-\xi_h)}{l}\beta \approx \beta. \tag{3.55}$$

The dynamics of the trailing edge are derived from the Euler-Bernoulli model described in Section 3.1.8. The trailing edge is assumed to elastically oscillate around an input $u(t)$, which is described by

$$m_\beta\ddot{\beta}(t) + m_\beta\omega_\beta^2(\beta(t) - u(t)) = F(t), \tag{3.56}$$

where F represents the aerodynamic and inertial generalised forces acting on the trailing edge [128], and m_β is given by

$$m_\beta = b^3\int_{-1}^{1}\rho(\xi)\,S_\beta^2\,d\xi. \tag{3.57}$$

where b is the semi-chord and $\rho(\xi)$ is the density of the aerofoil, described in the next section.

The open-loop state-space of this system is given by,

$$\dot{\boldsymbol{x}}(t) = A\boldsymbol{x}(t) + B_w w(t) + B_u u(t), \tag{3.58}$$

where $B_u \in \mathbb{R}^n$ and $x \in \mathbb{R}^n$, with $n = 6 + n_{\text{in}} + n_{\text{gu}}$, is given by

$$\boldsymbol{x} = \left[Y, \alpha, \dot{Y}, \dot{\alpha}, \beta, \dot{\beta}, z_1 ..., z_{n_{\text{in}}} ..., g_1 ..., g_{n_{\text{gu}}}\right]^\top . \tag{3.59}$$

Note this is a special case of the generalisation made in 3.59 as the mode shapes defining the aerofoil's deformation have been limited to only describing the deformation of a compliant trailing edge flap.

3.2.2 Mass distribution

Since the aerofoil model is a lumped-parameter structural dynamics model mass and stiffness can be assigned independently. We will enforce that stiffening the aerofoil will require adding more mass. Hence the density of the aerofoil is modeled as,

$$\rho(\xi) = \begin{cases} \rho_r \left(\omega_y^2 + \omega_\alpha^2\right) & \text{for } -1 \leq \xi < \xi_h, \\ \rho_r \omega_\beta^2 & \text{for } \quad \xi_h \leq \xi \leq 1, \end{cases} \tag{3.60}$$

where ω_y and ω_α are the heave and pitch natural frequencies of the linear springs seen in Figure 3.1 and $\rho_r = 1\, kgs^2m^{-1}$ is a constant of proportionality between the frequencies and density. Integrating this density distribution over the aerofoil gives a total mass of

$$M_{tot} = b\rho_r \left((1 + \xi_h)\left(\omega_y^2 + \omega_\alpha^2\right) + (1 - \xi_h)\,\omega_\beta^2\right). \tag{3.61}$$

It can be observed that a stiffer wing, with higher natural frequency, will be heavier. If one was investigating a higher fidelity model mass and stiffness might not be independent, for example, for a structural box model of cantilever wing the geometry of the box prescribes the mass and stiffness.

3.2.3 Controller and Observer

An LQG controller and observer will be created for the aerofoil to form the control input $u(t)$ from pressure sensors on the chord. The controller and observer can be designed separately. The controller is defined by a linear quadratic minimisation

$$\min_{K} \int_0^T \left(Q_y Y^2(t) + Q_\alpha \alpha^2(t) + R(K\boldsymbol{x})^2(t) \right) dt, \tag{3.62}$$

where Q_y and Q_α are control weightings to be used as design variables, whereas R penalises the control input and is given by

$$R = (1 - \xi_h)\,\omega_\beta^2. \tag{3.63}$$

Therefore, the input penalty is proportional to the mass of the flap, i.e. a heavy flap would require more control energy. Note that Q_y, Q_α and R must be positive for a solution to (3.62) to exist.

The observer dynamics are formed from a series of pressure sensors and the control input,

$$\boldsymbol{y}(t) = C\boldsymbol{x}(t) + Du(t), \tag{3.64}$$

for matrices $C \in \mathbb{R}^{n_p \times n}$, where n_p is the number of pressure sensors. The estimated state vector $\hat{\boldsymbol{x}}$ satisfies,

$$\dot{\hat{\boldsymbol{x}}} = A\hat{\boldsymbol{x}} + B_u u + L(\boldsymbol{y} - C\hat{\boldsymbol{x}}). \tag{3.65}$$

The observer gain $L \in \mathbb{R}^{n \times n_p}$ is calculated by the Kalman filter problem [130],

$$\min_{L} \lim_{t\to\infty} E\left[(\boldsymbol{x}(t) - \hat{\boldsymbol{x}}(t)) (\boldsymbol{x}(t) - \hat{\boldsymbol{x}}(t))^T \right], \tag{3.66}$$

where $E[.]$ is the expectation in response to a stochastic input with known variance. Both K and L are found using the `lqr` and `kalman` packages in MATLAB that solve (3.62) and (3.66) via Riccati equations.

To restrict the authority of the control saturation has been introduced. Note that this is the only non-linear component of the model. The addition of saturation introduces a physical limit on the performance of the controller. The saturation model is

$$u(t) = \begin{cases} u_+ & \text{for} \quad u > u_+, \\ K\hat{\boldsymbol{x}}(t) & \text{for} \quad |u| \leq u_+, \\ -u_+ & \text{for} \quad u < -u_+. \end{cases} \tag{3.67}$$

Low control activity is not optimal for performance but a controller that acts too aggressively leads to a system with too much saturation, which in this model leads to unstable dynamics. For all results presented in this work, the saturation limit of $u_+ = 5^\circ$ is imposed. One would also expect saturation to be included, as it is here, in models of higher complexity. Note, when modelling aerodynamic and/or structural non-linearities, such as the saturation described above, time-domain considerations are often required [14].

3.2.4 Model Parameters

Not all the parameters within the model have been discussed, however, Table 3.1 lists those remaining parameters needed to reproduce the current model. The density of air affects the matrices A, B_u and B_w in (3.58) as described by Gaunaa [128].

Parameter description	Value
Density of air	$1\,kgm^{-3}$
Length of the chord	$2\,m$
Position of elastic axis	$\xi_{ea} = -0.4$
Flap hinge	$\xi_h = 0.8$

Table 3.1: Remaining model parameters.

3.3 Optimisation

3.3.1 Design variables

With the goal to optimise a full ASE system the design variables chosen have been taken from each of the three fields: structral, aerodynamic and control. First, structural parameters are chosen to be ω_y, ω_α and ω_β; the natural frequencies of the heave, pitch and trailing edge. These are not only proxies for the flexibility of aerofoil but also define the total mass and the position of the centre of mass, which characterises the stability of the system. The control law will also be optimised by means of the variables Q_y and Q_α, introduced in (3.62). These variables will weight the control law on whether to preference either the heave or pitch motions when stabilising the system. The aerodynamic shaping, i.e. the trailing edge, will be achieved by design of the polynomial coefficients in (3.53). In this investigation, only two of these coefficients will be optimised over, s_2 and s_3, the rest will be set to zero. Finally, the placement of two pressure sensors on the camberline, p_1 and p_2, will be designed as to optimise the observer design. In summary there are nine design variables in the design vector X,

$$X = \begin{pmatrix} \omega_y & \omega_\alpha & \omega_\beta & Q_y & Q_\alpha & s_2 & s_3 & p_1 & p_2 \end{pmatrix}^T . \tag{3.68}$$

3.3.2 Cost function

The cost function to be minimised during the aerofoil design is made up of both a static measure of performance and a dynamic performance measure, the reason for this choice is justified Section 4.2.1. This work, as described in Chapter 1, is motivated by increasing demand for efficient aircraft, which can be physically limited by an aircraft's mass. Hence, the static measure $J_1(X)$ is the total mass, a common attribute in which a reduction is sought. Specifically, this is given in (3.61), that is,

$$J_1(X) = M_{tot} = b\rho_r\left((1+\xi_h)\left(\omega_y^2+\omega_\alpha^2\right)+(1-\xi_h)\,\omega_\beta^2\right). \tag{3.69}$$

The dynamic measure $J_2(X)$ of the aerofoil is defined by the time integral of the total elastic energy of the system,

$$J_2(X) = \int_0^T \left[k_y Y^2(X;t) + k_\alpha \alpha^2(X;t)\right] dt, \tag{3.70}$$

where $k_y = M_{tot}\omega_y^2$ is the heave spring stiffness, $k_\alpha = I_{tot}\omega_\alpha^2$ is the pitch spring stiffness, T defines the time interval being considered and I_{tot} is the total moment of inertia of the aerofoil. It is shown in Chapter 4 that a time-domain metric such as this is important in the context of a saturated model. For example, if the states Y and α diverge in the interval $[0,\, T]$ one would expect a relatively large $J_2(X)$, thus biasing the optimiser to designs that do not diverge, at least in the chosen interval. This motion is in response to a vertical gust input given by,

$$w(t) = \begin{cases} w_0\left(1-\cos\left(\frac{\pi V t}{l}\right)\right) & \text{for } 0 \leq t \leq \frac{2l}{V} \\ 0 & \text{else} \end{cases}, \tag{3.71}$$

where V is the test free-stream velocity of the aerofoil, w_0 is the amplitude of the gust and l is the length of the gust. A value of $T = 50$ was chosen as it is large enough to allow for any transient motion to decay, while not causing excessive computational effort. The external disturbance, w, feeds into the dynamics via (3.58). This objective function minimises the stress over a gust response explicitly. This would be key if the design's longevity and reliability were important as minimising stress will lower long term fatigue. This choice of cost function is further explored comprehensively in Section 4.2 and expanded to include a range of responses from numerous gusts, a common industry practice. The total cost function $J\left(X\right)$ will simply be given by

$$J\left(X\right) = J_1\left(X\right) + J_2\left(X\right). \tag{3.72}$$

3.3.3 Constraints

The optimisation will be constrained by two non-linear constraints and by bounds on the design vector.

Design vector bounds: These bounds ensure that the solution is physical, for example, that the mass is non-negative and that the pressure sensors are on the aerofoil. The design vector will be rescaled by these upper and lower limits so that each component is between 0 and 1, i.e $0 \leq X_i \leq 1$ for all i. This normalisation will facilitate the comparison of the variability of each design variable over an optimisation.

Flutter speed: Flutter is a dynamic instability that in linear models lead to oscillatory and divergent wing responses, whereas, in non-linear models flutter is normally characterised by limit cycle oscillations. The closed-loop linear flutter speed is defined as the lowest positive free-stream velocity in which the closed-loop dynamics are linearly unstable. Specifically, in this model the lowest velocity such that there exists an eigenvalue of $A - B_u K$ with a non-negative real part. Note that A, B_u and K are all functions of V. A constraint on this linear flutter speed will be enforced. To mimic a flight safety margin, the aerofoil will be constrained to experience a free-stream velocity of 80% of its linear flutter speed, i.e.

$$V \leq 0.8 V_F, \tag{3.73}$$

where V_F is the linear flutter speed defined as

$$V_F(X) := \sup\{V : \mathrm{Re}(\lambda_i(A - B_u K)) < 0, \text{ for all } i = 1, \ldots, N+6\}. \tag{3.74}$$

$$c_1(X) = V - 0.8 V_F \leq 0. \tag{3.75}$$

This is a key constraint that is considered early in the design process of real aircraft, furthermore, the physical aircraft's flutter speed is extensively investigated as part of the test flights.

Trailing edge shape: It is expected that a trailing edge with larger arc length will be advantageous to the controller, since in this case it will be able to generate a bigger force with the larger surface. Hence, if no constraint is imposed, optimal designs will often have non-monotonic trailing edges, which are physically unrealistic. As such it is necessary to implement a constraint on the trailing edge to ensure it remains monotonic. This can be achieved by,

$$\frac{d}{d\xi} S_\beta(\xi) \leq 0, \qquad \xi_h \leq \xi \leq 1, \tag{3.76}$$

where S_β is defined in (3.53). This constraint will be written as,

$$c_2\left(X\right) = \max\left\{\frac{dS_\beta}{d\xi}\left(\epsilon\right) : \xi_h \leq \epsilon \leq 1\right\} \leq 0. \tag{3.77}$$

Now, concatenating the non-linear inequalities as $c = \left[c_1, c_2\right]^\top$ the optimisation problem can be written as,

$$\min_X J\left(\boldsymbol{x}(X),\, X\right) \tag{3.78}$$

$$\text{such that } \bar{\mathcal{A}}\left(\boldsymbol{x}(X),\, X\right) = 0, \tag{3.79}$$

$$c\left(X\right) \leq 0, \tag{3.80}$$

$$0 \leq X \leq 1. \tag{3.81}$$

3.4 Optimisation Implementation

3.4.1 Solution method

Throughout the paper optimisations are performed using a gradient based interior point algorithm within the MATLAB `fmincon` function. Interior point algorithms can be used to minimise non-linear cost-functions constrained by non-linear functions either by equality or inequality relationships. The interior point algorithm works by instead solving a sequence, in $\mu > 0$, of equality constrained problems defined by

$$\min_{X,\,C} J\left(X\right) - \mu \sum_{i} \ln\left(C_i\right), \tag{3.82}$$

$$\text{such that } \bar{\mathcal{A}}\left(X\right) = 0, \tag{3.83}$$

$$c\left(X\right) + C = 0, \tag{3.84}$$

$$0 \leq X \leq 1. \tag{3.85}$$

where there are as many C_i as there were inequality constraints. The goal of an interior point algorithm is that as μ decreases the solution to this approximate minimisation problem should tend to the solution of the original problem. In Chapter 4 information about the Hessian is not passed to MATLAB and hence the approximate minimisation problem is solved by Newton steps in $(X,\, C)$ using approximations of the Hessian. Iterations are stopped when $|X_n - X_{n-1}| < \epsilon$, where ϵ is the design vector tolerance condition. One can also consider a measure of first-order optimality, which are based on the Karush-Kuhn-Tucker conditions and can be outputted by `fmincon`, to further assess whether if the iterations have terminated due to finding a minimum or the algorithm has simply satisfied the design vector tolerance condition. It must be noted that first-order optimality equal to zero is a necessary condition for a minimum but not a sufficient condition.

3.4.2 Optimisation acceleration

As mentioned in Section 3.1.8 there are a number of integrals that can be computed “offline” before any time simulations greatly decreasing the computational effort. Further acceleration is possible for investigating different designs. Many of the required integrals are linear in the mode shape, which in our example is given be $S_\beta(\xi)$ defined in (3.53), i.e if

$$S_\beta(\xi) = \gamma^1 S^1_\beta(\xi) + \gamma^2 S^2_\beta(\xi) \tag{3.86}$$

then

$$\mathcal{I}(S_\beta(\xi), \xi) = \gamma^1 \mathcal{I}(S^1_\beta(\xi), \xi) + \gamma^2 \mathcal{I}(S^2_\beta(\xi), \xi), \tag{3.87}$$

where $\mathcal{I}(S_\beta(\xi), \xi)$ is an example of one of said linear integrals. Using this, the majority of the required integrals can be computed over the entire design space by first calculating

$$\mathcal{I}^2 = \mathcal{I}((\xi - \xi_h)^2, \xi) \qquad \text{and} \qquad \mathcal{I}^3 = I((\xi - \xi_h)^3, \xi). \tag{3.88}$$

Then for any point in design space the linear integrals are known and equal to,

$$\mathcal{I}(S_\beta(\xi), \xi) = \frac{(1 - \xi_h)}{\sum_{r=2}^{3} s_r} \sum_{r=2}^{3} s_r \frac{\mathcal{I}^r}{(1 - \xi_h)^r}. \tag{3.89}$$

Chapter 4

Design Optimisation of an Aeroservoelastic Aerofoil

This chapter uses the model described in Chapter 3 as a test bed for aeroservoelastic design optimisation. The aeroelastic model is first used in a relatively simple design optimisation to highlight how complexities in the design space can limit a gradient based optimiser. Subsequently the aeroservoelastic system is investigated. Initially a frequency-domain constraint is considered in an attempt to limit the effects of the control saturation on the design optimisation. It is concluded that frequency-domain metrics would be insufficient, justifying the use of a time-domain statistic in the cost-function. Finally, the full design optimisation problem is evaluated using the algorithms described in Chapter 2.

4.1 Model Verification

Verification of the implementation of the ASE model was accomplished by setting the shape of the trailing edge to a flat plate, i.e.

$$S_\beta\left(\xi\right) = \begin{cases} 0 & -1 \leq \xi \leq \xi_h, \\ \\ \left(\xi_h - \xi\right) & \xi_h \leq \xi \leq 1. \end{cases} \tag{4.1}$$

A plot of non dimensional flutter speed against the non dimensionalised hinge spring frequency for the three degree of freedom (heave, pitch and flap rotation) linear system, has been compared to those by Zeiler [131] with Figure 4.1 indicating that there is excellent agreement between both implementations. The evaluation of the current model requires the computation of integrals such as the ones described in (3.15) and (3.16), which here is achieved by discretising the chord into 100 uniform segments and integrating with the trapezium rule. A discretisation of 100 was chosen as when compared to a discretisation of 50 the non-dimensional flutter speed had a relative percentage difference of 0.001%, hence it was concluded that sufficient convergence had been achieved. Furthermore, a discretisation of 100 has been implemented throughout the remainder of the Chapter.

To further ensure the reliability of the solutions a study was conducted to insure time domain results were independent of the time step δt. The study performed simultaneous optimisations on 100 randomly selected initial design conditions $(X_0^i)_{i=1}^{100}$ and converged to 100 final designs $(X_*^i)_{i=1}^{100}$. The cost function $J(X_*^i;\, \delta t)$ of these final designs was evaluated using a $\delta t = 10^{-2}\, s$ or $10^{-3}\, s$ and it was found that $\max_i \left|\frac{J(X_*^i;\, 10^{-2}) - J(X_*^i;\, 10^{-3})}{J(X_*^i;\, 10^{-2})}\right| < 0.0001$. Hence, it was concluded that a $\delta t = 10^{-2}\, s$ was sufficient for the results presented here.

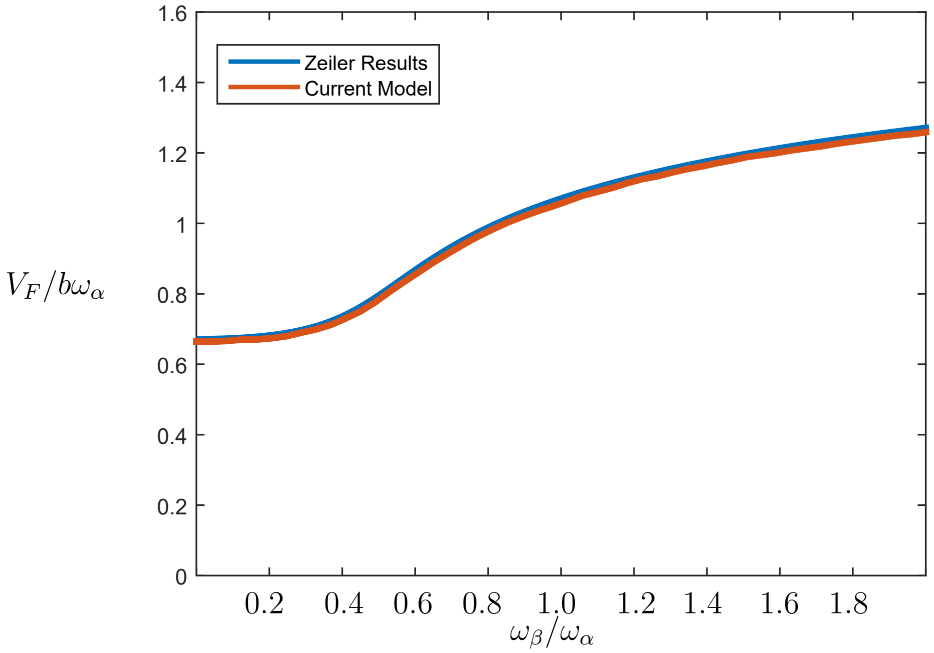

Figure 4.1: Non-dimensional flutter speed, $V_f/(b\omega_\alpha)$ against a non-dimensionalised hinge spring frequency, $\omega_\beta/\omega_\alpha$ for a flat plate, flat flap camberline model. The current code is compared to results from [131].

4.2 Structural Optimisation

To clearly demonstrate how design space complexities can cause sensitivity to initial conditions in a design optimisation we initially investigate a relatively simply problem. Consider the problem in which only the natural frequencies ω_y, ω_α are optimisation variables, and that the system is uncontrolled. That is, $Q_y = 0 = Q_\alpha$ defined in (3.62), the measurement locations p_1, p_2, which characterise the matrix C defined in (3.64), are not required, and ω_β, s_2, s_3 are fixed[1]. We consider the problem of minimizing the total mass M_{tot}, given by (3.61), subject to the simple dynamic constraint that the open-loop system (3.58) is asymptotically stable, i.e. flutter free. This corresponds to solving

---

[1] For the example in this section, $\omega_\beta = 5, s_2 = 0.2, s_3 = -0.3$

$$\begin{aligned} \min_{\omega_y,\omega_\alpha} \quad & \omega_y^2 + \omega_\alpha^2 \\ \text{subject to} \quad & \mathrm{Re}(\lambda_i(A)) < 0, \quad i = 1, \ldots, N+6, \end{aligned} \tag{4.2}$$

where $\lambda_i(A)$ denotes the ith eigenvalue of the state matrix A.

Feasible regions of the $(\omega_y, \omega_\alpha)$ design space are indicated in Figure 4.2 (a) with dark grey-shaded areas indicating parameter values corresponding to unstable dynamics. Interactions between the three structural frequencies contribute to open-loop instability in the regions $\omega_\alpha \approx \omega_y$ and $\omega_\beta \lesssim \omega_\alpha, \omega_y \lesssim 2\omega_\beta$, with the resulting lack of design-space connectedness influencing the performance of a gradient-based optimisation strategy, as those discussed in 1.1.2. For example, each of the three feasible regions in Figure 4.2 satisfying $\omega_\alpha \geq 10$ possess a clear local minimum with respect to the cost $\omega_\alpha^2 + \omega_y^2$, and an optimisation initialized each such region converges to the respective local minimum (selected optimisation trajectories are shown with initial condition a solid square and converged solution a solid disc). The region of design space containing the global minimum, which for this example lies at approximately $\omega_\alpha \approx 2.5 \approx \omega_y$, is highlighted in Figure 4.2 (b). The fact that the minimum lies in a *cusp* of design space contributes to the fact that its region of attraction (i.e., the set of initial conditions which converge to it—shaded light-grey) is severely restricted. This has important implications for optimisation strategies: even for such a simple example, the complexity of the design space can be such that the global minima (or even the local minima at $(\omega_\alpha, \omega_h) \approx (1, 5)$) are only obtained from small subsets of design space. Consequently, a large sample of initial conditions—and a consequent increase in computational cost—may be required to explore the full range of designs using a given optimisation strategy. Furthermore, since this example is perhaps the simplest that can be considered within the chosen aeroelastic framework, it is not unreasonable to expect that adding extra design variables or

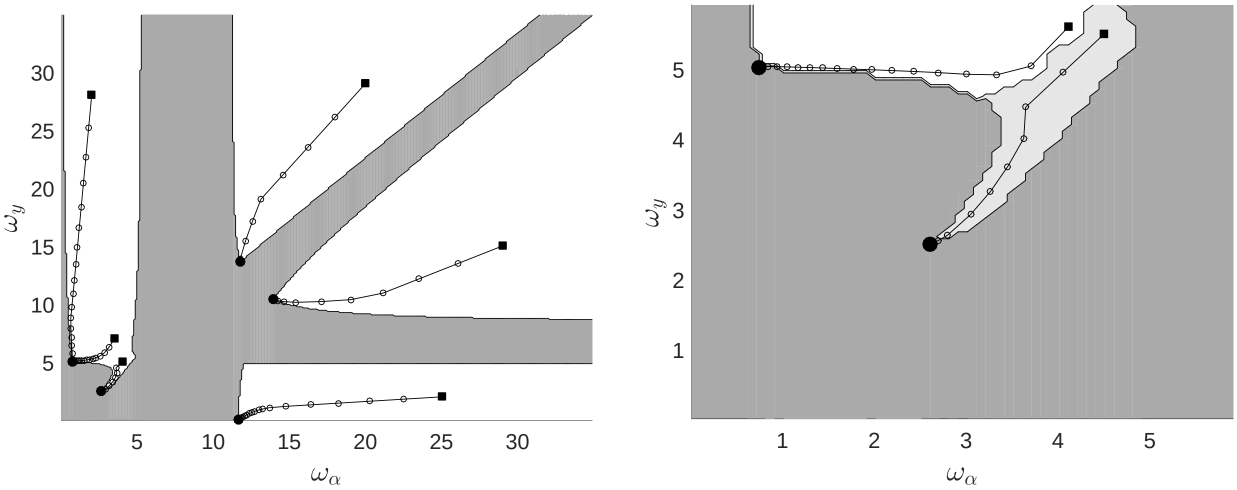

Figure 4.2: (a) Convergence of gradient-based optimisation trajectories to minimize $\omega_\alpha^2 + \omega_y^2$ subject to a flutter constraint with $\omega_\beta = 5$. (b) Neighbourhood of the global minimum its basis of attraction (light-gray area).

imposing additional constraints will only lead to a further increase in design-space complexity. However, such a pessimistic view is not entirely accurate, as we will see next. Figure 4.3 provides an example in which an expansion of design space is beneficial for optimisation performance. In particular, we now consider the case in which the optimisation problem (4.2) is solved but with the trailing edge frequency w_β as an additional variable optimised in the interval $\omega_\beta \in [1, 20]$, simultaneously with ω_α, ω_y. Three initialisations are shown in Figure 4.3, each of which have initial trailing edge frequency $\omega_\beta = 14$. The optimisation trajectories are broadly similar to these presented in Figure 4.2 (a) for fixed ω_β. However, the trajectories are able to pass through the boundary—indicated by dashed lines—of the feasible set for $\omega_\beta = 14$ with no discernible decrease in the smoothness of convergence trajectories. The background contour plot of Figure 4.3 indicates how this is achieved: contours indicate the percentage of values of $1 \leq \omega_\beta \leq 10$ for which a point in $(\omega_\alpha, \omega_y)$-space is feasible. Although the trajectories are now able to traverse boundaries the final converged value is still a function of initial starting point. Figure 4.3 (b) indicates why this is the case: The worst performing trajectory is path (i), which is initialized close to the unfeasible set for $\omega_\beta = 14$. This forces the optimiser to initially decrease ω_β to reduce the cost function, and the optimisation

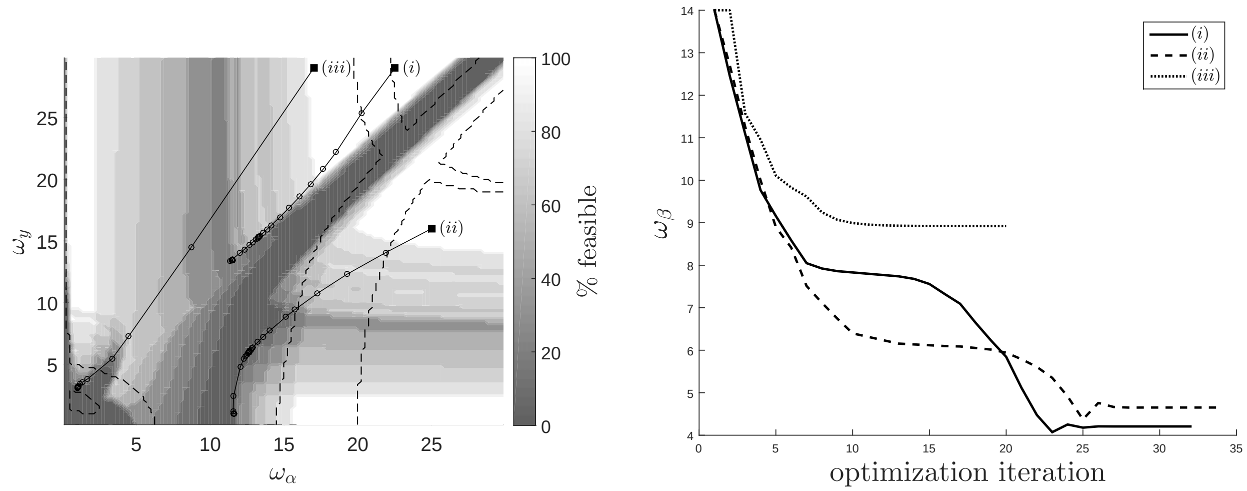

Figure 4.3: (a) Convergence of trajectories through three-dimensional design space and the feasible set corresponding to $\omega_\beta = 14$ (dashed lines). (b) Value of ω_β for the optimisation trajectories identified in (a)

trajectory eventually converges to a local minimum corresponding to $\omega_\beta \approx 4$. In contrast, path (*iii*) avoids this local minimum by maintaining $\omega_\beta \approx 14$ for initial iterations, and only reducing ω_β to optimise the design when ω_y, ω_α are small.

It should be noted that, in this example, we have imposed the simplest possible dynamic constraint of open-loop stability. However, such a constraint does not guarantee good dynamic performance, nor indicates whether a design is amenable to closed-loop control. One characteristic evident from the optimisation trajectories in Figures 4.2(a) and 4.3(a) is that converged designs lie on the boundary of the feasible set, in this case corresponding to marginal stability. Hence, control is required for acceptable performance. Now, if we strengthen the dynamic constraint to incorporate closed-loop performance, yet still expect an optimiser to obtain designs on the boundary of new constraint set, care must be taken to ensure that such design points represent *robust designs*. This is especially pertinent since saturation is included in the studied model.

4.2.1 Constraints for Closed-Loop Performance

To optimise closed-loop performance of a design with parameters X, given by (3.68), a necessary constraint is that the system is closed-loop stable, that is, $A - B_u K$ is stable. For aeroelastic problems it is natural to attempt to form a robust version of this constraint by imposing that the system is stable for a range of free-stream velocities containing the design point V_∞. To this end, a safety margin is imposed such that the flutter speed of a feasible design must be at least a proportion $C_1 > 1$ greater than the designed cruise velocity, that is,

$$V_F(X) \geq C_1 V_\infty. \tag{4.3}$$

It should be noted that although (4.3) is technically a constraint on closed-loop stability under full-state feedback $u = -K\boldsymbol{x}$, the separation principle [132] ensures that the output-feedback $u = -K\hat{\boldsymbol{x}}$ is also stabilising if the pair (C, A) is observable, which is typically the case for the case of two pressure sensors that we consider.

We now consider whether (4.3) is sufficient for good closed-loop performance. To this end, consider the time-domain metric

$$f(X, w, T) = \int_0^T |y(X;t)|^2 + |\alpha(X;t)|^2 \, dt, \tag{4.4}$$

where $y(X;t), \alpha(X,t)$ are the heave and pitch trajectories of the closed-loop output-feedback for a system with design parameters X, simulated from zero-initial conditions and forced by an external disturbance $(w(t))_{t=0}^T$. The use of a time-domain statistic is necessary since the system contains a saturation nonlinearity, whose influence may not necessarily be affected by a linear constraint of the form (4.3). Indeed, Figure 4.4 shows the trajectory of an optimised design vector X satisfying (4.3) with a 25% safety margin ($C_1 = 1.25$), forced by a "$1 - \cos$"

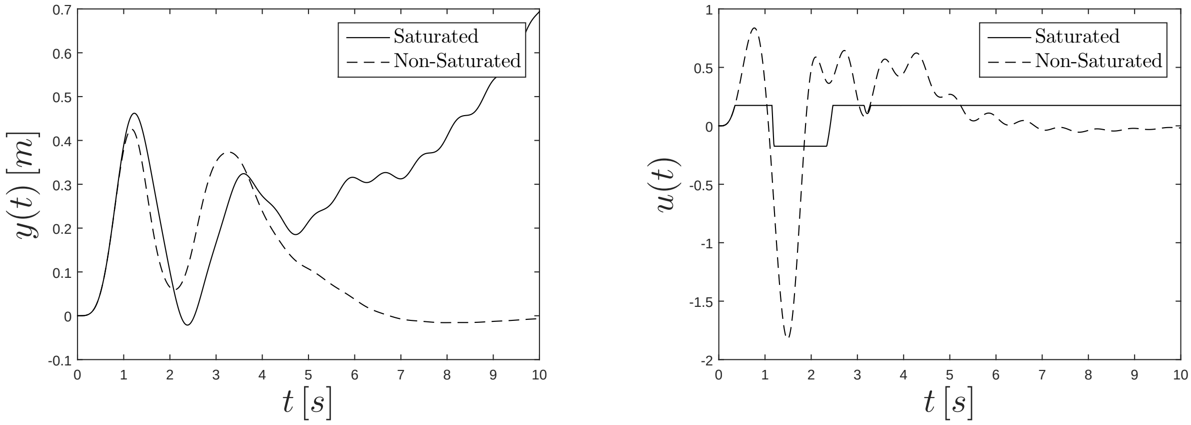

Figure 4.4: Heave response and control input under a "1−cos" disturbance, with and without control saturation.

gust

$$w\left(t\right)=\begin{cases} w_0\left(1-\cos\left(\frac{\pi V_\infty t}{l}\right)\right), & 0\leq t\leq\frac{2l}{V_\infty}, \\ 0, & \text{otherwise}, \end{cases} \tag{4.5}$$

with amplitude $w_0 = 1m$ and length $\ell = 2b$. The choice of a discrete gust, as opposed to a continuous gust, is preferred in this Chapter as it allows for easier investigation of the stability of the systems studied. It can be seen in Figure 4.4(a) that if saturation is not imposed then the control rejects the gust effectively, stabilizing the system within approximately two gust lengths. However, upon imposing control saturation—evident in Figure 4.4(b)—despite the trajectory $y(X, t)$ being initially broadly similar to the unsaturated case, divergence occurs and $f(X, w, t) \to \infty$ as $t \to \infty$. Hence, even a seemingly conservative constraint ensuring linear closed-loop stability at free-stream velocities 25% greater than the design condition is not sufficient to guarantee nonlinear stability of the system. A standard method of avoiding saturation is to tune the closed loop control in order to ensure that the input is bounded as a function of the expected disturbance magnitude. This quantity can be estimated by considering the transfer function T_{uw} from disturbance w to control input u of the output-feedback system. In particular, by considering the coupled state-observer dynamics (3.58), (3.65) and the feedback $u(t) = -K\hat{\boldsymbol{x}}$, it is shown in Appendix A that

$$T_{uw}(s) = \begin{pmatrix} 0 & -K \end{pmatrix} \begin{pmatrix} sI - A & -B_u K \\ LC & sI - (A - LC - B_u K) \end{pmatrix}^{-1} \begin{pmatrix} B_w \\ 0 \end{pmatrix}. \tag{4.6}$$

Since $\|u\|_2 \leq \|T_{uw}\|_\infty \|w\|_2$ and, additionally, a sinusoidal disturbance w with frequency ω is attenuated at the control input u with gain $|T_{uw}(i\omega)|$, it is natural to attempt to constrain the magnitude of the control input by requiring that

$$\|T_{uw}\|_\infty := \sup_\omega |T_{uw}(i\omega)| \leq C_2, \tag{4.7}$$

where C_2 may be chosen appropriately. We note that a more simplistic way of achieving this aim would be to constrain the weight-ratios $Q_y/R, Q_\alpha/R$ in the control-gain cost function (3.62). However, to specify a global bound on the control input $u(t)$ would require ratios which would depend upon the underlying system matrices, making such a condition non-trivially X-dependent, and therefore difficult to specify. Instead, (4.7) represents a concise constraint on the magnitude of the control and, indeed, is an elementary example of mixed H_2/H_∞ control synthesis [133].

The effect of adding the constraint (4.7) is considered by performing an ensemble of optimisations in the nine-dimensional design space X, initialized from 5^3 locations corresponding to a grid of points in $(\omega_y, \omega_\alpha, \omega_\beta)$-space. We test stability of each converged design by considering the time-domain statistic $f(X, w(t), 50)$, where $w(t)$ is, as above, the gust distribution (4.5) with unit amplitude and length $2b$. Sampling over design space in this way will also allow us to test the robustness of the optimiser with respect to the initial starting condition. Figure 4.5 shows, for varying values of the constraint C_2, the percentage of converged designs which satisfy the relatively loose performance objective $f(X, w(t), 50) \leq 100$.

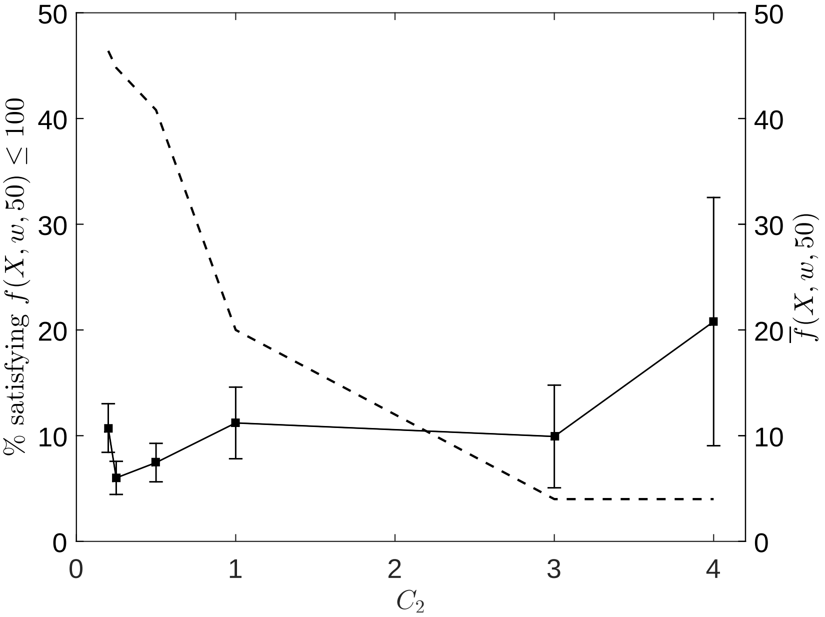

Figure 4.5: The effect of constraining $\|T_{wu}\|_\infty$: percentage of converged designs (dashed line) satisfying the time-domain performance metric; and mean value $\bar{f}$ of metric for converged designs (with standard errors).

For comparison, the converged (albeit unsaturated) trajectory shown in Figure 4.4 satisfies $f(X, w, 50) = 14.0$. It can be seen in Figure 4.5 that imposing a tighter bound through decreasing C_2, limits the magnitude of the control action, reduces the influence of saturation and, hence, results in a higher percentage of converged designs satisfying the performance metric. However, even for very restrictive values of C_2 it is still the case that less that half of the optimisation trajectories do not converge to a design with acceptable closed-loop performance. Furthermore, reducing C_2 more than the plotted data leads to the optimisations failing to converge to designs that satisfy all the constraints.

The low proportion of designs that managed to converge even for small values of C_2 can be explained by Figure 4.6, which demonstrates how the feasible region changes as C_2 is lowered. It can be seen that the connectedness of the feasible region is degraded considerably for $C_2 = 1$ compared to $C_2 = 10$, with Figure 4.6 indicating that the feasible region (for $C_2 = 1$) is partitioned into bands for larger values of ω_α. This reduction in

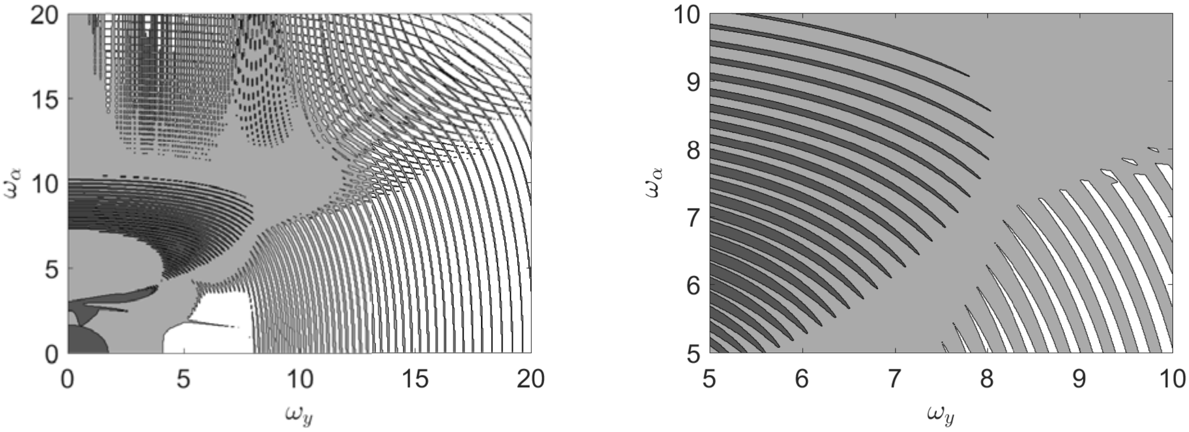

Figure 4.6: Feasible regions of a 2D slice (left) and zoomed area (right). Colour indicates design is feasible for neither (dark grey), one (light grey) or both (white) values of $C_2 = 1, 10$.

connectedness may explain why optimisation with a constraint imposed on T_{uw} fails to give robust performance as the constraint is tightened. The zoomed area in Figure 4.6 uses a higher discretisation to show, with more clarity, the structure of the feasible region. One can see in the lower right of Figure 4.6 (b) a series of bands of feasibility that are not connected for $C_2 = 1$. These bands are connected for $C_2 = 10$. Furthermore, there are bands of infeasibility for $C_2 = 10$—the dark grey bands on the left of 4.6(b)—although the feasible regions between these bands are connected one might expect that such bands will still adversely affect optimisation performance.

These results imply that even the minimal aeroelastic model with a single source of non-linearity, considered here, must be treated in a non-linear optimisation framework. For this reason, instead of attempting to address the nonlinear dynamics (saturation) via additional constraints, we will next seek to indirectly penalize the effects of saturation through the addition of a time-domain component of the cost function. So far, the optimisations have only used a static measure of performance, i.e. the mass. Although the time domain response $f(X)$ has been constrained this was found to lead to designs that did not alleviate the external gust significantly. However, as it will be seen next, if $f(X)$ is included in the cost function instead of a constraint, designs are found with a better dynamic performance, i.e. a lower $f(X)$, with no increase in mass.

We therefore consider the following optimisation problem

$$\begin{aligned} \min_{X} \quad & M_{\text{tot}}(X) + \sum_{i=1}^{N_{gu}} f(X, w_i, T) \\ \text{subject to} \quad & V_F(X) \geq C_1 V_\infty \\ & 2s_2 + 3s_3(1-\xi_h) \geq 0, \\ & |p_1|, |p_2| \leq 1. \end{aligned} \tag{4.8}$$

which includes: a closed-loop flutter constraint with safety margin C_1; imposed monotonicity of the trailing edge, to ensure that physically unreasonable designs are avoided; and the trivial constraint that pressure sensors must lie on the aerofoil itself. The cost function seeks to minimize a trade-off between total mass M_{tot} and dynamic performance under $i = 1, ..., N_{gu}$ external "$1 - \cos$" disturbances $w_i(t)$ given by

$$w_i(t) = \begin{cases} \frac{1}{2} w_0 \left(1 - \cos\left(\frac{2\pi t}{l^i}\right)\right), & 0 \leq t \leq 2l_i, \\ 0, & \text{otherwise}, \end{cases} \tag{4.9}$$

here $w_0 = 1\,\text{m}$, $N_{gu} = 3$, and $l_i = i\,\text{m}$. Note that all results in Section 4.3 will be based on the optimisation problem defined in (4.8).

One can see that the cost function in (4.8) is comprised of two terms: the mass and a measure of dynamic performance which, for brevity, we will denote f_1 and f_2. It is common with cost functions with this structure to introduce weightings, W_1 and W_2, and define the optimisation instead as

$$\min_{X} F(X; W_1, W_2), \tag{4.10}$$

where $F(X, W_1, W_2) := W_1 f_1 + W_2 f_2$. We chose to normalise our cost function so that over a range of optimal solutions we had $W_1 f_1 \approx W_2 f_2$. This gives designs that place equal importance on the mass and dynamics. We found that $W_1 = W_2 = 1$ was a suitable choice for this across the design space. However, if one wanted to obtain "low mass" designs, for example, then one could let $W_1 \gg W_2$. This would cause the optimisation to prioritise reducing mass at the expense of dynamic performance.

4.3 Aeroservoelastic Design Optimisation

4.3.1 Simultaneous and Sequential Optimisation Strategies

Greater benefit is expected to be achieved from using a simultaneous optimisation, compared to a sequential optimisation, on highly coupled aeroservoelastic systems such as the actuated aerofoil considered here. However, even though a sequential approach should be sub-optimal it is possible that a simultaneous optimisation can fail to reach its potential due to complexity in the design space.

It is possible to demonstrate how the level complexity of the model can change the relative effectiveness between a simultaneous and sequential optimisation. This is achieved by comparing optimal designs of the problem, defined by (4.8), at various free-stream velocities V_∞. Increasing the velocity scales the loads on the structure, and therefore also the controls, but also makes flutter more likely. Therefore it is a suitable parameter to explore the robustness of various optimisation architectures.

Using Algorithms 1 and 2 described in Chapter 2, simultaneous and sequential optimisations are compared in Table 4.1 at various free-stream velocities and over a set of random

V_∞ ms^{-1}	$\varepsilon_{\bar{f}}$	ε_{cg}	ε_{func}	ε_{var}	ε_t
2.5	2.7	0.1	160	-3.3	-1.0
3	0.1	-1.5	200	2.4	-20.4
3.5	-5.6	1.5	220	14.5	3.7
4	-8.1	4.7	520	18.6	80.7
4.5	-8.7	6.0	700	36.7	255
5	-8.4	6.2	540	20.6	181

Table 4.1: Relative errors (in percentage) from sequential to simultaneous optimisations.

initial conditions $\{X_i^0\}_{i=1}^N$ with $N = 50$ and $\epsilon = 10^{-8}$. The relative error from the sequential optimisation to the simultaneous optimisation will be used to compare various quantities. For a given quantity θ the relative error is defined as

$$\varepsilon_\theta = \frac{\theta^{Sim} - \theta^{Seq}}{\theta^{Seq}}. \tag{4.11}$$

The quantities to be discussed are the following:

- The optimal function objective over the initial conditions, $\bar{f}(V_\infty) = \min_i f\left(\varphi_\epsilon^{q,*}\left(X_i^0\right)\right).$
- The mean position of the centre of mass over the initial conditions, cg.
- The mean number of function evaluations, $func$.
- The variance of the converged design vectors $X_i^* = \varphi_\epsilon^{q,*}\left(X_i^0\right)$, i.e. $var(V_\infty) = \frac{1}{N}\sum_{i=1}^N \left(X_i^* - \bar{X}^*\right)^2$, where $\bar{X}^* = \frac{1}{N}\sum_i X_i^*$.
- The mean total CPU time, t.

It can be seen in Table 4.1 that for a smaller free-stream velocity the sequential optimisation outperforms the simultaneous optimisation, giving a design with a 2.7% reduction in cost function. This is likely caused by the extra complexity of a simultaneous optimisation, for example, the simultaneous design space may contain extra local minimum that the optimiser

Variable	ω_y^0	ω_α^0	ω_β^0	Q_y^0	Q_α^0	a_2^0	a_3^0	p_1^0	p_2^0
Value	6.275	2.375	3.7	0	0	-0.5	-0.5	-0.5	0.5

cannot avoid. Alternatively, in simultaneous optimisation the design's controller has greater authority to manipulate the performance causing the design space to be relatively flatter and hence the algorithm stopping due to satisfying the design vector tolerance condition rather than finding a minimum. However, as the velocity increases the coupling of the control design to the aerofoil becomes stronger for two reasons: the forces that the trailing edge is able to generate increases with free-stream velocity, hence, at higher velocities the control surface can exert a more significant effect on the dynamics, meaning that integration of its design into the simultaneous optimisation is potentially advantageous. Second, as the free-stream velocity increases, the volume of the feasible set of design space decreases due to the flutter constraint, again implying an increasingly important role of the control design. In any case, for $V_\infty \geq 3.5\,\mathrm{ms}^{-1}$ it is observed that simultaneous optimisation outperforms sequential optimisation by at least 5%. An example of how a simultaneous optimisation can outperform a sequential optimisation at higher velocities can be seen when looking at the paths through design space taken by each method. A set of initial conditions is created such that

$$X_0^{ij} = \left\{\left[\omega_y^i,\, \omega_\alpha^j,\, \omega_\beta^0,\, Q_y^0,\, Q_\alpha^0,\, s_2^0,\, s_3^0,\, p_1^0,\, p_2^0\right]^\top : \omega_y^0 \leq \omega_y^i \leq \omega_y^0 + N\delta \,\text{and}\, \omega_\alpha^0 \leq \omega_\alpha^j \leq \omega_\alpha^0 + N\delta\right\}.$$

This set forms a small two-dimensional box in $(\omega_y,\, \omega_\alpha)$ space in which $\omega_y^i = \omega_y^0 + (i-1)\delta$ and $\omega_\alpha^j = \omega_\alpha^0 + (j-1)\delta$. From these points both a simultaneous and sequential optimisation is run and their path through $(\omega_y,\, \omega_\alpha,\, \omega_\beta)$ space is plotted in Figure 4.7 for $\delta = 0.001$ and $N = 10$. When comparing simultaneous optimisation to sequential optimisation it can be seen in Table 4.1 that at higher velocities the average position of the centre of gravity is further aft, by as much as 6.2% of the chord. In general moving the centre of gravity towards the tail leads to an aerofoil that is more prone to flutter instability. The placement of the

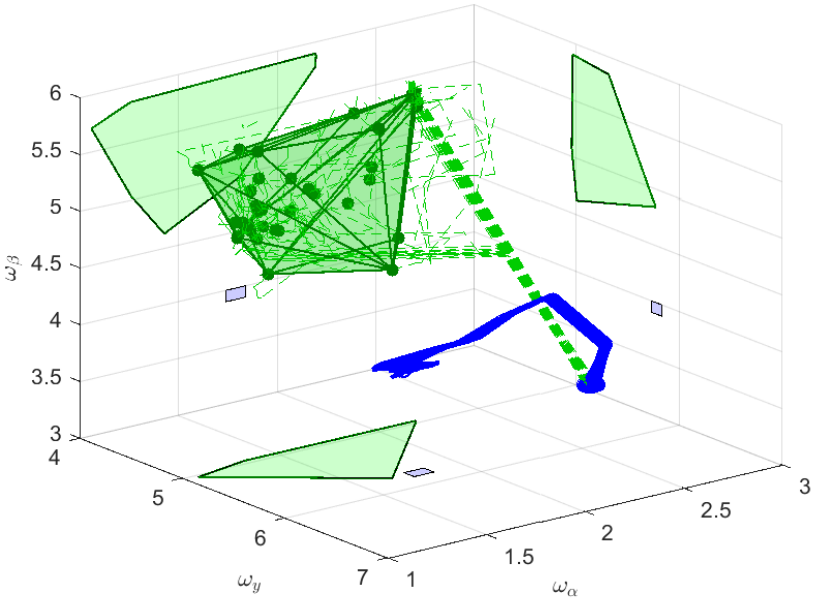

Figure 4.7: Iteration paths from numerous close initial conditions from a sequential method, blue, and a simultaneous method, green. The final design points of the simultaneous method are marked with dark green circles. A convex hull has been plotted around these points along with its projections in the $\omega_y - \omega_\alpha$, $\omega_\alpha - \omega_\beta$ and $\omega_y - \omega_\beta$ planes.

centre of gravity in this model is calculated using the density in (3.60), i.e. the heavier the flap is made relative to the aerofoil the more aft the centre of gravity. Since this is a more unstable location such designs are often open-loop unstable. However, the open-loop instability allows for faster actuation, and a corresponding decrease in the dynamic component of the cost function $f_2(X)$.

Although the simultaneous method is able to find better optimal designs it suffers from greater sensitivity to initial conditions and requires more function evaluations. It must be noted, that although all the sequential designs terminated at points in which MATLAB outputted that a local minimum was found that the simultaneous designs terminated due to satisfying the design vector tolerance condition. This would explain the large convex hull seen in Figure 4.7. On average, over all the velocities in Table 4.1 a single cost-function evaluation took 0.11 seconds — as with all results this was computed on an Intel core i7-4770 CPU. This was consistent over all speeds and only varied significantly when evaluating marginally stable or unstable designs. For example, the average number of function evaluations needed for $V_\infty = 4.5\,ms^{-1}$ was 121.4 and 971.2 for the sequential and simultaneous optimisations, respectively. Hence, the simultaneous optimisations spent approximately 93.5 seconds longer on function evaluations (the average a sequential optimisation took 53.1 seconds). Note that one might expect more proportionality between total CPU time and function evaluations in a higher fidelity model that requires more time per function evaluation. This is due to fixed costs not directly attributed to the cost-function evaluations, for example the time required for Matlab to call `fmincon`, becoming proportionally less significant.

The increase in sensitivity to initial conditions can be seen both in Figure 4.7 and Table 4.1. The percentage change in the variance of the optimal designs is as high as 36.7% and the number of function evaluations increases by a factor of seven. In Sections 4.3.3

and 4.3.4, we will discuss methods that reduce these unwanted consequences of simultaneous optimisation.

4.3.2 Physical interpretation of the optimal results

As previously discussed, the centre of gravity further aft is a more unstable location. These designs are often open-loop unstable, which is the general trend observed in Figure 4.2. However, open-loop instability facilitates more aggressive control action for a given actuation deflection which is desirable, due to the important role that saturation plays in the closed-loop dynamics. In particular, closed-loop time-domain responses corresponding to tail-heavy configurations are observed in Figure 4.8 to have smaller settling times when subjected to the gust

$$w\left(t\right)=\begin{cases}\frac{1}{2}\left(1-\cos\left(\pi bt\right)\right)ms^{-1} & 0\leq t\leq 2\,\mathrm{s},\\ 0 & \text{otherwise.}\end{cases} \tag{4.12}$$

This phenomenon can be isolated from other factors by artificially moving the centre of gravity, by a distance $0.1b$, while keeping the design vector constant. It can seen in Figure 4.8 that small changes in the centre of gravity can affect the time domain response and in fact moving it towards the tail improves the response. The figure shows, in particular, the amplitudes in heave and control input for mass offsets of ±5%.

4.3.3 Parametrisation

As the tolerance condition, ϵ, is decreased the best local minimum found $f\left(X^{*}\right)$—from optimisations initialised from the starting set $\{X_i^0\}_{i=1}^N$, described in Algorithm 1—decreases. This is shown in Figure 4.9. In Chapter 2 a reparameterisation technique was discussed that used Proper Orthogonal Decomposition (POD) to rotate the basis in which the design vector

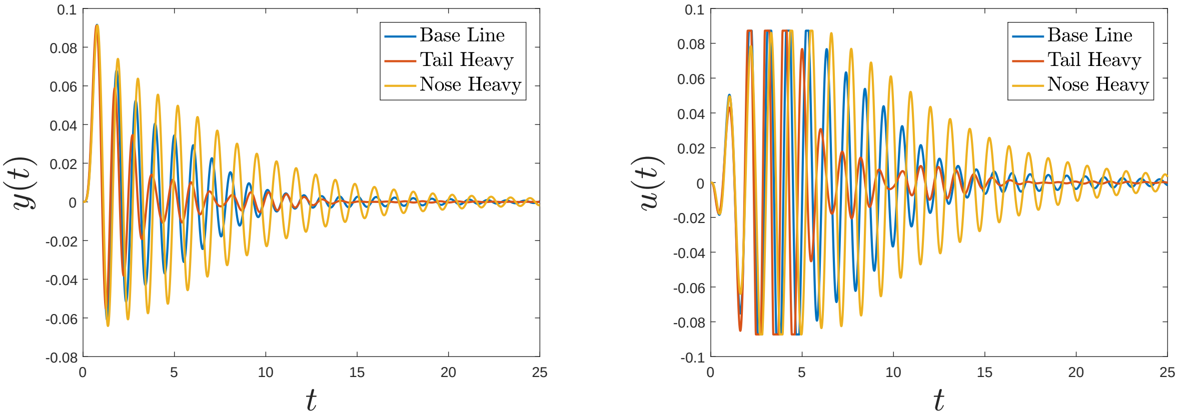

Figure 4.8: Closed-loop responses of aerofoils with the same design vector but varied centre of gravity and $V_\infty = 4.5\, ms^{-1}$. Centre of gravity is displaced a distance equal to 5% of the chord towards the tail in Tail Heavy case and displaced the same distance towards the nose for the Nose Heavy case.

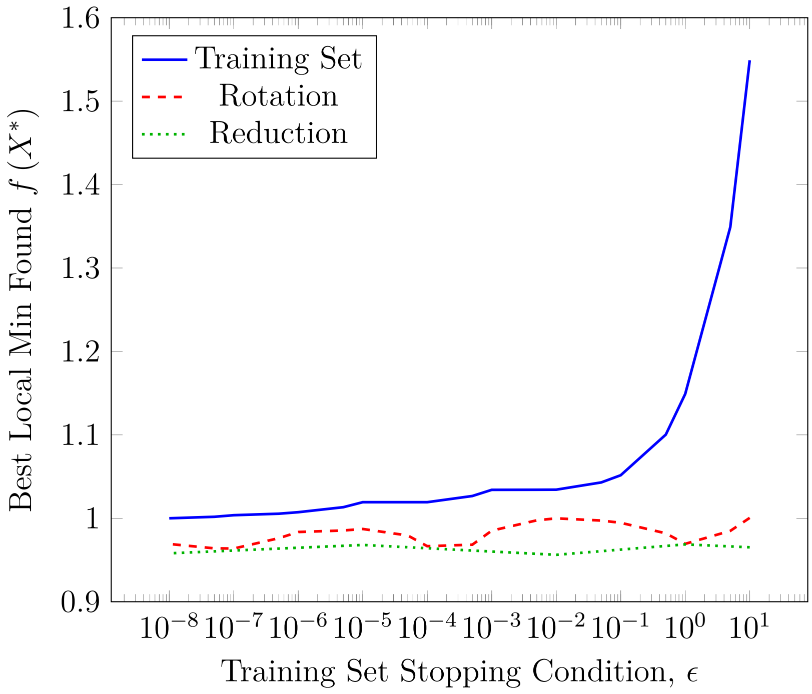

Figure 4.9: The lowest cost function found from each method, normalised by the lowest found by the training set with $\epsilon = 1 \times 10^{-8}$ and shown for a range of values for the training set stopping condition ϵ.

is defined. Figure 4.9 also shows that simply rotating the basis vectors, by use of Algorithm 3, can lead to the optimisation outperforming the best training set local minimum, found at $\epsilon = 1 \times 10^{-8}$, by roughly 5% even for the larger values of ϵ. This rotated optimisation, label POD in Figure 4.9, is shown to be approximately constant over eight orders of magnitude of ϵ and always lies beneath the best local minimum found in the original basis. This result is slightly counter-intuitive, for one, computational effort is invested in the formation of the training set and then the optimiser is able to find a better solution regardless of the fact that both methods are solving the same problem defined in (4.8).

4.3.4 Variable Selection

In Section 4.3.1 it has been shown that the aerofoil model studied here can benefit from a simultaneous optimisation strategy. However, the simultaneous method suffers from increased function evaluations and increased sensitivity to the initial conditions due to the complexity of the design space. For computational efficiency it may be of benefit to temporarily optimise over only a subset of the available decision variables. Thus, we now consider whether removing complexity temporarily can help the optimiser obtain improved local minima. Since the goal is to study automated MDO the process of removing complexity needs to be algorithmic rather than user defined. This can be achieved by using a POD parametrisation as explained in Chapter 2, Algorithm 3. This POD-based reduction strategy requires a choice of the value of the reduction proportion parameter Λ. By defining

$$\Lambda(r) = \left(\sum_{i=1}^{d-r} \lambda_i\right) \Bigg/ \left(\sum_{i=1}^{d} \lambda_i\right), \tag{4.13}$$

the typical behaviour of $\Lambda(r)$, seen across all samples collected, is presented in Figure 4.10. It was found that choosing a value of Λ in the initial and relatively flat section of the $\Lambda(r)$ graph

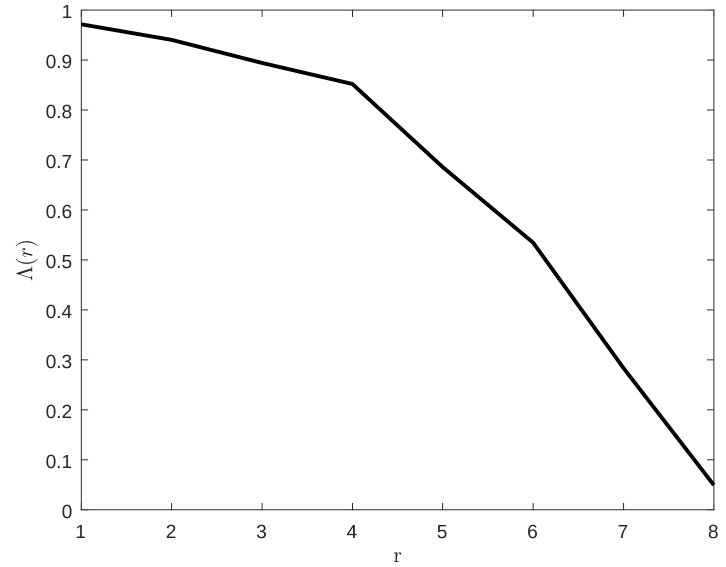

Figure 4.10: Fraction of variance Λ described by a subset of $d - r$ POD basis vectors.

Method	$\varepsilon_{\bar{f}}$	ε_{func}	ε_{var}
Rotation	-2	-28.4	-22.3
Reduction	-4	-37.5	-35.3

Table 4.2: Relative error (as a percentage) from the original basis optimisations to the POD rotated optimisations and original basis optimisations to the reduction method.

(in this case between $1 \leq r \leq 4$) leads to a good balance between final cost function, number of function evaluations and sensitivity to initial conditions. Choosing $\Lambda = 0.85$ successfully placed the reduction method in this flat section for all cases tested. The improvements from using $\Lambda = 0.85$ can be seen in Figure 4.9. As with the rotation strategy plot, the reduction plot is approximately constant and visibly outperforms the original simultaneous optimisations. Further comparisons between the original basis, POD rotation method and reduction method are found in Table 4.2. Both the POD rotation and reduction methods have successfully attenuated some of the undesired consequences that were demonstrated in Figure 4.7 and discussed in Section 4.3.1. While performing slightly better than the standard simultaneous optimisation the investigated strategies have also reduced the number of function evaluations needed and lowered the sensitivity to initial conditions. The percentage difference between

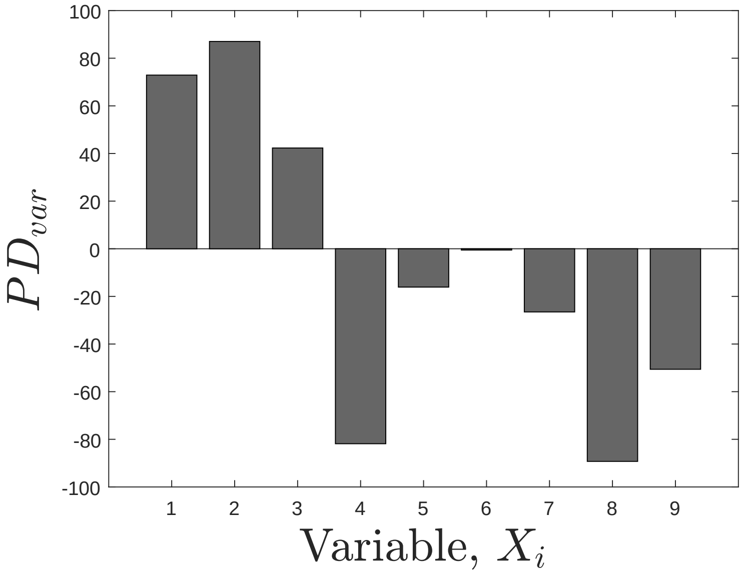

Figure 4.11: Percentage difference between the final designs from the original basis and Reduction method with $X = [\omega_y,\, \omega_\alpha,\, \omega_\beta,\, Q_y,\, Q_\alpha,\, s_2,\, s_3,\, p_1,\, p_2,\,]^\top$

the original basis final designs and the reduction method final designs for each component has been shown in Figure 4.11. Interestingly the variance was reduced in all the components except the structural variables. This could be due to the structural variables being the most dominant variables in the problem. The reduction method is able to identify this and hence varies the other variables less and instead searches the structural space more thoroughly.

4.4 Concluding Remarks

This Chapter started with the validation of the aeroelastic model discussed in Chapter 3. A simple open-loop aeroelastic optimisation was able demonstrated that the complexity of design space, specifically how well the design space was connected, was a factor in the performance of a gradient based optimiser. The effect of including control saturation was investigated in Section 4.2.1. Examples where found that showed that even if our aeroservoelastic system is linearly stable that the nonlinear time-domain response (due to saturation) could diverge. Since computing time-domain responses can be computationally demanding frequency-domain methods were investigated. Although the frequency-domain method did lead to more designs with convergent time-domain responses it was far from guaranteeing convergence, with approximately 50% of designs still having divergent time-domain responses. Furthermore, it was shown that design space connectedness was limiting this method from achieving better results. Thus it was concluded that frequency-domain methods were not a substitute for time-domain response evaluation. Hence, we choose to investigate a cost function that included a metric of the time-domain response.

In Section 4.3.1 it was shown that a simultaneous optimisation strategy, compared to a sequential strategy, was more beneficial at higher free-stream velocities. We argued this is because at higher velocities the control design has more influence over dynamics as the trailing edge flap is able to generate higher forces. While at lower velocities the benefit of simultaneous design is outweighed by the added complexity to the design space. It was also shown that simultaneous design promoted the design of aerofoils that had worse open-loop properties. For example, the centre of gravity was typically further aft in simultaneous designs, compared with sequential designs, a characteristic that in open-loop leads to more unstable responses. However, in closed-loop this meant designs where able to reject gusts quicker, this is analogous to why some fighter jets are open-loop unstable.

Finally using Proper Orthogonal Decomposition to reparametrise or temporarily reduced the number of design variables, a method described in Chapter 2 Algorithm 3, was investigated. Both methods were shown to improve the robustness for simultaneous optimisation strategies, specifically they decreased the sensitivity to initial conditions. Moreover, they achieved this while producing designs with better performance, i.e. designs with a lower cost-function value. These methods show promise in automating reparametrisation and variable reduction, which we have shown lead to an accelerated design optimisation.

Chapter 5

Cantilever Model

The previous chapter used a relatively simple model to exercise the design optimisation of aeroservoelastic systems. With the aim of investigating a more physically realistic and complex model this chapter derives a state-space formulation of an aeroservoelastic cantilever wing model. The model consists of a geometrically-nonlinear, slender-beam described by a one-dimensional reference line that can deform in three-dimensional space; a two-dimensional, potential aerodynamic model defined over the span of the beam and trailing edge flaps that can vary in size and position. As described in Chapter 4 it was infeasible to include design of the size or position of control surfaces in the spatially two dimensional aeroelastic optimisation problem considered there, since it was always advantageous for the previous model to make the control flap larger, i.e. $\xi_h \to -1$. Although we do not include design optimisation of the cantilever model it would allow one to include size or positioning of multiple control flaps as design variables, the optimisation of which is key in the context of HALE aircraft, where control surfaces can be used to replace structural weight and stiffness.

5.1 Structural Model

The structural model consists of a geometrically-exact composite beam described with an intrinsic formulation [56]. An intrinsic formulation uses velocities and strains as primary variables, as opposed to the more common descriptions based on displacements and rotations. A disadvantage of the intrinsic formulation is that one must integrate the velocities or strains to recover displacement and rotations. However, an advantage is that the equations of motion only contain quadratic non-linear couplings which will be of use in Chapter 6 where sensitivities required for iterative optimisation are analytically computed.

Suppose that a straight cantilever wing with no sweep is modeled as a beam of length L with centreline parametrised by a scalar $s \in [0, L]$ and with dynamics expressed in intrinsic co-ordinates

$$\boldsymbol{x}_1(s,t) = \begin{pmatrix} \boldsymbol{v}(s,t) \\ \boldsymbol{\omega}(s,t) \end{pmatrix}, \qquad \boldsymbol{x}_2(s,t) = \begin{pmatrix} \boldsymbol{f}(s,t) \\ \boldsymbol{m}(s,t) \end{pmatrix}, \tag{5.1}$$

where $\boldsymbol{v}(s,t), \boldsymbol{\omega}(s,t)$ are the inertial and angular velocities and $\boldsymbol{f}(s,t), \boldsymbol{m}(s,t)$ are sectional internal forces and moments. For the linearised description of the dynamics considered here, these variables are expressed in a frame $(\boldsymbol{e}_i)_{i=1}^3$ local to the beam. A global frame $(\boldsymbol{e}_x, \boldsymbol{e}_y, \boldsymbol{e}_z)$ is chosen to be the span-wise, chord-wise and normal co-ordinates in the undeformed configuration, respectively. The position $\boldsymbol{r}(s,t)$ and rotation $\boldsymbol{T}(s,t)$ (which provides the transformation from the global to local frame) at each point of the beam are given by

$$\frac{\partial \boldsymbol{r}}{\partial t} = \boldsymbol{T}\boldsymbol{v}, \qquad \frac{\partial \boldsymbol{T}}{\partial t} = \boldsymbol{T}\tilde{\boldsymbol{\omega}}, \tag{5.2}$$

where $\tilde{\cdot}$ is the cross-product operator such that $\tilde{\boldsymbol{v}}\boldsymbol{w} := \boldsymbol{v} \wedge \boldsymbol{w}$. We now assume that the beam is moving with constant velocity in the global stream-wise $\boldsymbol{e}_y$ direction, but is clamped

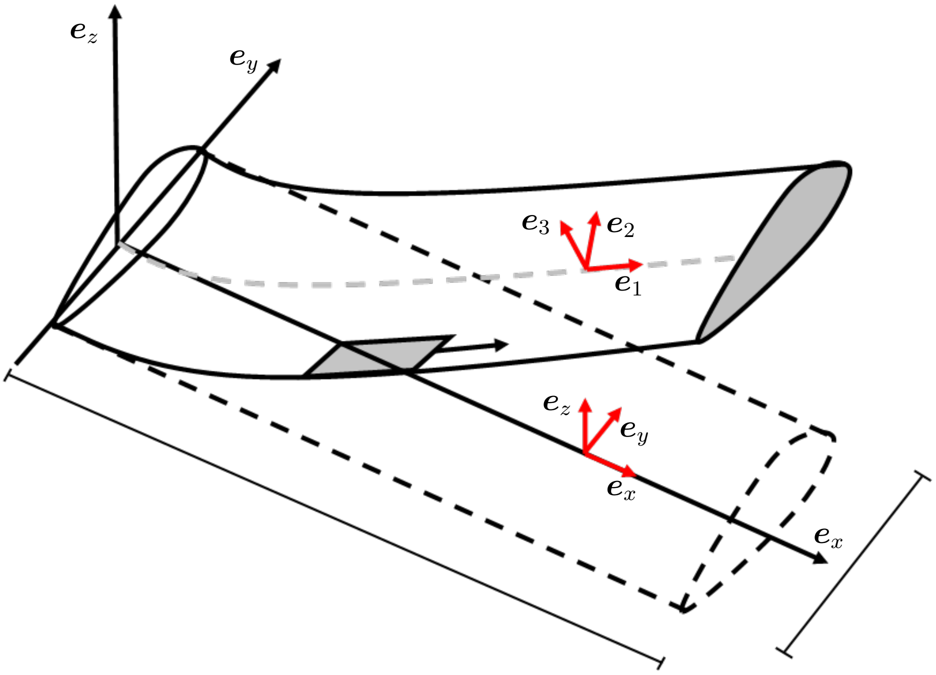
$\boldsymbol{e}_z$
$\boldsymbol{e}_y$
$\boldsymbol{e}_3$
$\boldsymbol{e}_2$
$\boldsymbol{e}_1$
$\boldsymbol{e}_z$
$\boldsymbol{e}_y$
$\boldsymbol{e}_x$
$\boldsymbol{e}_x$

Figure 5.1: Definition of the global frame $[\boldsymbol{e}_x, \boldsymbol{e}_y, \boldsymbol{e}_z]^\top$ and local frame $[\boldsymbol{e}_1, \boldsymbol{e}_2, \boldsymbol{e}_3]^\top$.

at one end to remain in the same unrotated (x, z)-plane, that is, $\boldsymbol{r}(0, t) = -V_\infty t\, \boldsymbol{e}_y$ and $\boldsymbol{T}(0, t) = \boldsymbol{I}_3$. In intrinsic co-ordinates, this condition and the assumption of a free endpoint at $s = L$, corresponds to the boundary conditions

$$\boldsymbol{x}_1(0, t) = V_\infty \begin{pmatrix} \boldsymbol{e}_y \\ \boldsymbol{0} \end{pmatrix}, \qquad \boldsymbol{x}_2(L, t) = \boldsymbol{0}. \tag{5.3}$$

A depiction of the different frames, $\boldsymbol{r}$ and the free-stream velocity can be found in Figure 5.1.

Palacios adapted Hodges' [134] model to show that the linearised dynamics of the beam satisfies the PDE

$$\begin{aligned}\boldsymbol{M}\frac{\partial \boldsymbol{x}_1}{\partial t}-\frac{\partial \boldsymbol{x}_2}{\partial s}-\boldsymbol{E}\boldsymbol{x}_2+\mathcal{L}_1(\boldsymbol{x}_1)\boldsymbol{M}\boldsymbol{x}_1+\mathcal{L}_2(\boldsymbol{x}_2)\boldsymbol{C}\boldsymbol{x}_2&=\boldsymbol{F}(s,t),\\ \boldsymbol{C}\frac{\partial \boldsymbol{x}_2}{\partial t}-\frac{\partial \boldsymbol{x}_1}{\partial s}+\boldsymbol{E}^\top\boldsymbol{x_1}-\mathcal{L}_1(\boldsymbol{x}_1)^\top\boldsymbol{C}\boldsymbol{x}_2&=\boldsymbol{0},\\ \boldsymbol{x}_1(0,t)&=V_\infty\begin{pmatrix}\boldsymbol{e}_y\\ \boldsymbol{0}\end{pmatrix},\\ \boldsymbol{x}_2(L,t)&=\boldsymbol{0},\end{aligned} \tag{5.4}$$

were $\boldsymbol{F}(s,t)$ contains all external forcing terms. Here, assuming an initially undeformed beam, the matrix $\boldsymbol{E}$ is given by

$$\boldsymbol{E}=\begin{pmatrix}\boldsymbol{0} & \boldsymbol{0}\\ \tilde{\boldsymbol{e}}_x & \boldsymbol{0}\end{pmatrix}\in\mathbb{R}^{6\times 6}, \tag{5.5}$$

$\boldsymbol{M}=\boldsymbol{M}(s)\in\mathbb{R}^{6\times 6}$ and $\boldsymbol{C}=\boldsymbol{C}(s)\in\mathbb{R}^{6\times 6}$ are the spatially-dependent mass and compliance matrix, respectively. The operators $\mathcal{L}_1$ and $\mathcal{L}_2$ are defined by

$$\mathcal{L}_1\begin{pmatrix}\boldsymbol{v}\\ \boldsymbol{\omega}\end{pmatrix}:=\begin{pmatrix}\tilde{\boldsymbol{\omega}} & 0\\ \tilde{\boldsymbol{v}} & \tilde{\boldsymbol{\omega}}\end{pmatrix},\qquad \mathcal{L}_2\begin{pmatrix}\boldsymbol{f}\\ \boldsymbol{m}\end{pmatrix}:=\begin{pmatrix}0 & \tilde{\boldsymbol{f}}\\ \tilde{\boldsymbol{f}} & \tilde{\boldsymbol{m}}\end{pmatrix}. \tag{5.6}$$

5.2 Aerodynamic Model

An aerofoil with constant semi-chord b is assumed to exist at each location s of the beam. Furthermore, it is assumed the aerofoils are at zero incidence in the beam axis and that they have constant span-wise aerodynamic properties. It is assumed that aerodynamics contribute to external forcing in (5.4) of the form $\boldsymbol{F}(s,t)=\boldsymbol{F}_{AE}(s,t)+\boldsymbol{F}_{GU}(s,t)+\boldsymbol{F}_{\beta}(s,t)$

where

$$\boldsymbol{F}_{AE}(s,t) = \begin{pmatrix} 0 & F_{a2}(s,t) & F_{a3}(s,t) & M_{a1}(s,t) & 0 & 0 \end{pmatrix}^\top \tag{5.7}$$

is defined in the local frame of reference. The remaining terms $\boldsymbol{F}_{GU}$ and $\boldsymbol{F}_\beta$ are the resulting forcing due to external gusts and trailing edge flap deflections respectively and are to be discussed later in Sections 5.4 and 5.5 of this Chapter. Appealing to classical unsteady aerofoil theory, the forces and moments per unit length in (5.7) can be written, as in [135], in terms of the local velocities $\boldsymbol{x}_1$ via

$$\boldsymbol{F}_{AE} = \rho b \mathcal{A}_1(\boldsymbol{x}_1)\boldsymbol{x}_1 + \rho b \left[V_\infty \mathcal{A}_2 \boldsymbol{x}_1\right] \left[\sum_{j=1}^{n_{in}} 2a_j^{AE} b_j^{AE} \lambda_j\right] \tag{5.8}$$

where ρ is the air density, b is the aerofoil semi-chord, a_j^{AE}, b_j^{AE} are aerodynamic coefficients and $(\lambda_j(s,t))_{j=1}^{n_{in}}$ are additional state-variables describing the unsteady aerodynamics as in the aerofoil model described in Chapter 3, Section 3.1.5. By convention, $\sum_j a_j^{AE} = \frac{1}{2}$. They are influenced, in turn, by the local velocity of the aerofoil according to

$$\dot{\lambda}_j = \boldsymbol{\kappa}_1^\top \boldsymbol{x}_1 - \frac{V_\infty b_j^{AE}}{b}\lambda_j, \qquad j = 1, \dots, n_{in}, \tag{5.9}$$

where $\boldsymbol{\kappa}_1 := \begin{pmatrix} 0 & 0 & -1/b & (1-\xi_{ea}) & 0 & 0 \end{pmatrix}^\top$. Here ξ_{ea} is the parameter determining the distance $\xi_{ea} b$ from the structural axis through which the aerodynamic forces are assumed to act, $\xi_{ea} > 0$ implies aerodynamic forces act fore of the structural axis. Finally, the operator $\mathcal{A}_1 : \mathbb{R}^6 \to \mathbb{R}^{6\times 6}$ and the matrix $\mathcal{A}_2 \in \mathbb{R}^{6\times 6}$ are given by

$$\mathcal{A}_1(\boldsymbol{x}_1) := \begin{pmatrix} 0 & 0 & 0 & 0 & 0 & 0 \\ 0 & -C_{D0}v_2 & \frac{C_{L\alpha}}{2}v_3 - C_{L0}v_2 & -b(1-\xi_{ea})\frac{C_{L\alpha}}{2}v_3 & 0 & 0 \\ 0 & C_{L0}v_2 - \left(\frac{C_{L\alpha}}{2} + C_{D0}\right)v_3 & 0 & b(1-\xi_{ea})\frac{C_{L\alpha}}{2}v_2 & 0 & 0 \\ 0 & b\left((2C_{M0}+\xi_{ea}C_{L0})v_2 - \xi_{ea}\frac{C_{L\alpha}}{2}v_3\right) & 0 & b^2(\xi_{ea}-\xi_{ea}^2-\frac{1}{2})\frac{C_{L\alpha}}{2}v_2 & 0 & 0 \\ 0 & 0 & 0 & 0 & 0 & 0 \\ 0 & 0 & 0 & 0 & 0 & 0 \end{pmatrix} \tag{5.10}$$

and

$$\mathcal{A}_2 = \frac{1}{2} C_{L\alpha} \begin{pmatrix} 0 & 0 & 0 & 0 & 0 & 0 \\ 0 & 0 & -1 & 0 & 0 & 0 \\ 0 & 1 & 0 & 0 & 0 & 0 \\ 0 & \xi_{ea} b & 0 & 0 & 0 & 0 \\ 0 & 0 & 0 & 0 & 0 & 0 \\ 0 & 0 & 0 & 0 & 0 & 0 \end{pmatrix}. \tag{5.11}$$

Ignoring gust and flap inputs, the coupled aeroelastic system is formed by applying the aerodynamic forcing $\boldsymbol{F}_{AE}$ as an input to the structural PDE (5.4) and adding the coupling equation (5.9) to obtain

$$\begin{aligned} \boldsymbol{M}\frac{\partial \boldsymbol{x}_1}{\partial t} - \frac{\partial \boldsymbol{x}_2}{\partial s} - \boldsymbol{E}\boldsymbol{x}_2 + \mathcal{L}_1(\boldsymbol{x}_1)\boldsymbol{M}\boldsymbol{x}_1 + \mathcal{L}_2(\boldsymbol{x}_2)\boldsymbol{C}\boldsymbol{x}_2 &= \rho b \mathcal{A}_1(\boldsymbol{x}_1)\boldsymbol{x}_1 \\ &\quad + \rho b \left[V_\infty \mathcal{A}_2 \boldsymbol{x}_1\right] \left(\boldsymbol{\kappa}_{AE}^\top \boldsymbol{\lambda}\right), \\ \boldsymbol{C}\frac{\partial \boldsymbol{x}_2}{\partial t} - \frac{\partial \boldsymbol{x}_1}{\partial s} + \boldsymbol{E}^\top \boldsymbol{x_1} - \mathcal{L}_1(\boldsymbol{x}_1)^\top \boldsymbol{C}\boldsymbol{x}_2 &= \boldsymbol{0}, \\ \frac{\partial \boldsymbol{\lambda}}{\partial t} + V_\infty \boldsymbol{\epsilon}\boldsymbol{\lambda} &= \left[\boldsymbol{\kappa}_1^\top \boldsymbol{x}_1\right] \boldsymbol{1}, \\ \boldsymbol{x}_1(0,t) &= V_\infty \begin{pmatrix} \boldsymbol{e}_2 \\ \boldsymbol{0} \end{pmatrix}, \\ \boldsymbol{x}_2(L,t) &= \boldsymbol{0}, \end{aligned} \tag{5.12}$$

Here,

$$\boldsymbol{\kappa}_{AE} := (2a_j^{AE} b_j^{AE})_{j=1}^{n_{in}}, \qquad \boldsymbol{\epsilon} = \operatorname{diag}\left((b_j^{AE}/b)_{j=1}^{n_{in}}\right), \qquad \boldsymbol{\lambda} = (\lambda_j)_{j=1}^{n_{in}}, \tag{5.13}$$

and $\boldsymbol{1} \in \mathbb{R}^{n_{in}}$ is a vector of units. Note that the equation for $\boldsymbol{\lambda}$ has to hold for all s, thus when we project the equations onto n_{mo} *mode shapes* in Section 5.6 each mode shape will require its own set of aerodynamic states.

5.3 Linearisation

We choose to linearize the PDE about an unloaded equilibrium point of the PDE corresponding with constant velocity in the e_2 direction. This linearisation does not simply involve removing the quadratic nonlinearities present in the intrinsic formulation. In fact when linearising around the forward flight conditions several linearised terms arise from the quadratic nonlinearities. Note that in Chapter 6 we will solve the PDE to find the nonlinear equilibrium, taking advantage of the relatively simply quadratic nonlinearities the intrinsic formulation offers.

For the forward flight condition we linearise around the following state,

$$\boldsymbol{x}_1^0 = V_\infty \begin{pmatrix} \boldsymbol{e}_2 \\ \boldsymbol{0} \end{pmatrix}, \qquad \boldsymbol{x}_2^0 = \boldsymbol{0}, \qquad \boldsymbol{\lambda}^0 = 0. \tag{5.14}$$

To verify that this indeed defines an equilibrium note that

$$\boldsymbol{\kappa}_1^\top \boldsymbol{x}_1^0 = 0, \qquad E^\top \boldsymbol{x}_1^0 = 0 = \frac{\partial \boldsymbol{x}_1^0}{\partial s}. \tag{5.15}$$

We will assume that $\boldsymbol{M}(s)\boldsymbol{x}_1^0 = \begin{pmatrix} V_\infty m_{22}(s)\boldsymbol{e}_2^\top & 0 \end{pmatrix}^\top$, which is justified in Section 7.1 This implies

$$\mathcal{L}_1(\boldsymbol{x}_1^0)\boldsymbol{M}\boldsymbol{x}_1^0 = V_\infty^2 m_{22}(s) \begin{pmatrix} 0 & 0 \\ \tilde{\boldsymbol{e}}_2 & 0 \end{pmatrix} \begin{pmatrix} \boldsymbol{e}_2 \\ 0 \end{pmatrix} = 0, \qquad 0 \le s \le L. \tag{5.16}$$

Furthermore,

$$\mathcal{A}_1(\boldsymbol{x}_1^0)(\boldsymbol{x}_1^0) = \begin{pmatrix} 0 & -C_{D0} & C_{L0} & b(2C_{M0} + \xi_{ea}C_{L0}) & 0 & 0 \end{pmatrix}^\top \tag{5.17}$$

and for a thin, symmetric cantilever wing we can reasonably assume that the zero-angle-of-attack lift/drag/moment coefficients are zero:

$$C_{L0} = C_{D0} = C_{M0} = 0. \tag{5.18}$$

Now, for any $\boldsymbol{x} \in \mathbb{R}^6$, define a matrices $\mathcal{A}_{\boldsymbol{x}}, \mathcal{L}_{\boldsymbol{x}} \in \mathbb{R}^{6\times 6}$ by

$$\begin{aligned} \mathcal{A}_{\boldsymbol{x}}\boldsymbol{y} &:= \mathcal{A}_1(\boldsymbol{x})\boldsymbol{y} + \mathcal{A}_1(\boldsymbol{y})\boldsymbol{x}, \qquad \boldsymbol{y} \in \mathbb{R}^6, \\ \mathcal{L}_{\boldsymbol{x}}\boldsymbol{y} &:= \mathcal{L}_1(\boldsymbol{x})\boldsymbol{M}\boldsymbol{y} + \mathcal{L}_1(\boldsymbol{y})\boldsymbol{M}\boldsymbol{x}, \qquad \boldsymbol{y} \in \mathbb{R}^6. \end{aligned} \tag{5.19}$$

Using the expressions for the operators $\mathcal{A}_1$, $\mathcal{A}_2$ and $\mathcal{L}_1$ it can be seen that

$$\overline{\mathcal{A}_{\boldsymbol{x}_1^0}} := \frac{\mathcal{A}_{\boldsymbol{x}_1^0}}{V_\infty} = \frac{1}{2}C_{L\alpha} \begin{pmatrix} 0 & 0 & 0 & 0 & 0 & 0 \\ 0 & 0 & 0 & 0 & 0 & 0 \\ 0 & 0 & -1 & b(1-\xi_{ea}) & 0 & 0 \\ 0 & 0 & -\xi_{ea}b & b^2\left(\xi_{ea} - \xi_{ea}^2 - \frac{1}{2}\right) & 0 & 0 \\ 0 & 0 & 0 & 0 & 0 & 0 \\ 0 & 0 & 0 & 0 & 0 & 0 \end{pmatrix}, \tag{5.20}$$

$$\overline{\mathcal{A}_2\boldsymbol{x}_1^0} = \frac{\mathcal{A}_2\boldsymbol{x}_1^0}{V_\infty} = \frac{1}{2}C_{L\alpha} \begin{pmatrix} 0 \\ 0 \\ 1 \\ \xi_{ea}b \\ 0 \\ 0 \end{pmatrix}, \tag{5.21}$$

Furthermore, using that $\mathcal{L}_1(a)b = -\mathcal{L}_2(b)a$

$$\begin{aligned}
\mathcal{L}_{\boldsymbol{x}_1^0}\boldsymbol{x}_1 &= \mathcal{L}_1(\boldsymbol{x}_1^0)\boldsymbol{M}\boldsymbol{x}_1 + \mathcal{L}_1(\boldsymbol{x}_1)\boldsymbol{M}\boldsymbol{x}_1^0 && (5.22)\\
&= \mathcal{L}_1(V_\infty \boldsymbol{e}_2)\boldsymbol{M}\boldsymbol{x}_1 - \mathcal{L}_2(V_\infty m_{22}\boldsymbol{e}_2)\boldsymbol{x}_1 && (5.23)\\
&:= V_\infty \overline{\mathcal{L}_{\boldsymbol{x}_1^0}}\boldsymbol{x}_1, && (5.24)
\end{aligned}$$

where

$$\overline{\mathcal{L}_{\boldsymbol{x}_1^0}} = \begin{pmatrix} 0 & 0 & 0 & 0 & 0 & -m_{22} \\ 0 & 0 & 0 & 0 & 0 & 0 \\ 0 & 0 & 0 & m_{22} & 0 & 0 \\ m_{31} & m_{32} & m_{33} - m_{22} & m_{34} & m_{35} & m_{36} \\ 0 & 0 & 0 & 0 & 0 & 0 \\ -m_{11} + m_{22} & -m_{12} & -m_{13} & -m_{14} & -m_{15} & -m_{16} \end{pmatrix}. \qquad (5.25)$$

We now linearize (5.12) about the equilibrium point $(\boldsymbol{x}_1^0, \boldsymbol{x}_0^2, \boldsymbol{\lambda}^0)$ by letting

$$\hat{\boldsymbol{x}}_1 = \boldsymbol{x}_1 - \boldsymbol{x}_1^0, \qquad \hat{\boldsymbol{x}}_2 = \boldsymbol{x}_2, \qquad \hat{\boldsymbol{\lambda}} = \boldsymbol{\lambda}, \qquad (5.26)$$

and, dropping the hats in the final equation, the PDE describing the evolution of the perturbations becomes

$$\begin{aligned}
\boldsymbol{M}\frac{\partial \boldsymbol{x}_1}{\partial t} - \frac{\partial \boldsymbol{x}_2}{\partial s} - \boldsymbol{E}\boldsymbol{x}_2 + \overline{\mathcal{L}_{\boldsymbol{x}_1^0}}\boldsymbol{x}_1 &= \rho b V_\infty \overline{\mathcal{A}_{\boldsymbol{x}_1^0}}\boldsymbol{x}_1 + \rho b V_\infty^2 \left[\overline{\mathcal{A}_2 \boldsymbol{x}_1^0}\right]\left(\boldsymbol{\kappa}_{AE}^\top \boldsymbol{\lambda}\right),\\
\boldsymbol{C}\frac{\partial \boldsymbol{x}_2}{\partial t} - \frac{\partial \boldsymbol{x}_1}{\partial s} + \boldsymbol{E}^\top \boldsymbol{x}_{\mathbf{1}} - V_\infty \mathcal{L}_1(\boldsymbol{e}_2)^\top \boldsymbol{C}\boldsymbol{x}_2 &= \boldsymbol{0},\\
\frac{\partial \boldsymbol{\lambda}}{\partial t} + V_\infty \boldsymbol{\epsilon}\boldsymbol{\lambda} &= \left[\boldsymbol{\kappa}_1^\top \boldsymbol{x}_1\right]\mathbf{1}, \qquad (5.27)\\
\boldsymbol{x}_1(0,t) &= \boldsymbol{0},\\
\boldsymbol{x}_2(L,t) &= \boldsymbol{0}.
\end{aligned}$$

5.4 Gust Model

We are interested in investigating the gust response of the flexible wing, as we did in Chapter 4. We analyse only the idealized case in which the velocity of a gust $\boldsymbol{v}(s,t)$ has the form

$$\boldsymbol{v}(s,t) = w(t)d(s)\boldsymbol{e}_3(s,t), \qquad 0 \leq s \leq L, \quad t \geq 0, \tag{5.28}$$

that is, the gust is assumed to always act in the (local) direction perpendicular to the aerofoils with a prescribed intensity $w(t)$ and spatial distribution $d(s)$. The influence of the gust is assumed to act in a quasi-steady manner through the aerodynamic forcing terms by replacing

$$\begin{aligned} \mathcal{A}_1(\boldsymbol{x}_1)\boldsymbol{x}_1 &\mapsto \mathcal{A}_1(\boldsymbol{x}_1 - \boldsymbol{v})(\boldsymbol{x}_1 - \boldsymbol{v}), \\ \mathcal{A}_2\boldsymbol{x}_1 &\mapsto \mathcal{A}_2(\boldsymbol{x}_1 - \boldsymbol{v}), \\ \boldsymbol{\kappa}_1^\top \boldsymbol{x}_1 &\mapsto \boldsymbol{\kappa}_1^\top(\boldsymbol{x}_1 - \boldsymbol{v}). \end{aligned} \tag{5.29}$$

Applying this transformation and applying the same linerisation as Section 5.3, with the addition of lineristion around the state $\boldsymbol{v}(s,t) = 0$, results in the following equations

$$\begin{aligned} \boldsymbol{M}\frac{\partial \boldsymbol{x}_1}{\partial t} - \frac{\partial \boldsymbol{x}_2}{\partial s} - \boldsymbol{E}\boldsymbol{x}_2 + \overline{\mathcal{L}_{\boldsymbol{x}_1^0}}\boldsymbol{x}_1 &= \rho b V_\infty \overline{\mathcal{A}_{\boldsymbol{x}_1^0}}\boldsymbol{x}_1 + \rho b V_\infty^2 \left[\overline{\mathcal{A}_2 \boldsymbol{x}_1^0}\right] \left(\boldsymbol{\kappa}_{AE}^\top \boldsymbol{\lambda}\right) \\ &\quad + \rho b V_\infty \overline{\mathcal{A}_{\boldsymbol{x}_1^0}\boldsymbol{v}} w(t), \\ \boldsymbol{C}\frac{\partial \boldsymbol{x}_2}{\partial t} - \frac{\partial \boldsymbol{x}_1}{\partial s} + \boldsymbol{E}^\top \boldsymbol{x}_{\mathbf{1}} - V_\infty \mathcal{L}_1(\boldsymbol{e}_2)^\top \boldsymbol{C}\boldsymbol{x}_{\mathbf{2}} &= \mathbf{0}, \\ \frac{\partial \boldsymbol{\lambda}}{\partial t} + V_\infty \boldsymbol{\epsilon}\boldsymbol{\lambda} &= \left[\boldsymbol{\kappa}_1^\top (\boldsymbol{x}_1 - \boldsymbol{v})\right] \mathbf{1}, \\ \boldsymbol{x}_1(0,t) &= \mathbf{0}, \\ \boldsymbol{x}_2(L,t) &= \mathbf{0}, \end{aligned} \tag{5.30}$$

where

$$\overline{\mathcal{A}_{\boldsymbol{x}_1^0}\boldsymbol{v}}w(t) := \frac{\mathcal{A}_{\boldsymbol{x}_1^0}\boldsymbol{v}}{V_\infty} = \frac{1}{2}C_{L\alpha}\begin{pmatrix} 0 \\ 0 \\ -d(s) \\ -\xi_{ea}b\,d(s) \\ 0 \\ 0 \end{pmatrix} w(t). \tag{5.31}$$

5.5 Flap Input

Suppose finally that there are n_{fl} rigid flaps with deflections $(\beta^l(t))_{l=1}^{n_{fl}}$ on the trailing edge of the wing, their location indicated by the span-wise *flap shape function* $S_\beta^l(s)$. For example, a flap of length r at the tip of the wing would have the following flap shape function,

$$S_\beta^1(s) = \begin{cases} 0 & \text{for } 0 \leq s \leq L-r \\ 1 & \text{for } L-r < s < L \end{cases} \tag{5.32}$$

The modification to the aerodynamic forcing experienced by the structure, is modeled by adding the force $\boldsymbol{F}_\beta = \sum_{l=1}^{n_{fl}} \rho b \mathcal{A}_3(\boldsymbol{x}_1)\boldsymbol{x}_1 S_\beta^l(s)\beta^l(t)$ where

$$\mathcal{A}_3(\boldsymbol{x}_1) := \begin{pmatrix} 0 & 0 & 0 & 0 & 0 & 0 \\ 0 & 0 & -C_{L\beta}v_2 & 0 & 0 & 0 \\ 0 & C_{L\beta}v_2 & 0 & 0 & 0 & 0 \\ 0 & (\xi_{ea}bC_{L\beta} + 2bC_{M\beta})v_2 & 0 & 0 & 0 & 0 \\ 0 & 0 & 0 & 0 & 0 & 0 \\ 0 & 0 & 0 & 0 & 0 & 0 \end{pmatrix}, \tag{5.33}$$

as throughout Section 5.3 $\boldsymbol{F}_\beta$ is to be linearised about $\boldsymbol{x}_1^0$. Note that as with the gust model this is a quasi-steady approximation. The linearisation of $\boldsymbol{F}_\beta$ gives the linearised flap force $\boldsymbol{f}_\beta$,

$$\boldsymbol{f}_F(s,t) \approx \sum_{l=1}^{n_{fl}} \mathcal{A}_3(\boldsymbol{x}_1^0)\boldsymbol{x}_1^0 S_\beta^l(s)\beta^l(t) = \sum_{l=1}^{n_{fl}} \rho b V_\infty^2 \begin{pmatrix} 0 \\ 0 \\ C_{L\beta} \\ \xi_{ea} b C_{L\beta} + 2bC_{M\beta} \\ 0 \\ 0 \end{pmatrix} S_\beta^l(s)\beta^l(t) \tag{5.34}$$

$$=: \sum_{l=1}^{n_{fl}} \rho b V_\infty^2 B_\beta S_\beta^l(s)\beta^l(t). \tag{5.35}$$

As the aerodynamic model is linear, this term is simply added to the right hand side of the first equation in (5.30).

5.6 Galerkin Projection

5.6.1 Linear Normal Modes

The linearised PDE (5.30) has an infinite dimensional solution space. In order to solve in the spatial-domain we use a separation of variables with a finite number of *mode shapes*,

$$\boldsymbol{x}_1 = \sum_{g=1}^{n_{mo}} q_{1g}(t)\boldsymbol{\Phi}_{1g}(s), \qquad \boldsymbol{x}_2 = \sum_{g=1}^{n_{mo}} q_{2g}(t)\boldsymbol{\Phi}_{2g}(s). \tag{5.36}$$

In this work we use linear normal modes $\boldsymbol{\Phi}_{1g}$, $\boldsymbol{\Phi}_{2g}$ of the intrinsic beam equation. Linearising the intrinsic beam equation about the unloaded equilibrium $\boldsymbol{x}_1 = \boldsymbol{x}_2 = 0$ with no external forcing gives,

$$\begin{aligned}\boldsymbol{M}\dot{\boldsymbol{x}}_1 - \boldsymbol{x}_2' - \boldsymbol{E}\boldsymbol{x}_2 &= 0,\\ \boldsymbol{C}\dot{\boldsymbol{x}}_2 - \boldsymbol{x}_1' + \boldsymbol{E}^\top\boldsymbol{x}_1 &= 0.\end{aligned} \tag{5.37}$$

Substituting (5.36) into (5.37) leads to the following generalised eigenvalue problem

$$\begin{pmatrix} 0 & \frac{\partial}{\partial s} + \boldsymbol{E} \\ \frac{\partial}{\partial s} - \boldsymbol{E}^\top & 0 \end{pmatrix} \begin{pmatrix} \boldsymbol{\Phi}_{1g} \\ \boldsymbol{\Phi}_{2g} \end{pmatrix} = \omega_g \begin{pmatrix} \boldsymbol{M} & 0 \\ 0 & -\boldsymbol{C} \end{pmatrix} \begin{pmatrix} \boldsymbol{\Phi}_{1g} \\ \boldsymbol{\Phi}_{2g} \end{pmatrix} \tag{5.38}$$

which is solved with the boundary conditions $\boldsymbol{\Phi}_{1g}(0) = 0$ and $\boldsymbol{\Phi}_{2g}(L) = 0$ for the cantilever problem. Given that $\boldsymbol{M}$ and $\boldsymbol{C}$ are real and symmetric the eigenvalues ω_g will always be real and each positive eigenvalue will have an equal and negative counterpart. Note that no assumptions have been made on $\boldsymbol{M}$ and $\boldsymbol{C}$ which could be fully populated. It can be shown [135] that the linear natural modes can be normalised to satisfy

$$\langle \boldsymbol{\Phi}_{1g}, \boldsymbol{M}\boldsymbol{\Phi}_{1p} \rangle = \delta_{gp} = \langle \boldsymbol{\Phi}_{2g}, \boldsymbol{C}\boldsymbol{\Phi}_{2p} \rangle, \tag{5.39}$$

where $\langle \boldsymbol{f}, \boldsymbol{g} \rangle := \int_0^L \boldsymbol{f}(s) \cdot \boldsymbol{g}(s) ds$ for $\boldsymbol{f}, \boldsymbol{g} : [0, L] \to \mathbb{R}^6$. In this continuous form the number of eigenvalues will be infinite. However, if the equations are discretised the number of eigenvalues will equal the number of degrees of freedom. In this work, the mode shapes will be assigned values at $n_{sp} + 1$ locations given by $s_r = r\frac{L}{n_{sp}}$ for $r = 0, \ldots, n_{sp}$. Values between these *nodes* can be linearly interpolated, thus the integrals are given by

$$\langle \boldsymbol{f}, \boldsymbol{g} \rangle = \frac{L}{n_{sp}} \sum_{r=0}^{n_{sp}} \left[\frac{\boldsymbol{f}(s_r) + \boldsymbol{f}(s_{r+1})}{2} \right] \cdot \left[\frac{\boldsymbol{g}(s_r) + \boldsymbol{g}(s_{r+1})}{2} \right]. \tag{5.40}$$

Note that at each location s_r there are 12 degrees of freedom (6 from $\boldsymbol{x}_1$ and 6 from $\boldsymbol{x}_2$) except at s_0 and $s_{n_{sp}}$ where there are 6 degrees of freedom each due to the boundary conditions

$\boldsymbol{\Phi}_{1g}(0) = 0$ and $\boldsymbol{\Phi}_{2g}(L) = 0$. Hence, the solution to the generalised eigenvalue problem in (5.38) will have $12n_{sp}$ eigenvalues.

5.6.2 Aerodynamic states

As in Chapter 3, in order to describe the aerodynamic model with a finite number of states aerodynamic states $\lambda_j(s,t)$ are needed. Since these aerodynamic states need to be defined for all s we introduce the *decomposed aerodynamic states* q^{AE}_{jg}. The decomposed aerodynamic states are to be substituted for the aerodynamic states $(\lambda_j)_{j=1}^{n_{in}}$ in the modal decomposition as follows

$$\lambda_j(s,t) = \sum_{g=1}^{n_{mo}} [\boldsymbol{\kappa}_1^\top \boldsymbol{\Phi}_{1g}(s)] q^{AE}_{jg}(t), \qquad j = 1, \ldots, n_{in}, \quad g = 1, \ldots, n_{mo}. \tag{5.41}$$

Hence there are now $n_{in} \times n_{mo}$ variables for the aerodynamic states, i.e. each mode has n_{in} aerodynamic states. This decomposition is effective since if we assume the following

$$\dot{q}^{AE}_{jg} = q_{1g} - \frac{V_\infty b^{AE}_j}{b} q^{AE}_{jg} - \langle \boldsymbol{\Phi}_{1g}, \boldsymbol{M}\boldsymbol{v} \rangle, \qquad j = 1, \ldots, n_{in}, \quad g = 1, \ldots, n_{mo}, \tag{5.42}$$

then $\dot{\boldsymbol{\lambda}} + V_\infty \boldsymbol{\epsilon} \lambda = [\boldsymbol{\kappa}_1^\top (\boldsymbol{x}_1 - \boldsymbol{v})]\mathbf{1}$, as required for the evolution of the aerodynamic states $\boldsymbol{\lambda}$ as stated in (5.30). It now remains to describe the temporal evolution and influence of the aerodynamic states $\boldsymbol{\lambda}$, or equivalently q^{AE}_{jg}, in a compact manner. To this end, note that if we define $\dot{\boldsymbol{q}}_{AE} \in \mathbb{R}^{n_{mo} \cdot n_{in} \times 1}$ such that,

$$\boldsymbol{q}_{AE} := \begin{pmatrix} q^{AE}_{11} & \ldots & q^{AE}_{1n_{mo}} & q^{AE}_{21} & \ldots & q^{AE}_{2n_{mo}} & \ldots & q^{AE}_{n_{in}1} & \ldots & q^{AE}_{n_{in}n_{mo}} \end{pmatrix}^\top, \tag{5.43}$$

then from (5.42)

$$\dot{\boldsymbol{q}}_{AE} = \begin{pmatrix} \boldsymbol{I}_{n_{mo}} & 0 & -\frac{V_\infty b_1}{b}\boldsymbol{I}_{n_{mo}} & 0 & \cdots & 0 \\ \boldsymbol{I}_{n_{mo}} & 0 & 0 & -\frac{V_\infty b_2}{b}\boldsymbol{I}_{n_{mo}} & \ddots & \vdots \\ \vdots & \vdots & \vdots & \ddots & \ddots & 0 \\ \boldsymbol{I}_{n_{mo}} & 0 & 0 & \cdots & 0 & -\frac{V_\infty b_{n_{mo}}}{b}\boldsymbol{I}_{n_{mo}} \end{pmatrix} \begin{pmatrix} \boldsymbol{q}_1 \\ \boldsymbol{q}_2 \\ \boldsymbol{q}_{AE} \end{pmatrix} + \boldsymbol{B}_w^1 w(t), \quad (5.44)$$

where

$$\boldsymbol{B}_w^1 := -\begin{pmatrix} \langle \boldsymbol{\Phi}_{11}, \boldsymbol{M}[0,\,0,\,1,\,0,\,0,\,0]^\top \rangle \\ \vdots \\ \langle \boldsymbol{\Phi}_{1n_{mo}}, \boldsymbol{M}[0,\,0,\,1,\,0,\,0,\,0]^\top \rangle \\ \langle \boldsymbol{\Phi}_{11}, \boldsymbol{M}[0,\,0,\,1,\,0,\,0,\,0]^\top \rangle \\ \vdots \end{pmatrix} \in \mathbb{R}^{n_{in}.n_{mo}} \quad (5.45)$$

Letting $\mathbf{1} \in \mathbb{R}^{n_{in}}$ be a vectors of units, this can be written

$$\dot{\boldsymbol{q}}_{AE} = \begin{pmatrix} \mathbf{1} \otimes \boldsymbol{I}_{n_{mo}} & 0 & -V_\infty(\boldsymbol{\epsilon} \otimes \boldsymbol{I}_{n_{mo}}) \end{pmatrix} \begin{pmatrix} \boldsymbol{q}_1 \\ \boldsymbol{q}_2 \\ \boldsymbol{q}_{AE} \end{pmatrix} + \boldsymbol{B}_w^1 w(t). \quad (5.46)$$

where $\boldsymbol{\epsilon}$ is defined in 5.2 and $\otimes$ denotes the Kronecker matrix product [136].

5.6.3 State-Space Formulation

We now substitute the expansions (5.36) into the PDE (5.30). Taking the inner product of the first line of the resulting equations with $\boldsymbol{\Phi}_{1g}$, the inner product of the second equation with $\boldsymbol{\Phi}_{2g}$ and using the orthogonality relations (5.39) we have

$$\begin{aligned}
\dot{q}_{1p} = {} & \sum_{g=1}^{n_{mo}} q_{2g}\langle \boldsymbol{\Phi}_{1p}, \boldsymbol{\Phi}_{2g}' + \boldsymbol{E}\boldsymbol{\Phi}_{2g}\rangle - V_\infty \sum_{g=1}^{n_{mo}} q_{1g}\langle \boldsymbol{\Phi}_{1p}, \overline{\mathcal{L}_{\boldsymbol{x}_1^0}}\boldsymbol{\Phi}_{1g}\rangle \\
& + \rho b V_\infty \sum_{g=1}^{n_{mo}} q_{1g}\langle \boldsymbol{\Phi}_{1p}, \overline{\mathcal{A}_{\boldsymbol{x}_1^0}}\boldsymbol{\Phi}_{1g}\rangle + \rho b V_\infty^2 \langle \boldsymbol{\Phi}_{1p}, \overline{\mathcal{A}_2 \boldsymbol{x}_1^0}\rangle \left(\boldsymbol{\kappa}_{AE}^\top \boldsymbol{\lambda}\right) \\
& - \rho b V_\infty \left\langle \boldsymbol{\Phi}_{1p}, \overline{\mathcal{A}_{x_1^0}\boldsymbol{v}}\right\rangle w(t) + \rho b V_\infty^2 \sum_{l=1}^{n_{fl}} \langle \boldsymbol{\Phi}_{1p}, B_\beta S_\beta^l(s)\rangle \beta^l(t), \\
\dot{q}_{2p} = {} & \sum_{g=1}^{n_{mo}} q_{1g}\langle \boldsymbol{\Phi}_{2p}, \boldsymbol{\Phi}_{1g}' - \boldsymbol{E}^\top\boldsymbol{\Phi}_{1g}\rangle + V_\infty \sum_{g=1}^{n_{mo}} q_{2g}\langle \boldsymbol{\Phi}_{2p}, \mathcal{L}_1(\boldsymbol{e}_2)^\top \boldsymbol{C}\boldsymbol{\Phi}_{2g}\rangle,
\end{aligned} \tag{5.47}$$

for each $p = 1, \dots, n_{mo}$.

Now, integration by parts and cantilever boundary conditions, i.e. $\boldsymbol{x}_1(0,t)\boldsymbol{x}_2(0,t) = \boldsymbol{x}_1(L,t)\boldsymbol{x}_2(L,t) = 0$, can be used to show that for each g, p, if $w_{gp} := \langle \boldsymbol{\Phi}_{1p}, \boldsymbol{\Phi}_{2g}' + \boldsymbol{E}\boldsymbol{\Phi}_{2g}\rangle$, then

$$\langle \boldsymbol{\Phi}_{2p}, \boldsymbol{\Phi}_{1g}' - \boldsymbol{E}^\top\boldsymbol{\Phi}_{1g}\rangle = -\langle \boldsymbol{\Phi}_{1p}, \boldsymbol{\Phi}_{2g}' + \boldsymbol{E}\boldsymbol{\Phi}_{2g}\rangle = -w_{gp}. \tag{5.48}$$

Note that when the linear normal modes are used $w_{gp} = \omega_g \delta_{gp}$. For terms arising from linearisation of the terms nonlinear in $\boldsymbol{x}_1, \boldsymbol{x}_2$, define

$$s_{gp} := -\langle \boldsymbol{\Phi}_{1g}, \overline{\mathcal{L}_{\boldsymbol{x}_1^0}}\boldsymbol{\Phi}_{1p}\rangle \tag{5.49}$$

$$t_{gp} := \langle \boldsymbol{\Phi}_{2g}, \mathcal{L}_1(\boldsymbol{e}_2)^\top \boldsymbol{C}\boldsymbol{\Phi}_{2p}\rangle. \tag{5.50}$$

Next, recalling the expression for $\overline{\mathcal{A}_{\boldsymbol{x}_1^0}}$, let

$$\gamma_{gp} := \langle \boldsymbol{\Phi}_{1g}, \overline{\mathcal{A}_{\boldsymbol{x}_1^0}}\boldsymbol{\Phi}_{1p}\rangle \tag{5.51}$$

and define matrices

$$\boldsymbol{W} = \mathrm{diag}(\omega_g) \in \mathbb{R}^{n_{mo} \times n_{mo}}, \quad \boldsymbol{\Gamma} = (\gamma_{gp}) \in \mathbb{R}^{n_{mo} \times n_{mo}}, \tag{5.52}$$

$$\boldsymbol{S} = (s_{gp}) \in \mathbb{R}^{n_{mo} \times n_{mo}}, \quad \boldsymbol{T} = (t_{gp}) \in \mathbb{R}^{n_{mo} \times n_{mo}}, \tag{5.53}$$

upon which the structural equations can be written as

$$\begin{pmatrix} \dot{\boldsymbol{q}}_1 \\ \dot{\boldsymbol{q}}_2 \end{pmatrix} = \begin{pmatrix} V_\infty(\rho b \boldsymbol{\Gamma} + \boldsymbol{S}) & \boldsymbol{W} \\ -\boldsymbol{W}^\top & V_\infty \boldsymbol{T} \end{pmatrix} \begin{pmatrix} \boldsymbol{q}_1 \\ \boldsymbol{q}_2 \end{pmatrix} + \begin{pmatrix} (\langle \boldsymbol{\Phi}_{1g}, \boldsymbol{R}(s,t) \rangle)_{g=1}^{n_{mo}} \\ 0 \end{pmatrix}, \tag{5.54}$$

with the forcing term

$$\boldsymbol{R}(s,t) = \rho b V_\infty \left(V_\infty \left[\overline{\mathcal{A}_2 \boldsymbol{x}_1^0} \right] \left(\boldsymbol{\kappa}_{AE}^\top \boldsymbol{\lambda} \right) - \overline{\mathcal{A}_{\boldsymbol{x}_1^0} \boldsymbol{v}} + \sum_{l=1}^{n_{fl}} V_\infty B_\beta S_\beta^l(s) \beta^l(t) \right). \tag{5.55}$$

The states $\boldsymbol{q}_1$ and $\boldsymbol{q}_2$ in (5.54) need to be solved together with (5.46). We will now consider each term in (5.55) in order to finish writing the equations of motion concisely. First, let $\boldsymbol{\kappa}_2 := \overline{\mathcal{A}_2 \boldsymbol{x}_1^0} = \frac{1}{2} C_{L\alpha} \begin{pmatrix} 0 & 0 & 1 & \xi_{ea} b & 0 & 0 \end{pmatrix}^\top$, we have that

$$\begin{aligned} \rho b V_\infty^2 \langle \boldsymbol{\Phi}_{1g}, \overline{\mathcal{A}_2 \boldsymbol{x}_1^0} \rangle \left(\boldsymbol{\kappa}_{AE}^\top \boldsymbol{\lambda} \right) &= \rho b V_\infty^2 \sum_{j=1}^{n_{in}} 2 a_j^{AE} b_j^{AE} \langle \boldsymbol{\Phi}_{1g}(s), \boldsymbol{\kappa}_2 \lambda_j(s) \rangle \\ &= \rho b V_\infty^2 \sum_{p=1}^{n_{mo}} \sum_{j=1}^{n_{in}} 2 a_j^{AE} b_j^{AE} q_{jp}^{AE} \langle \boldsymbol{\Phi}_{1g}(s), \boldsymbol{\kappa}_2 \boldsymbol{\kappa}_1^\top \boldsymbol{\Phi}_{1p}(s) \rangle \\ &= \rho b V_\infty^2 \sum_{j=1}^{n_{in}} \left[2 a_j^{AE} b_j^{AE} \sum_{p=1}^{n_{mo}} h_{gp} q_{jp}^{AE} \right], \qquad g = 1, \ldots, n_{mo}, \end{aligned} \tag{5.56}$$

where $h_{gp} := \langle \boldsymbol{\Phi}_{1g}, \boldsymbol{\kappa}_2 \boldsymbol{\kappa}_1^\top \boldsymbol{\Phi}_{1p} \rangle$. Letting

$$\boldsymbol{H} := (h_{gp}) \in \mathbb{R}^{n_{mo} \times n_{mo}} \tag{5.57}$$

we can therefore write the first term in (5.55) as

$$\begin{aligned}\left(\rho b V_\infty^2 \langle \boldsymbol{\Phi}_{1g}, \overline{\mathcal{A}_2 \boldsymbol{x}_1^0}\rangle \left(\boldsymbol{\kappa}_{AE}^\top \boldsymbol{\lambda}\right)\right)_{g=1}^{n_{mo}} &= \rho b V_\infty^2 \begin{pmatrix} 2a_1 b_1 \boldsymbol{H} & 2a_2 b_2 \boldsymbol{H} & \cdots & 2a_{n_{in}} b_{n_{in}} \boldsymbol{H} \end{pmatrix} \boldsymbol{q}_{AE} \\ &= \rho b V_\infty^2 (\boldsymbol{\kappa}_{AE}^\top \otimes \boldsymbol{H}) \boldsymbol{q}_{AE}\end{aligned} \tag{5.58}$$

For the second term, pertaining to the vertical gust input, we define $b_g^W := -\rho b \left\langle \boldsymbol{\Phi}_{1g}, \overline{\mathcal{A}_{x_1^0} \boldsymbol{v}} \right\rangle$ we can write

$$-\rho b V_\infty \left\langle \boldsymbol{\Phi}_{1g}, \overline{\mathcal{A}_{x_1^0} \boldsymbol{v}} \right\rangle w(t) = \left(b_g^W (V_\infty) w(t)\right)_{g=1}^{n_{mo}}, \tag{5.59}$$

$$= \boldsymbol{B}_W^2 (V_\infty) w(t), \tag{5.60}$$

where

$$\boldsymbol{B}_W^2 := \left(b_g^W\right)_{g=1}^{n_{mo}} \in \mathbb{R}^{n_{mo}}. \tag{5.61}$$

Now define $\boldsymbol{B}_W := [\boldsymbol{B}_W^1,\, \boldsymbol{0},\, \boldsymbol{B}_W^2]^\top \in \mathbb{R}^n$, where $n = 2n_{mo} + n_{mo}.n_{in}$. The final term, relating to the flap inputs, we define $b_{gl}^\beta := \rho b \langle \boldsymbol{\Phi}_{1g}, B_\beta S_\beta^l(s)\rangle$ so we can write

$$\rho b V_\infty^2 \sum_{l=1}^{n_{fl}} \langle \boldsymbol{\Phi}_{1g}, B_\beta S_\beta^l(s)\rangle \beta^l(t) = \left(\left(V_\infty^2 b_{gl}^\beta \beta^l(t)\right)_{g=1}^{n_{mo}}\right)_{l=1}^{n_{fl}}, \tag{5.62}$$

$$= V_\infty^2 \boldsymbol{B}_\beta \boldsymbol{\beta}(t), \tag{5.63}$$

where

$$\boldsymbol{B}_\beta := \left(b_{gl}^\beta\right) \in \mathbb{R}^{n_{mo} \times n_{fl}} \qquad \text{and} \qquad \boldsymbol{\beta}(t) := \left(\beta^l(t)\right)_{l=1}^{n_{fl}} \in \mathbb{R}^{n_{fl}}. \tag{5.64}$$

Finally, the linearised aeroservoelastic equations of motion can be written in canonical state-space form,

$$\dot{\boldsymbol{q}}(t) = \begin{pmatrix} V_\infty(\rho b\boldsymbol{\Gamma} + \boldsymbol{S}) & \boldsymbol{W} & \rho b V_\infty^2(\boldsymbol{\kappa}_{AE}^\top \otimes \boldsymbol{H}) \\ -\boldsymbol{W}^\top & V_\infty \boldsymbol{T} & 0 \\ \boldsymbol{1} \otimes \boldsymbol{I}_{n_{mo}} & 0 & -V_\infty(\boldsymbol{\epsilon} \otimes \boldsymbol{I}_{n_{mo}}) \end{pmatrix} \boldsymbol{q}(t) + \boldsymbol{B}_W(V_\infty)w(t) + V_\infty^2 \boldsymbol{B}_\beta \boldsymbol{\beta}(t), \quad (5.65)$$

$$:= A\left(V_\infty\right)\boldsymbol{q}(t) + \boldsymbol{B}_W(V_\infty)w(t) + V_\infty^2 \boldsymbol{B}_\beta \boldsymbol{\beta}(t) \quad (5.66)$$

with $A(V_\infty) \in \mathbb{R}^{n \times n}$, $\boldsymbol{1} \in \mathbb{R}^{n_{in}}$ and

$$\boldsymbol{q} = \left(\boldsymbol{q}_1, \, \boldsymbol{q}_2, \, \boldsymbol{q}_{AE}\right)^\top, \quad (5.67)$$

$$\boldsymbol{W} = (w_{gp}) \in \mathbb{R}^{n_{mo} \times n_{mo}}, \qquad w_{gp} = \langle \boldsymbol{\Phi}_{1g}, \boldsymbol{\Phi}_{2p}' + \boldsymbol{E}\boldsymbol{\Phi}_{2p} \rangle, \quad (5.68)$$

$$\boldsymbol{\Gamma} = (\gamma_{gp}) \in \mathbb{R}^{n_{mo} \times n_{mo}}, \qquad \gamma_{gp} = \langle \boldsymbol{\Phi}_{1g}, \mathcal{A}_{\boldsymbol{x}_1^0} \boldsymbol{\Phi}_{1p} \rangle, \quad (5.69)$$

$$\boldsymbol{H} = (h_{gp}) \in \mathbb{R}^{n_{mo} \times n_{mo}}, \qquad h_{gp} = \langle \boldsymbol{\Phi}_{1g}, \boldsymbol{\kappa}_2 \boldsymbol{\kappa}_1^\top \boldsymbol{\Phi}_{1p} \rangle, \quad (5.70)$$

$$\boldsymbol{S} = (s_{gp}) \in \mathbb{R}^{n_{mo} \times n_{mo}}, \qquad s_{gp} = -\langle \boldsymbol{\Phi}_{1g}, \mathcal{L}_{\boldsymbol{x}_1^0} \boldsymbol{\Phi}_{1p} \rangle, \quad (5.71)$$

$$\boldsymbol{T} = (t_{gp}) \in \mathbb{R}^{n_{mo} \times n_{mo}}, \qquad t_{gp} = \langle \boldsymbol{\Phi}_{2g}, \mathcal{L}_1(\boldsymbol{e}_2)^\top \boldsymbol{C} \boldsymbol{\Phi}_{2p} \rangle, \quad (5.72)$$

5.7 Concluding Remarks

In this Chapter we have introduced a cantilever wing model consisting of an intrinsic beam model and two-dimensional aerodynamics, with gust and trailing edge deflection inputs summarised in the PDE (5.4). We linearised this model and projected onto a finite number number of modes, this allowed the PDE to be approximated in the state space formulation in (5.66). This model will be verified in Chapter 7. An advantage of this model, compared to the previous model described in Chapter 3 and 4, is it allows the aeroelastic effects of multiple control surfaces to be predicted.

Chapter 6

Adjoint-based Optimisation

This chapter explores methods that can accelerate the gradient based design optimisation investigated in this work. In Chapter 4 the “black-box” Matlab function `fmincon` for solving the aeroservoelastic design optimisation problems. This uses numerical methods to approximate gradients by finite differences. For example, to approximate the gradient of the cost-function—`fmincon` needs to approximate this at each iteration—at least two cost-function evaluations are needed per design variable for each gradient approximation. Instead, if the gradients are known analytically instead of two function evaluations per variable, needed by approximate methods, only one evaluation of the gradient is required per iteration. To this end, this Chapter presents methods that do not require “black-box” functions and, furthermore, uses analytic values for the gradients, which saves computational time, improves accuracy and numerical robustness. The fact that the model described in Chapter 5, only contains quadratic non-linearities, due to the use of the intrinsic formulation, means the product-rule only needs to be used once per term, hence, easing the analytic evaluation of the derivatives.

6.1 Derivatives

In this Section, with a view to implementing gradient-based optimization techniques, we develop expressions for the derivatives of terms appearing in the governing PDEs, which were written as

$$\begin{gathered} \boldsymbol{M}\frac{\partial \boldsymbol{x}_1}{\partial t} - \frac{\partial \boldsymbol{x}_2}{\partial s} - \boldsymbol{E}\boldsymbol{x}_2 + \mathcal{L}_1(\boldsymbol{x}_1)\boldsymbol{M}\boldsymbol{x}_1 + \mathcal{L}_2(\boldsymbol{x}_2)\boldsymbol{C}\boldsymbol{x}_2 = \boldsymbol{F}(s,t), \\ \boldsymbol{C}\frac{\partial \boldsymbol{x}_2}{\partial t} - \frac{\partial \boldsymbol{x}_1}{\partial s} + \boldsymbol{E}^\top \boldsymbol{x_1} - \mathcal{L}_1(\boldsymbol{x}_1)^\top \boldsymbol{C}\boldsymbol{x}_2 = \boldsymbol{0}, \end{gathered} \tag{6.1}$$

where

$$\mathcal{L}_1\begin{pmatrix} \boldsymbol{v} \\ \boldsymbol{\omega} \end{pmatrix} := \begin{pmatrix} \tilde{\boldsymbol{\omega}} & 0 \\ \tilde{\boldsymbol{v}} & \tilde{\boldsymbol{\omega}} \end{pmatrix}, \qquad \mathcal{L}_2\begin{pmatrix} \boldsymbol{f} \\ \boldsymbol{m} \end{pmatrix} := \begin{pmatrix} 0 & \tilde{\boldsymbol{f}} \\ \tilde{\boldsymbol{f}} & \tilde{\boldsymbol{m}} \end{pmatrix}. \tag{6.2}$$

By convention, if $\boldsymbol{G} : \mathbb{R}^n \to \mathbb{R}^m$ is a vector-valued function given by

$$\boldsymbol{G}(\boldsymbol{x}) = \begin{pmatrix} g_1(\boldsymbol{x}) \\ g_2(\boldsymbol{x}) \\ \vdots \\ g_m(\boldsymbol{x}) \end{pmatrix}$$

and the Jacobian matrix $\frac{\partial \boldsymbol{G}}{\partial \boldsymbol{x}} \in \mathbb{R}^{n\times m}$ is defined by

$$\left[\frac{\partial \boldsymbol{G}}{\partial \boldsymbol{x}}\right]_{ij} := \frac{\partial g_i}{\partial x_j}, \qquad i = 1,\dots,m,\ j = 1,\dots,n.$$

The following lemma contains results for differentiating matrix and vector products, whose proofs we include for completeness.

Lemma 6.1.1. *Suppose that* $x, y \in \mathbb{R}^3$ *and that* $\boldsymbol{A} \in \mathbb{R}^{3\times 3}$. *Then* *(i)* $\frac{\partial}{\partial \boldsymbol{x}}(\boldsymbol{A}\boldsymbol{x}) = \boldsymbol{A}$;

(ii) $\frac{\partial}{\partial \boldsymbol{x}}(\boldsymbol{x} \wedge \boldsymbol{y}) = -\tilde{\boldsymbol{y}}$;

(iii) $\frac{\partial}{\partial \boldsymbol{x}}(\boldsymbol{y} \wedge \boldsymbol{x}) = \tilde{\boldsymbol{y}}$;

(iv) $\frac{\partial}{\partial \boldsymbol{x}}(\boldsymbol{x} \wedge \boldsymbol{A}\boldsymbol{y}) = -\widetilde{\boldsymbol{A}\boldsymbol{y}}$.

(v) $\frac{\partial}{\partial \boldsymbol{x}}(\boldsymbol{x} \wedge \boldsymbol{A}\boldsymbol{x}) = \tilde{\boldsymbol{x}}\boldsymbol{A} - \widetilde{\boldsymbol{A}\boldsymbol{x}}$.

Proof. (i) Since $(\boldsymbol{A}\boldsymbol{x})_i = \sum_j a_{ij}x_j$, it follows immediately that $\frac{\partial}{\partial \boldsymbol{x}}(\boldsymbol{A}\boldsymbol{x}) = \boldsymbol{A}$.

(ii) Follows from (i) upon writing $\boldsymbol{x} \wedge \boldsymbol{y} = -\boldsymbol{y} \wedge \boldsymbol{x} = -\tilde{\boldsymbol{y}}\boldsymbol{x}$ and (iii) is a trivial corollary.

(iv) Follows from (i) since $\boldsymbol{x} \wedge \boldsymbol{A}\boldsymbol{y} = -[\boldsymbol{A}\boldsymbol{y}] \wedge \boldsymbol{x} = -\widetilde{\boldsymbol{A}\boldsymbol{y}}\boldsymbol{x}$.

(v) Noting that $\boldsymbol{x} \wedge \boldsymbol{A}\boldsymbol{x} = \tilde{\boldsymbol{x}}\boldsymbol{A}\boldsymbol{x}$, the result follows from (i), (iv) and the product rule for differentiation. □

It is now possible to calculate derivatives of expressions involving the operators $\mathcal{L}_1, \mathcal{L}_2$.

Lemma 6.1.2. *Suppose that* $\boldsymbol{x} \in \mathbb{R}^6$ *and* $\boldsymbol{A} \in \mathbb{R}^{6\times 6}$. *Then*

(i) $\frac{\partial}{\partial \boldsymbol{x}}(\mathcal{L}_1(\boldsymbol{x})\boldsymbol{A}\boldsymbol{x}) = \mathcal{L}_1(\boldsymbol{x})\boldsymbol{A} - \mathcal{L}_2(\boldsymbol{A}\boldsymbol{x})$;

(ii) $\frac{\partial}{\partial \boldsymbol{x}}(\mathcal{L}_2(\boldsymbol{x})\boldsymbol{A}\boldsymbol{x}) = \mathcal{L}_2(\boldsymbol{x})\boldsymbol{A} - \mathcal{L}_1(\boldsymbol{A}\boldsymbol{x})$.

Proof. (i) Let

$$\boldsymbol{x} = \begin{pmatrix} \boldsymbol{v} \\ \boldsymbol{w} \end{pmatrix} \in \mathbb{R}^6, \quad \text{and} \quad \boldsymbol{A} = \begin{pmatrix} \boldsymbol{A}_{11} & \boldsymbol{A}_{12} \\ \boldsymbol{A}_{21} & \boldsymbol{A}_{22} \end{pmatrix},$$

where $\boldsymbol{v}, \boldsymbol{w} \in \mathbb{R}^3$ and each $\boldsymbol{A}_{ij} \in \mathbb{R}^{3\times3}$. Then

$$\begin{aligned}\mathcal{L}_1(\boldsymbol{x})\boldsymbol{A}\boldsymbol{x} &= \begin{pmatrix} \tilde{\boldsymbol{w}} & \boldsymbol{0} \\ \tilde{\boldsymbol{v}} & \tilde{\boldsymbol{w}} \end{pmatrix} \begin{pmatrix} \boldsymbol{A}_{11}\boldsymbol{v} + \boldsymbol{A}_{12}\boldsymbol{w} \\ \boldsymbol{A}_{21}\boldsymbol{v} + \boldsymbol{A}_{22}\boldsymbol{w} \end{pmatrix} \\ &= \begin{pmatrix} \tilde{\boldsymbol{w}}\boldsymbol{A}_{11}\boldsymbol{v} + \tilde{\boldsymbol{w}}\boldsymbol{A}_{12}\boldsymbol{w} \\ \tilde{\boldsymbol{v}}\boldsymbol{A}_{11}\boldsymbol{v} + \tilde{\boldsymbol{v}}\boldsymbol{A}_{12}\boldsymbol{w} + \tilde{\boldsymbol{w}}\boldsymbol{A}_{21}\boldsymbol{v} + \tilde{\boldsymbol{w}}\boldsymbol{A}_{22}\boldsymbol{w} \end{pmatrix}.\end{aligned}$$

Hence, using Lemma 6.1.1,

$$\begin{aligned}\frac{\partial}{\partial \boldsymbol{x}}\left(\mathcal{L}_1(\boldsymbol{x})\boldsymbol{A}\boldsymbol{x}\right) &= \begin{pmatrix} \tilde{\boldsymbol{w}}\boldsymbol{A}_{11} & -\widetilde{\boldsymbol{A}_{11}\boldsymbol{v}} + \tilde{\boldsymbol{w}}\boldsymbol{A}_{12} - \widetilde{\boldsymbol{A}_{12}\boldsymbol{w}} \\ \tilde{\boldsymbol{v}}\boldsymbol{A}_{11} - \widetilde{\boldsymbol{A}_{11}\boldsymbol{v}} - \widetilde{\boldsymbol{A}_{12}\boldsymbol{w}} + \tilde{\boldsymbol{w}}\boldsymbol{A}_{21} & \tilde{\boldsymbol{v}}\boldsymbol{A}_{12} - \widetilde{\boldsymbol{A}_{21}\boldsymbol{v}} + \tilde{\boldsymbol{w}}\boldsymbol{A}_{22} - \widetilde{\boldsymbol{A}_{22}\boldsymbol{w}} \end{pmatrix} \\ &= \begin{pmatrix} \tilde{\boldsymbol{w}}\boldsymbol{A}_{11} & \tilde{\boldsymbol{w}}\boldsymbol{A}_{12} \\ \tilde{\boldsymbol{v}}\boldsymbol{A}_{11} + \tilde{\boldsymbol{w}}\boldsymbol{A}_{21} & \tilde{\boldsymbol{v}}\boldsymbol{A}_{12} + \tilde{\boldsymbol{w}}\boldsymbol{A}_{22} \end{pmatrix} \\ &\quad - \begin{pmatrix} \boldsymbol{0} & [\boldsymbol{A}_{11}\widetilde{\boldsymbol{v} + \boldsymbol{A}}_{12}\boldsymbol{w}] \\ [\boldsymbol{A}_{11}\widetilde{\boldsymbol{v} + \boldsymbol{A}}_{12}\boldsymbol{w}] & [\boldsymbol{A}_{21}\widetilde{\boldsymbol{v} + \boldsymbol{A}}_{22}\boldsymbol{w}] \end{pmatrix}.\end{aligned}$$

Recalling the definitions (6.2) of $\mathcal{L}_1, \mathcal{L}_2$, the above equality can be written

$$\frac{\partial}{\partial \boldsymbol{x}}\left(\mathcal{L}_1(\boldsymbol{x})\boldsymbol{A}\boldsymbol{x}\right) = \mathcal{L}_1(\boldsymbol{x})\boldsymbol{A} - \mathcal{L}_2(\boldsymbol{A}\boldsymbol{x}).$$

(ii) Similar to (i) note that,

$$\begin{aligned}\mathcal{L}_2(\boldsymbol{x})\boldsymbol{A}\boldsymbol{x} &= \begin{pmatrix} \boldsymbol{0} & \tilde{\boldsymbol{v}} \\ \tilde{\boldsymbol{v}} & \tilde{\boldsymbol{w}} \end{pmatrix} \begin{pmatrix} \boldsymbol{A}_{11}\boldsymbol{v} + \boldsymbol{A}_{12}\boldsymbol{w} \\ \boldsymbol{A}_{21}\boldsymbol{v} + \boldsymbol{A}_{22}\boldsymbol{w} \end{pmatrix} \\ &= \begin{pmatrix} \tilde{\boldsymbol{v}}\boldsymbol{A}_{21}\boldsymbol{v} + \tilde{\boldsymbol{v}}\boldsymbol{A}_{22}\boldsymbol{w} \\ \tilde{\boldsymbol{v}}\boldsymbol{A}_{11}\boldsymbol{v} + \tilde{\boldsymbol{v}}\boldsymbol{A}_{12}\boldsymbol{w} + \tilde{\boldsymbol{w}}\boldsymbol{A}_{21}\boldsymbol{v} + \tilde{\boldsymbol{w}}\boldsymbol{A}_{22}\boldsymbol{w} \end{pmatrix}.\end{aligned}$$

Using Lemma 6.1.1,

$$
\begin{aligned}
\frac{\partial}{\partial \boldsymbol{x}}\left(\mathcal{L}_2(\boldsymbol{x})\boldsymbol{A}\boldsymbol{x}\right) &= \begin{pmatrix} \tilde{\boldsymbol{v}}\boldsymbol{A}_{21} - \widetilde{\boldsymbol{A}_{21}\boldsymbol{v}} - \widetilde{\boldsymbol{A}_{22}\boldsymbol{w}} & \tilde{\boldsymbol{v}}\boldsymbol{A}_{22} \\ \tilde{\boldsymbol{v}}\boldsymbol{A}_{11} - \widetilde{\boldsymbol{A}_{11}\boldsymbol{v}} - \widetilde{\boldsymbol{A}_{12}\boldsymbol{w}} + \tilde{\boldsymbol{w}}\boldsymbol{A}_{21} & \tilde{\boldsymbol{v}}\boldsymbol{A}_{12} - \widetilde{\boldsymbol{A}_{21}\boldsymbol{v}} + \tilde{\boldsymbol{w}}\boldsymbol{A}_{22} - \widetilde{\boldsymbol{A}_{22}\boldsymbol{w}} \end{pmatrix} \\
&= \begin{pmatrix} \tilde{\boldsymbol{v}}\boldsymbol{A}_{21} & \tilde{\boldsymbol{v}}\boldsymbol{A}_{22} \\ \tilde{\boldsymbol{v}}\boldsymbol{A}_{11} + \tilde{\boldsymbol{w}}\boldsymbol{A}_{21} & \tilde{\boldsymbol{v}}\boldsymbol{A}_{12} + \tilde{\boldsymbol{w}}\boldsymbol{A}_{22} \end{pmatrix} \\
&\qquad - \begin{pmatrix} [\widetilde{\boldsymbol{A}_{21}\boldsymbol{v} + \boldsymbol{A}_{22}\boldsymbol{w}}] & \boldsymbol{0} \\ [\widetilde{\boldsymbol{A}_{11}\boldsymbol{v} + \boldsymbol{A}_{12}\boldsymbol{w}}] & [\widetilde{\boldsymbol{A}_{21}\boldsymbol{v} + \boldsymbol{A}_{22}\boldsymbol{w}}] \end{pmatrix}.
\end{aligned}
$$

Again, by (6.2), it follows that

$$
\frac{\partial}{\partial \boldsymbol{x}}\left(\mathcal{L}_2(\boldsymbol{x})\boldsymbol{A}\boldsymbol{x}\right) = \mathcal{L}_2(\boldsymbol{x})\boldsymbol{A} - \mathcal{L}_1(\boldsymbol{A}\boldsymbol{x}).
$$

□

Aerodynamic forcing acts on the PDE via both quadratic and bilinear (in $\boldsymbol{x}_1$ and $\boldsymbol{\lambda}$) terms. For this reason, it will be convenient to derive expressions for the Jacobians of general quadratic expressions.

Lemma 6.1.3. *Suppose that $\boldsymbol{x} \in \mathbb{R}^6$ and let $\boldsymbol{A} : \mathbb{R}^6 \to \mathbb{R}^{6\times 6}$ be a linear operator given by*

$$
\boldsymbol{A}(\boldsymbol{x}) := \sum_{k=1}^{6} x_k \boldsymbol{A}^{(k)}
$$

for some $\boldsymbol{A}^{(k)} = (a_{ij}^{(k)})_{ij} \in \mathbb{R}^{6\times 6}$, $k = 1, \ldots, 6$. Then

$$
\frac{\partial}{\partial \boldsymbol{x}}\boldsymbol{A}(\boldsymbol{x})\boldsymbol{x} = \sum_{k=1}^{6} x_k \boldsymbol{Q}^{(k)} = \begin{pmatrix} \boldsymbol{A}^{(1)} & \cdots & \boldsymbol{A}^{(6)} \end{pmatrix} (\boldsymbol{I}_6 \otimes \boldsymbol{x}) + \boldsymbol{A}(\boldsymbol{x}),
$$

where $\boldsymbol{Q}^{(k)} = (a_{ik}^{(j)} + a_{ij}^{(k)})_{ij} \in \mathbb{R}^{6\times 6}$, $k = 1, \ldots, 6$.

Proof. For each $i = 1, \ldots, 6$,

$$(\boldsymbol{A}(\boldsymbol{x})(\boldsymbol{x}))_i = \sum_{j,k=1}^{6} x_k a_{ij}^{(k)} x_j \Rightarrow \frac{\partial}{\partial x_\ell}(\boldsymbol{A}(\boldsymbol{x})\boldsymbol{x})_i = \sum_{j=1}^{6} a_{ij}^{(\ell)} x_j + \sum_{k=1}^{6} x_k a_{i\ell}^{(k)}$$

Now,

$$\left[\sum_{k=1}^{6} x_k a_{i\ell}^{(k)}\right]_{i,\ell=1}^{6} = \boldsymbol{A}(\boldsymbol{x}),$$

and

$$\begin{aligned}\left[\sum_{j=1}^{6} a_{ij}^{(\ell)} x_j\right]_{i,\ell=1}^{6} &= \begin{pmatrix}\boldsymbol{A}^{(1)}\boldsymbol{x} & \cdots & \boldsymbol{A}^{(6)}\boldsymbol{x}\end{pmatrix} \\ &= \begin{pmatrix}\boldsymbol{A}^{(1)} & \cdots & \boldsymbol{A}^{(6)}\end{pmatrix}(\boldsymbol{I}_6 \otimes \boldsymbol{x}),\end{aligned}$$

and the result follows. □

We now write the aerodynamic forcing term (5.10), described by the operator $\mathcal{A}_1$ in this form.

Lemma 6.1.4. *The aerodynamic forcing $\mathcal{A}_1(\boldsymbol{x}_1)\boldsymbol{x}_1$ can be expressed*

$$\mathcal{A}_1(\boldsymbol{x}_1)\boldsymbol{x}_1 = \sum_{k=1}^{6} (\boldsymbol{x}_1)_k \boldsymbol{A}_1^{(k)} \boldsymbol{x}_1$$

for matrices $\boldsymbol{A}_1^{(1)} = \boldsymbol{A}_1^{(4)} = \boldsymbol{A}_1^{(5)} = \boldsymbol{A}_1^{(6)} = 0$,

$$\boldsymbol{A}_1^{(2)} := \begin{pmatrix} 0 & 0 & 0 & 0 & 0 & 0 \\ 0 & -C_{D0} & -C_{L0} & 0 & 0 & 0 \\ 0 & C_{L0} & 0 & b(1-\xi_{ea})\frac{C_{L\alpha}}{2} & 0 & 0 \\ 0 & b(2C_{M0}+\xi_{ea}C_{L0}) & 0 & b^2(\xi_{ea}-\xi_{ea}^2-\frac{1}{2})\frac{C_{L\alpha}}{2} & 0 & 0 \\ 0 & 0 & 0 & 0 & 0 & 0 \\ 0 & 0 & 0 & 0 & 0 & 0 \end{pmatrix}$$

and

$$\boldsymbol{A}_1^{(3)} := \begin{pmatrix} 0 & 0 & 0 & 0 & 0 & 0 \\ 0 & 0 & \frac{C_{L\alpha}}{2} & -b(1-\xi_{ea})\frac{C_{L\alpha}}{2} & 0 & 0 \\ 0 & -\left(\frac{C_{L\alpha}}{2}+C_{D0}\right) & 0 & 0 & 0 & 0 \\ 0 & -\xi_{ea}b\frac{C_{L\alpha}}{2} & 0 & 0 & 0 & 0 \\ 0 & 0 & 0 & 0 & 0 & 0 \\ 0 & 0 & 0 & 0 & 0 & 0 \end{pmatrix}$$

Furthermore,

$$\frac{\partial}{\partial \boldsymbol{x}_1}\left(\mathcal{A}_1(\boldsymbol{x}_1)\boldsymbol{x}_1\right) = \mathcal{A}_1(\boldsymbol{x}_1) + \begin{pmatrix} \boldsymbol{0} & \boldsymbol{A}_1^{(2)} & \boldsymbol{A}_1^{(3)} & \boldsymbol{0} & \boldsymbol{0} & \boldsymbol{0} \end{pmatrix} (\boldsymbol{I}_6 \otimes \boldsymbol{x}_1)$$

Proof. Follows from (5.10) and Lemma 6.1.3. □

6.2 Equilibrium Under Constant Aerodynamic Forcing

In this section, we seek to develop fast computational methods of finding equilibrium points of the PDE (5.12), which corresponds to finding $\boldsymbol{x}_1, \boldsymbol{x}_2$ and $\boldsymbol{\lambda}$ satisfying

$$\begin{aligned}
\frac{\partial \boldsymbol{x}_2}{\partial s} &= -\boldsymbol{E}\boldsymbol{x}_2 + \mathcal{L}_1(\boldsymbol{x}_1)\boldsymbol{M}\boldsymbol{x}_1 + \mathcal{L}_2(\boldsymbol{x}_2)\boldsymbol{C}\boldsymbol{x}_2 \\
&\qquad - \rho b \mathcal{A}_1(\boldsymbol{x}_1)\boldsymbol{x}_1 - \rho b \left[V_\infty \mathcal{A}_2 \boldsymbol{x}_1\right]\left[\boldsymbol{\kappa}_{AE}^\top \boldsymbol{\lambda}\right] - \sum_{l=1}^{n_{fl}} \rho b \mathcal{A}_3(\boldsymbol{x}_1)\boldsymbol{x}_1 S_\beta^l(s)\beta^l, \\
\frac{\partial \boldsymbol{x}_1}{\partial s} &= \boldsymbol{E}^\top \boldsymbol{x_1} - \mathcal{L}_1(\boldsymbol{x}_1)^\top \boldsymbol{C}\boldsymbol{x}_2, \\
V_\infty \boldsymbol{\epsilon}\boldsymbol{\lambda} &= \left[\boldsymbol{\kappa}_1^\top \boldsymbol{x}_1\right]\boldsymbol{1}, \\
\boldsymbol{x}_1(0,t) &= V_\infty \begin{pmatrix} \boldsymbol{e}_2 \\ \boldsymbol{0} \end{pmatrix}, \\
\boldsymbol{x}_2(L,t) &= \boldsymbol{0},
\end{aligned} \tag{6.3}$$

for given flight conditions ρ, V_∞, and flap inputs β^l. In equilibrium, it is therefore possible to eliminate $\boldsymbol{\lambda}$ to obtain

$$\begin{aligned}
\frac{V_\infty b_j^{AE}\lambda_j}{b} = \boldsymbol{\kappa}_1^\top \boldsymbol{x}_1 \Rightarrow \boldsymbol{\kappa}_{AE}^\top \boldsymbol{\lambda} &= \sum_{j=1}^{n_{in}} 2a_j^{AE} b_j^{AE} \lambda_j \\
&= \frac{b\boldsymbol{\kappa}_1^\top \boldsymbol{x}_1}{V_\infty} \sum_{j=1}^{n_{in}} 2a_j^{AE} \\
&= \frac{b\boldsymbol{\kappa}_1^\top \boldsymbol{x}_1}{V_\infty},
\end{aligned}$$

since, as stated in Section 5.2, $\sum_j a_j^{AE} = \frac{1}{2}$. Substituting this expression into the momentum equation implies that we are required to solve

$$\begin{aligned}\frac{\partial \boldsymbol{x}_1}{\partial s} &= \boldsymbol{E}^\top \boldsymbol{x_1} - \mathcal{L}_1(\boldsymbol{x}_1)^\top \boldsymbol{C}\boldsymbol{x}_2,\\ \frac{\partial \boldsymbol{x}_2}{\partial s} &= -\boldsymbol{E}\boldsymbol{x}_2 + \mathcal{L}_1(\boldsymbol{x}_1)\boldsymbol{M}\boldsymbol{x}_1 + \mathcal{L}_2(\boldsymbol{x}_2)\boldsymbol{C}\boldsymbol{x}_2\\ &\qquad - \rho b \mathcal{A}_1(\boldsymbol{x}_1)\boldsymbol{x}_1 - \rho b^2 \left[\mathcal{A}_2\boldsymbol{x}_1\right]\left[\boldsymbol{\kappa}_1^\top \boldsymbol{x}_1\right] - \sum_{l=1}^{n_{fl}} \rho b \mathcal{A}_3(\boldsymbol{x}_1)\boldsymbol{x}_1 S_\beta^l(s)\beta^l,\end{aligned} \tag{6.4}$$

with the appropriate boundary conditions.

Lemma 6.2.1. *The aerodynamic forcing* $\left[\mathcal{A}_2\boldsymbol{x}_1\right]\left[\boldsymbol{\kappa}_1^\top \boldsymbol{x}_1\right]$ *can be expressed as*

$$\left[\mathcal{A}_2\boldsymbol{x}_1\right]\left[\boldsymbol{\kappa}_1^\top \boldsymbol{x}_1\right] = \sum_{k=1}^{k} (\boldsymbol{x}_1)_k \boldsymbol{A}_2^{(k)} \boldsymbol{x}_1$$

for matrices $\boldsymbol{A}_2^{(1)} = \boldsymbol{A}_2^{(4)} = \boldsymbol{A}_2^{(5)} = \boldsymbol{A}_2^{(6)} = 0$,

$$\boldsymbol{A}_2^{(2)} := \frac{1}{2} C_{L\alpha} \begin{pmatrix} 0 \\ 0 \\ 1 \\ \xi_{ea} b \\ 0 \\ 0 \end{pmatrix} \boldsymbol{\kappa}_1^\top, \quad \textit{and} \quad \boldsymbol{A}_2^{(3)} := \frac{1}{2} C_{L\alpha} \begin{pmatrix} 0 \\ -1 \\ 0 \\ 0 \\ 0 \\ 0 \end{pmatrix} \boldsymbol{\kappa}_1^\top.$$

Furthermore,

$$\frac{\partial}{\partial \boldsymbol{x}_1}\left(\left[\mathcal{A}_2\boldsymbol{x}_1\right]\left[\boldsymbol{\kappa}_1^\top \boldsymbol{x}_1\right]\right) = \sum_{k=2}^{3} (\boldsymbol{x}_1)_k \boldsymbol{A}_2^{(k)} + \begin{pmatrix} \boldsymbol{0} & \boldsymbol{A}_2^{(2)} & \boldsymbol{A}_2^{(3)} & \boldsymbol{0} & \boldsymbol{0} & \boldsymbol{0} \end{pmatrix} (\boldsymbol{I}_6 \otimes \boldsymbol{x}_1)$$

Proof. Follows from (5.11) and Lemma 6.1.3. □

Lemma 6.2.2. *The control input shape function* $\mathcal{A}_3(\boldsymbol{x}_1)\boldsymbol{x}_1$ *can be expressed*

$$\mathcal{A}_3(\boldsymbol{x}_1)\boldsymbol{x}_1 = (\boldsymbol{x}_1)_2 \boldsymbol{A}_3^{(2)} \boldsymbol{x}_1$$

where

$$\boldsymbol{A}_3^{(2)} := \mathcal{A}_3(\boldsymbol{x}_1) := \begin{pmatrix} 0 & 0 & 0 & 0 & 0 & 0 \\ 0 & 0 & -C_{L\beta} & 0 & 0 & 0 \\ 0 & C_{L\beta} & 0 & 0 & 0 & 0 \\ 0 & (\xi_{ea} b C_{L\beta} + 2bC_{M\beta}) & 0 & 0 & 0 & 0 \\ 0 & 0 & 0 & 0 & 0 & 0 \\ 0 & 0 & 0 & 0 & 0 & 0 \end{pmatrix}$$

Furthermore,

$$\frac{\partial}{\partial \boldsymbol{x}_1}\left(\mathcal{A}_3(\boldsymbol{x}_1)\boldsymbol{x}_1\right) = (\boldsymbol{x}_1)_2 A_3(\boldsymbol{x}_1) + \begin{pmatrix} \mathbf{0} & \boldsymbol{A}_3^{(2)} & \mathbf{0} & \mathbf{0} & \mathbf{0} & \mathbf{0} \end{pmatrix} (\boldsymbol{I}_6 \otimes \boldsymbol{x}_1)$$

Proof. Follows from (5.33) and Lemma 6.1.3. □

We now rearrange the equilibrium condition equation (6.4) in the form

$$\frac{d\boldsymbol{x}}{ds} = \boldsymbol{G}(\boldsymbol{x}), \qquad \boldsymbol{x} = \begin{pmatrix} \boldsymbol{x}_1 \\ \boldsymbol{x}_2 \end{pmatrix},$$

where $\boldsymbol{G} : \mathbb{R}^{12} \to \mathbb{R}^{12}$ is the operator

$$\boldsymbol{G}(\boldsymbol{x}) := \begin{pmatrix} \boldsymbol{G}_1(\boldsymbol{x}) \\ \boldsymbol{G}_2(\boldsymbol{x}), \end{pmatrix} \tag{6.5}$$

with

$$\boldsymbol{G}_1(\boldsymbol{x}) := \boldsymbol{E}^\top \boldsymbol{x_1} - \mathcal{L}_1(\boldsymbol{x}_1)^\top \boldsymbol{C}\boldsymbol{x}_2,$$

and

$$\begin{aligned}\boldsymbol{G}_2(\boldsymbol{x}) := &-\boldsymbol{E}\boldsymbol{x}_2 + \mathcal{L}_1(\boldsymbol{x}_1)\boldsymbol{M}\boldsymbol{x}_1 + \mathcal{L}_2(\boldsymbol{x}_2)\boldsymbol{C}\boldsymbol{x}_2 \\ &\qquad - \rho b\mathcal{A}_1(\boldsymbol{x}_1)\boldsymbol{x}_1 - \rho b^2\left[\mathcal{A}_2\boldsymbol{x}_1\right]\left[\boldsymbol{\kappa}_1^\top\boldsymbol{x}_1\right] - \sum_{l=1}^{n_{fl}} \rho b\mathcal{A}_3(\boldsymbol{x}_1)\boldsymbol{x}_1 S_\beta^l(s)\beta^l.\end{aligned}$$

We can now write down an analytical expression for the Jacobian of $\boldsymbol{G}$.

Proposition 6.2.3. *Consider the quadratic mapping $\boldsymbol{G} : \mathbb{R}^{12} \to \mathbb{R}^{12}$ given by* (6.5). *Then*

$$\frac{\partial \boldsymbol{G}}{\partial \boldsymbol{x}} = \left(\begin{array}{c|c} \boldsymbol{E}^\top + \mathcal{L}_1(\boldsymbol{C}\boldsymbol{x}_2)^\top & -\mathcal{L}_1(\boldsymbol{x}_1)^\top\boldsymbol{C} \\ \hline \mathcal{L}_1(\boldsymbol{x}_1)\boldsymbol{M} - \mathcal{L}_2(\boldsymbol{M}\boldsymbol{x}_1) - \rho b\boldsymbol{B}(\boldsymbol{x}_1) - \rho b\boldsymbol{B}_\beta(\boldsymbol{x}_1)\beta & -\boldsymbol{E} + \mathcal{L}_2(\boldsymbol{x}_2)\boldsymbol{C} - \mathcal{L}_1(\boldsymbol{C}\boldsymbol{x}_2) \end{array}\right),$$

where

$$\begin{aligned}\boldsymbol{B}(\boldsymbol{x}_1) = &\sum_{j=2}^{3}(\boldsymbol{x}_1)_j\left(\boldsymbol{A}_1^{(j)} + b\boldsymbol{A}_2^{(j)}\right) \\ &\qquad + \begin{pmatrix}\boldsymbol{0} & \boldsymbol{A}_1^{(2)} + b\boldsymbol{A}_2^{(2)} & \boldsymbol{A}_1^{(3)} + b\boldsymbol{A}_2^{(3)} & \boldsymbol{0} & \boldsymbol{0} & \boldsymbol{0}\end{pmatrix}(\boldsymbol{I}_6 \otimes \boldsymbol{x}_1)\end{aligned}$$

and

$$\boldsymbol{B}_\beta(\boldsymbol{x}_1) := (\boldsymbol{x}_1)_3 A_3^{(2)} + \begin{pmatrix}\boldsymbol{0} & \boldsymbol{A}_3^{(2)} & \boldsymbol{0} & \boldsymbol{0} & \boldsymbol{0} & \boldsymbol{0}\end{pmatrix}(\boldsymbol{I}_6 \otimes \boldsymbol{x}_1).$$

Proof. Follows from Lemmas 6.1.2, 6.1.4, 6.2.1 and 6.2.2. □

6.2.1 Sensitivity of $\boldsymbol{x}_2(L)$ to $\boldsymbol{x}_2(0)$

In order to efficiently compute an equilibrium position for a geometrically non-linear wing corresponding to a given constant flap deflection distribution $\beta(s)$ and uniform free-stream velocity V_∞, it is useful to develop a closed-form expression for the dependence of the tip forces and moments $\boldsymbol{x}_2(L)$ upon the respective values at the root. To this end, consider a discretised state vector

$$\boldsymbol{X} := \begin{pmatrix} \boldsymbol{x}(s_1) \\ \vdots \\ \boldsymbol{x}(s_{n_{sp}}) \end{pmatrix} \in \mathbb{R}^{12n_{sp}} \tag{6.6}$$

corresponding to nodal values along the wing span

$$s_i := \frac{iL}{n_{sp}}, \qquad i = 0, \ldots, n_{sp}.$$

It is assumed that the boundary condition at the root is given by

$$\boldsymbol{x}(s_0) = \boldsymbol{x}(0) = \begin{pmatrix} V_\infty \boldsymbol{e}_2 \\ \boldsymbol{0}_3 \\ \boldsymbol{x}_2(0) \end{pmatrix} \in \mathbb{R}^{12}, \qquad \boldsymbol{x}_2(0) = \begin{pmatrix} p_1 \\ \vdots \\ p_6 \end{pmatrix}$$

and we consider $\boldsymbol{p} = (p_i) \in \mathbb{R}^6$, the reactions at the support, as a vector of unknown parameters.

Theorem 6.2.4. *Suppose that a solution $\boldsymbol{x}(s)$ to* (6.4) *is known which satisfies the root boundary condition*

$$\boldsymbol{x}(0) = \begin{pmatrix} \boldsymbol{x}_1^0 \\ \boldsymbol{p} \end{pmatrix}$$

where $\boldsymbol{x}_1^0 \in \mathbb{R}^6$ is known and fixed, and $\boldsymbol{p} \in \mathbb{R}^6$. Consider $F(\boldsymbol{X}) := \boldsymbol{x}_2(L) \in \mathbb{R}^6$. Then

$$\frac{dF}{d\boldsymbol{p}} \approx \left[\prod_{i=1}^{n_{sp}-1} \left[\boldsymbol{I} + \Delta s\, \boldsymbol{G}_{\boldsymbol{x}}(\boldsymbol{x}(s_i))\right]^\top \begin{pmatrix} \boldsymbol{0}_{6\times6} \\ \boldsymbol{I}_6 \end{pmatrix} \right]^\top \begin{pmatrix} -\Delta s\, \mathcal{L}_1(\boldsymbol{x}_1^0)^\top \boldsymbol{C} \\ \boldsymbol{I} - \Delta s \left[\boldsymbol{E} - \mathcal{L}_2(\boldsymbol{p})\boldsymbol{C} + \mathcal{L}_1(\boldsymbol{C}\boldsymbol{p})\right] \end{pmatrix}. \tag{6.7}$$

where $s_i = iL/n_{sp}, \Delta s := L/n_{sp}$ and $\boldsymbol{G}_{\boldsymbol{x}}$ is given by Proposition 6.2.3.

Proof. Suppose, for simplicity, that $F(\boldsymbol{X}) = (\boldsymbol{x}_2)_j$, for $1 \leq j \leq 6$. To approximate the

Jacobian, assume that the ODE is approximated using a forward-Euler scheme such that

$$\boldsymbol{x}(s_{i+1}) = \boldsymbol{x}(s_i) + \Delta s \boldsymbol{G}(\boldsymbol{x}(s_i)), \qquad i = 0, \dots, n_{sp} - 1,$$

where $\Delta s := L/n_{sp}$ and $\boldsymbol{G}$ is defined as in (6.5). Now, satisfying the ODE is equivalent to

$$\boldsymbol{H}(\boldsymbol{X}, \boldsymbol{p}) := \begin{pmatrix} \boldsymbol{I} & \boldsymbol{0} & \cdots & \cdots & \boldsymbol{0} \\ -\boldsymbol{I} & \boldsymbol{I} & \boldsymbol{0} & \cdots & \boldsymbol{0} \\ \boldsymbol{0} & \ddots & \ddots & & \vdots \\ \vdots & \ddots & \ddots & & \boldsymbol{0} \\ \boldsymbol{0} & \cdots & \boldsymbol{0} & -\boldsymbol{I} & \boldsymbol{I} \end{pmatrix} \begin{pmatrix} \boldsymbol{x}(s_1) \\ \boldsymbol{x}(s_2) \\ \vdots \\ \vdots \\ \boldsymbol{x}(s_{n_{sp}}) \end{pmatrix} - \Delta s \begin{pmatrix} \boldsymbol{G}(\boldsymbol{x}(s_0)) \\ \boldsymbol{G}(\boldsymbol{x}(s_1)) \\ \vdots \\ \vdots \\ \boldsymbol{G}(\boldsymbol{x}(s_{n_{sp}-1})) \end{pmatrix} - \begin{pmatrix} \boldsymbol{x}(s_0) \\ \boldsymbol{0} \\ \vdots \\ \vdots \\ \boldsymbol{0} \end{pmatrix} = \boldsymbol{0} \tag{6.8}$$

where $\boldsymbol{X}$ is given by (6.6) and

$$\boldsymbol{x}(s_0) = \begin{pmatrix} V_\infty \boldsymbol{e}_2 \\ \boldsymbol{0}_3 \\ \boldsymbol{p} \end{pmatrix},$$

with $\boldsymbol{e}_2 \in \mathbb{R}^3$. To compute $\frac{\partial F}{\partial \boldsymbol{p}}$ consider the Lagrangian

$$\mathcal{L}(\boldsymbol{X}, \boldsymbol{p}) := F(\boldsymbol{X}) + \boldsymbol{\mu}^\top \boldsymbol{H}(\boldsymbol{X}, \boldsymbol{p})$$

where $\boldsymbol{\mu} \in \mathbb{R}^{12 n_{sp}}$ is a vector of Lagrange multipliers. Then

$$\begin{aligned} \frac{dF}{d\boldsymbol{p}} = \frac{d\mathcal{L}}{d\boldsymbol{p}} &= \frac{\partial F}{\partial \boldsymbol{X}} \frac{d\boldsymbol{X}}{d\boldsymbol{p}} + \left(\frac{d\boldsymbol{\mu}}{d\boldsymbol{p}}\right)^\top \boldsymbol{H} + \boldsymbol{\mu}^\top \left(\frac{\partial \boldsymbol{H}}{\partial \boldsymbol{X}} \frac{d\boldsymbol{X}}{d\boldsymbol{p}} + \frac{\partial \boldsymbol{H}}{\partial \boldsymbol{p}}\right) \\ (\text{since } \boldsymbol{H} \equiv 0) \qquad &= \left(\frac{\partial F}{\partial \boldsymbol{X}} + \boldsymbol{\mu}^\top \frac{\partial \boldsymbol{H}}{\partial \boldsymbol{X}}\right) \frac{d\boldsymbol{X}}{d\boldsymbol{p}} + \boldsymbol{\mu}^\top \frac{\partial \boldsymbol{H}}{\partial \boldsymbol{p}}. \end{aligned}$$

We are free to choose the multiplier $\boldsymbol{\mu}$, and a judicious choice is for it to be the solution of the linear system of equations

$$\left(\frac{\partial \boldsymbol{H}}{\partial \boldsymbol{X}}\right)^\top \boldsymbol{\mu} = -\left(\frac{\partial F}{\partial \boldsymbol{X}}\right)^\top. \tag{6.9}$$

Consequently,

$$\frac{dF}{d\boldsymbol{p}} = \boldsymbol{\mu}^\top \frac{\partial \boldsymbol{H}}{\partial \boldsymbol{p}}. \tag{6.10}$$

Now, differentiating (6.8) implies that

$$\left(\frac{\partial \boldsymbol{H}}{\partial \boldsymbol{X}}\right)^\top = \begin{pmatrix} \boldsymbol{I} & \boldsymbol{0} & \cdots & & \cdots & \boldsymbol{0} \\ -[\boldsymbol{I} + \Delta s\, \boldsymbol{G}_{\boldsymbol{x}}(\boldsymbol{x}(s_1))] & \boldsymbol{I} & \boldsymbol{0} & & \cdots & \boldsymbol{0} \\ \boldsymbol{0} & \ddots & \ddots & & & \vdots \\ \vdots & \ddots & \ddots & & & \boldsymbol{0} \\ \boldsymbol{0} & \cdots & \boldsymbol{0} & -[\boldsymbol{I} + \Delta s\, \boldsymbol{G}_{\boldsymbol{x}}(\boldsymbol{x}(s_{n_{sp}-1}))] & & \boldsymbol{I} \end{pmatrix}^\top$$

and

$$\left(\frac{\partial F}{\partial \boldsymbol{X}}\right)^\top = \begin{pmatrix} \boldsymbol{0} \\ \vdots \\ \boldsymbol{0} \\ \boldsymbol{0}_6 \\ \boldsymbol{e}_j \end{pmatrix}$$

Letting $\mu = \begin{pmatrix} \boldsymbol{\mu}_1^\top & \cdots & \boldsymbol{\mu}_{n_{sp}}^\top \end{pmatrix}^\top$ we obtain an analytical expression for the solution to (6.9):

$$\boldsymbol{\mu}_{n_{sp}} = -\begin{pmatrix} \boldsymbol{0}_6 \\ \boldsymbol{e}_j \end{pmatrix} \Rightarrow \boldsymbol{\mu}_j = \left[\prod_{i=j}^{n_{sp}-1} [\boldsymbol{I} + \Delta s\, \boldsymbol{G}_{\boldsymbol{x}}(\boldsymbol{x}(s_i))]^\top\right] \boldsymbol{\mu}_{n_{sp}}.$$

To calculate the Jacobian of F, it therefore remains to compute the derivative of $\boldsymbol{H}$ with respect to the parameter vector $\boldsymbol{p}$. To this end, note that

$$\boldsymbol{G}(\boldsymbol{x}(s_0)) = \boldsymbol{G}\left(\boldsymbol{x}_1^0, \boldsymbol{p}\right) = \begin{pmatrix} \boldsymbol{G}_1\left(\boldsymbol{x}_1^0, \boldsymbol{p}\right) \\ \boldsymbol{G}_2\left(\boldsymbol{x}_1^0, \boldsymbol{p}\right) \end{pmatrix},$$

and, hence,

$$\frac{\partial \boldsymbol{H}}{\partial \boldsymbol{p}} = -\Delta s \begin{pmatrix} -\mathcal{L}_1(\boldsymbol{x}_1^0)^\top \boldsymbol{C} \\ -\boldsymbol{E} + \mathcal{L}_2(\boldsymbol{p})\boldsymbol{C} - \mathcal{L}_1(\boldsymbol{C}\boldsymbol{p}) \\ \boldsymbol{0} \\ \vdots \\ \boldsymbol{0} \end{pmatrix} - \begin{pmatrix} \boldsymbol{0}_6 \\ \boldsymbol{I}_6 \\ \boldsymbol{0} \\ \vdots \\ \boldsymbol{0} \end{pmatrix}.$$

Finally, using (6.10),

$$\frac{dF}{d\boldsymbol{p}} = \left[\prod_{i=1}^{n_{sp}-1} \left[\boldsymbol{I} + \Delta s\, \boldsymbol{G}_{\boldsymbol{x}}(\boldsymbol{x}(s_i))\right]^\top \begin{pmatrix} \boldsymbol{0} \\ \boldsymbol{e}_j \end{pmatrix}\right]^\top \begin{pmatrix} \Delta s\, \mathcal{L}_1(\boldsymbol{x}_1^0)^\top \boldsymbol{C} \\ \boldsymbol{I} + \Delta s\left[-\boldsymbol{E} + \mathcal{L}_2(\boldsymbol{p})\boldsymbol{C} - \mathcal{L}_1(\boldsymbol{C}\boldsymbol{p})\right] \end{pmatrix} \in \mathbb{R}^{1\times 6},$$

with $\boldsymbol{e}_j \in \mathbb{R}^6$. Hence the result follows by considering each $j = 1, \ldots, 6$. □

6.2.2 Nonlinear equilibrium evaluation

Now that the Jacobian of the tip forces and moments is known with respect to the root boundary conditions, Newton's method can be employed to efficiently calculate a steady-state solution of the nonlinear PDE (6.4). In the following, the phrase *root boundary condition* $\boldsymbol{p} \in \mathbb{R}^6$ implies that (6.4) has boundary condition

$$\boldsymbol{x}(0) = \begin{pmatrix} V_\infty \boldsymbol{e}_2 \\ \boldsymbol{0} \end{pmatrix}, \qquad \boldsymbol{x}_2(0) = \boldsymbol{p}.$$

Note that it is not necessary for the implied accuracy of the numerical scheme involved in

Algorithm 4 Find deformed equilibrium under forcing

```
inputs Root boundary condition $\boldsymbol{p}_0 \in \mathbb{R}^6$ and corresponding solution $\boldsymbol{x}^{(0)}(s)$ of (6.4); $\epsilon > 0$; and $r = 0$.
repeat
    Update root forces and moments via (6.7) and
        $$\boldsymbol{p}_{r+1} \leftarrow \boldsymbol{p}_r - \left[\frac{\partial F}{\partial \boldsymbol{x}}(\boldsymbol{p}_r)\right]^{-1} F(\boldsymbol{p}_r)$$
    Solve (6.4) with initial condition $\boldsymbol{p}_{r+1}$ to obtain $\boldsymbol{x}^{(r+1)}(s)$.
    $r \leftarrow r + 1$
until $\|\boldsymbol{x}_2^{(r)}(L)\|_2 < \epsilon$
return Deformed equilibrium $\boldsymbol{x}^{(*)}(s)$
```

the computation of $F_{\boldsymbol{x}}$, specified by n_{sp}, to be equal to the accuracy of the numerical scheme used to solve (6.4) in step 4. of Algorithm 4. Furthermore, an advantage of analytically calculating $F_{\boldsymbol{x}}$ via (6.7) is that a solution to the PDE needs only be computed once per step of the Algorithm 4. In contrast, a numerical approximation of the Jacobian would require at least 6^2 PDE solutions to be computed per Newton step.

6.3 Concluding Remarks

This Chapter begins with an efficient method of calculating derivatives of the terms in the aeroelastic PDEs introduced in (5.4). The aeroelastic model is comprised of an intrinsic beam formulation and two-dimensional aerodynamics both of which have at most quadratic non-linearities a fact that allows the derivatives to be written concisely. Subsequently, an expression for the sensitivity of the tip strains as a function of the root strains is derived. Finally, this allows for a method, expressed in Algorithm 4, to be devised for calculating the non-linear equilibrium states of the aeroelastic cantilever PDEs. This method is verified in Chapter 7 and shown to accelerate aeroelastic calculations.

Chapter 7

Cantilever Model Results

This Chapter begins with the verification of the state-space equations (5.66) derived in Chapter 5. Both the state-space model's frequency-domain and time-domain characteristics are first compared with the literature. Then the adjoint-based method for calculating the nonlinear equilibrium states of the PDEs (5.4) is verified by comparison to the steady-state solutions predicted by time-domain solutions of the state-space formulation. Subsequently, it is made evident that the adjoint-based methods are able to accelerate aeroelastic calculations.

7.1 Validation

7.1.1 Model Inputs

We have a concise state-space equation (5.66) for the time-domain response for the aeroservoelastic cantilever wing. As well as the external inputs, from the gust $w(t)$ and

Input	Description
V_∞	Free-stream velocity.
L	Span-wise length of the wing.
ρ	Density of the surrounding fluid.
b	The semi-chord length, kept constant across the span in this model.
$(a_j^{AE})_{j=1}^{n_{in}}$	Coefficients for the Wagner function finite state approximation described in (3.28).
$(b_j^{AE})_{j=1}^{n_{in}}$	Coefficients for the Wagner function finite state approximation described in (3.28).
ξ_{ea}	$\xi_{ea} b$ is the distance from the structural axis to the point in which the aerodynamic forces act. If $\xi_{ea} > 0$ it reflects an aerodynamic centre fore of the structural axis.
$C_{L\alpha}$	The vertical lift coefficient arising from changes in angle of attack.
$C_{L\beta}$	The vertical lift coefficient arising from deflection of a trailing edge surface.
$C_{M\beta}$	The pitching moment coefficient from deflection of a trailing edge surface.
$(S_\beta^l(s))_{l=1}^{n_{fl}}$	Flap shape function modeling the distribution of n_{fl} trailing edge surfaces.
$d(s)$	The span-wise spatial distribution of the gust defined in (7.3).

Table 7.1: Inputs to the aeroelastic model.

trailing edge flaps $\boldsymbol{\beta}(t)$, the model also requires the input of the parameters summarised in Table 7.1. Further to the parameters described in Table 7.1 the model requires the input of the mass matrix $\boldsymbol{M}(s)$ and compliance matrix $\boldsymbol{C}(s)$ introduced in (5.4). For this work, the beam model will be assumed to have constant span-wise properties with the following mass

Input	Description
ρA	Mass per unit length, $kg\, m^{-1}$.
$\{\rho I_i\}_{i=1}^{3}$	Moments of inertia per unit length around each axis, $kg\, m$.
$\{EA\}_{i=1}^{3}$	Elastic modulus, N
GJ	Torsional stiffness, Nm^2
$\{EI_i\}_{i=2}^{3}$	Bending stiffnesses, Nm^2.
ξ_{CG}	Distance from structural axis to the centre of gravity, m.

Table 7.2: Structural properties required.

Input	Value
ρ	$1.02\, kg\, m^{-3}$
b	$0.9144\,\mathrm{m}$
$(a_j^{AE})_{j=1}^{n_{in}}$	$[0.165, 0.335]^{\top}$
$(b_j^{AE})_{j=1}^{n_{in}}$	$[0.0455, 0.3]^{\top}$
ξ_{ea}	0.66
$C_{L\alpha}$	2π

Table 7.3: Required inputs that are fixed for the remainder of this work.

and compliance matrices,

$$\boldsymbol{M}(s) = \begin{pmatrix} \rho A & 0 & 0 & 0 & 0 & 0 \\ 0 & \rho A & 0 & 0 & 0 & 0 \\ 0 & 0 & \rho A & \xi_{CG}\rho A & 0 & 0 \\ 0 & 0 & \xi_{CG}\rho A & \rho I_1 & 0 & 0 \\ 0 & 0 & 0 & 0 & \rho I_2 & 0 \\ 0 & 0 & 0 & 0 & 0 & \rho I_3 \end{pmatrix} \tag{7.1}$$

and $\boldsymbol{C}(s) = \mathrm{diag}\{EA_1^{-1}, EA_2^{-1}, EA_3^{-1}, GJ^{-1}, EI_2^{-1}, EI_3^{-1}\}$, where the entries to these matrices are described in Table 7.2. One can see that the assumption $\boldsymbol{M}(s)\boldsymbol{x}_1^0 = \begin{pmatrix} V_\infty m_{22}(s)\boldsymbol{e}_2^{\top} & 0 \end{pmatrix}^{\top}$, made in Section 5.3 is trivial with this choice of mass matrix.

Input	Value
L	$6.096\,m$
ξ_{CG}	-0.2
ρA	$37.71\,kg\,m^{-1}$
ρI_1	$8.64\,kg\,m$
$\rho I_2, \rho I_3$	$8.64 \times 10^{-3} kg\,m$
EA_1	$1 \times 10^{10}\,N$
EA_2, EA_3	$1 \times 10^{13} N$
GJ	$0.99 \times 10^{6} Nm^2$
EI_2	$9.77 \times 10^{6} Nm^2$
EI_3	$1 \times 10^{8} Nm^2$

Table 7.4: Inputs used for the Goland wing validation.

7.1.2 Linear Stability Analysis of the Goland Cantilever Wing

In this section we compare the linear stability of the Goland wing [137] to the state-space equation (5.66) derived from the PDE (5.4). The Goland wing is a well studied benchmark for validating numerical linear aeroelastic simulations. First we define the open-loop flutter speed V_{FL} of the state-space system (5.66) as

$$V_{FL} := \sup\{V_\infty : \mathrm{Re}(\lambda_i(A(V_\infty))) < 0, \text{ for all } i = 1, \dots, n\}, \tag{7.2}$$

where $\lambda_i(A)$ is the ith eigenvalue of A. Furthermore, we define the *flutter frequency* ω_{FL} as the imaginary part of the first unstable eigenvalue, corresponding to the flutter speed in (7.2). The inputs used in this section for the Goland wing are those in Table 7.3 and Table 7.4. Note the inputs in Table 7.3 are fixed for the remainder of this work. Implementation of the current code, on the Goland wing, produced a flutter speed and frequency of $V_{FL} = 140\,ms^{-1}$ and $\omega_{FL} = 69.8\,s^{-1}$, which are compared with the literature in Table 7.5. One can see there is excellent agreement with models using an intrinsic beam formulation and 2D aerodynamics. The major factor that explains the higher flutter velocity in the models using UVLM is that they account for tip effects and apparent mass, hence, UVLM models experience less

Author	Model Type	$V_{FL}\, ms^{-1}$	$\omega_{FL}\, s^{-1}$
Current	Intrinsic / 2D aero	140	69.8
Palacios [135]	Intrinsic / 2D aero	141	69.8
Wang [138]	Intrinsic / 2D aero	139	70.0
Wang [139]	Intrinsic / UVLM	164	-
Murua [140]	Displacement / UVLM	165	69

Table 7.5: Flutter velocity and frequency for the Goland wing with $n_{mo} = 8$ and $n_{sp} = 60$.

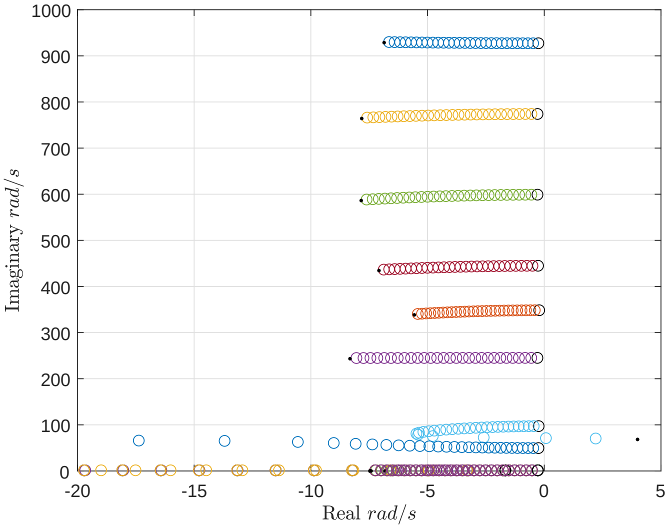

Figure 7.1: Root locus of the linear Goland wing with $n_{mo} = 8$ and $n_{sp} = 60$. Free-stream velocity from $5ms^{-1}$ to $150ms^{-1}$ in $5ms^{-1}$ increments.

aerodynamic forcing over the span of wing. Figure 7.1 is a plot of the eigenvalues, with positive imaginary part, of the Goland wing calculated with the current code with $n_{mo} = 8$. With the exception of one mode the real parts of the eigenvalues decrease as the free-stream velocity V_∞ increases. The said exception initially follows the same pattern with $\text{Re}(\lambda_i)$ decreasing up until $V_\infty \approx 120\, ms^{-1}$ after which $\text{Re}(\lambda_i)$ is observed to increase, eventually becomes unstable—causing flutter. When comparing 7.1 with [135, Figure 4] one can see that in both Figures each eigenvalue starts on the imaginary axis with similar frequencies and follows the same trajectory. This includes the eigenvalues corresponding to the aerodynamic states that lie exclusively on the real axis.

Input	Value
V_∞	$28\,ms^{-1}$
L	$30.48\,m$
ξ_{CG}	0.2

Table 7.6: Input exceptions for Section 7.1.3.

7.1.3 Time domain solutions with gust input

In the previous section we were able to show the current model's frequency response agrees well with the literature . In this section we validate time-domain solutions due to external gust inputs. Furthermore, as this work is motivated by the need for more robust aeroservoelastic modelling to facilitate the design of HALE aircraft we extend the validation from the Goland wing, which has an aspect ratio of 3.33, to the *Long-Goland wing*, a cantilever wing with the same cross-section but an aspect ratio of 16.67 as done by Simpson et al. [62]. The inputs to the state-space formulation (5.66) are the same as Section 7.1.2 with the exceptions to those stated in Table 7.6. Note the centre of gravity has been moved to a more stable position, akin to investigations in Chapter 4, Section 4.3.2, to avoid flutter. The gust input used in this case is a typical "$1 - \cos$" gust, i.e.

$$w(t) = \begin{cases} \frac{w_0}{2}\left(1 - \cos\left(\frac{2\pi V_\infty}{L_{GU}} t\right)\right) & 0 \le t \le \frac{L_{GU}}{V_\infty} \\ 0 & \text{otherwise} \end{cases}, \tag{7.3}$$

with $L_{GU} = 20\,m$ and $w_0 = 17.07\,ms^{-1}$.

The current implementation is compared with that studied in Simpson et al. [62] who combined the same intrinsic structural model used in this work with an unsteady vortex lattice method that was capable of capturing unsteady, three dimensional flow around a deforming aircraft. They published time-domain results of a linearised model which we use

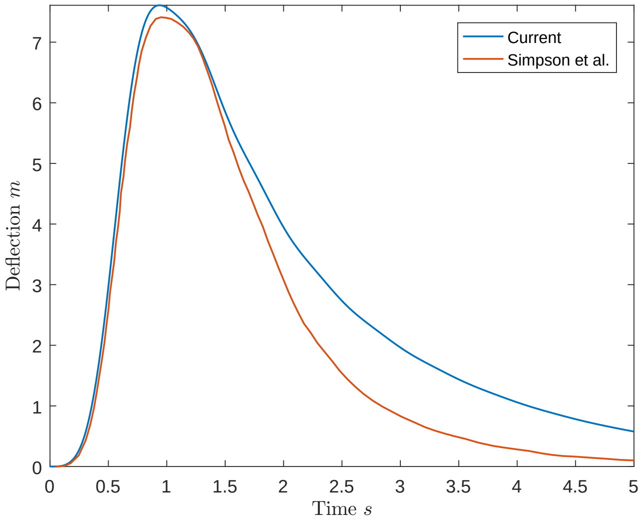

Figure 7.2: Tip displacement of the Long-Goland wing due to gust input described in (7.3), with $L_{GU} = 20\,m$ and $w_0 = 17.07\,ms^{-1}$. The blue line is the current implementation and the red line is taken from Figure 11 by Simpson et al. [62].

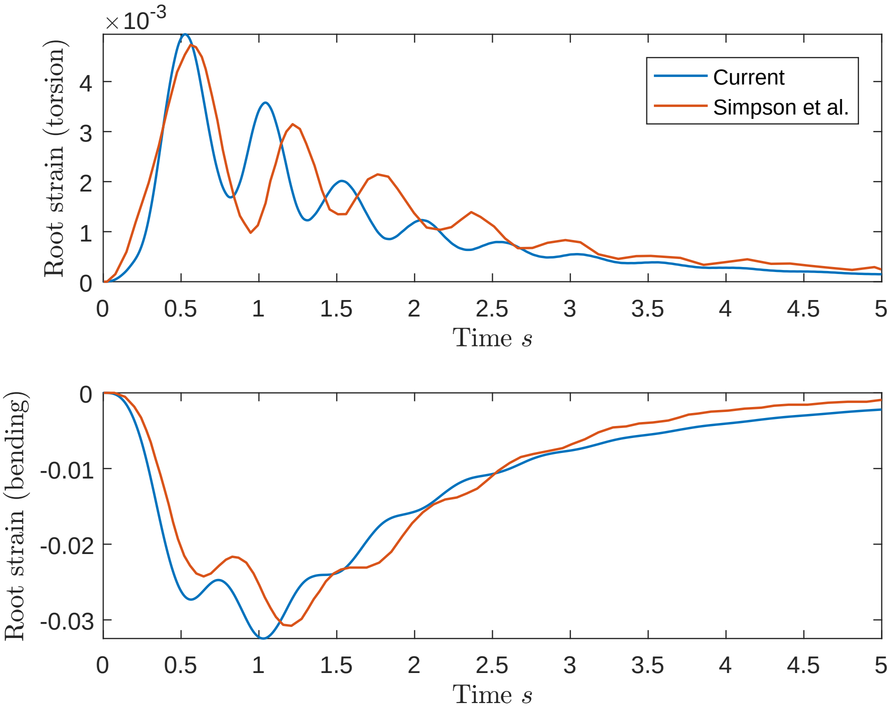

Figure 7.3: Root strains of the Long-Goland wing due to gust input described in (7.3), with $L_{GU} = 20\,m$ and $w_0 = 17.07\,ms^{-1}$. The blue line is the current implementation and the red line is taken from Figure 12 by Simpson et al. [62].

for comparison in Figures 7.2 and 7.3. The initial response, where the unsteadiness of the gust is weaker, matches closely. Furthermore, there is excellent agreement on the magnitude of the responses. Moreover, a slightly larger response amplitude from the current model is expected since our model does not account for tip effects, hence, the wing overall experiences more lift for any given input—compared to [62] where tip effects are present. Note that Figure 7.2 depicts the displacement in the $\boldsymbol{e}_z$ — defined in Chapter 5, Figure 5.1 — direction, which is not a direct output of the solution to (5.66). Instead one must first use (5.36) to return the values for $\boldsymbol{x}_1(s,t)$ and $\boldsymbol{x}_2(s,t)$ then use an integration scheme to recover the displacement $\boldsymbol{r}(s,t)$. To recover the displacement $\boldsymbol{r}(s,t) \in \mathbb{R}^3$ and rotation matrix $\boldsymbol{T}(s,t) \in \mathbb{R}^{3\times3}$, defined in (5.2), we choose to integrate the strains $\boldsymbol{C}\boldsymbol{x}_2$ in space. First define

$$\begin{pmatrix} \boldsymbol{\gamma}(s,t) \\ \boldsymbol{\kappa}(s,t) \end{pmatrix} := \boldsymbol{C}\boldsymbol{x}_2(s,t), \tag{7.4}$$

then we can relate the strains, displacements and rotations by

$$\frac{d\boldsymbol{T}}{ds} = \boldsymbol{T}\tilde{\boldsymbol{\kappa}}, \tag{7.5}$$

$$\frac{d\boldsymbol{r}}{ds} = \boldsymbol{T}\left(\boldsymbol{\gamma} + \boldsymbol{e}_1\right). \tag{7.6}$$

This can now be numerically integrated with the additional fact that we know that $\boldsymbol{r}(0,t) = -V_\infty t\boldsymbol{e}_y$ and $\boldsymbol{T}(0,t) = \boldsymbol{I}_3 \in \mathbb{R}^{3\times3}$. To clarify, the disagreement between these results due to the modeling choices and not due to lack of convergence of the current modelling. To verify this both the discretisation in space and time $(\Delta s, \Delta t)$ were investigated by considering the time integral of the tip displacement response in Figure 7.2, i.e. $I = \int_0^5 \boldsymbol{r}_3(L,t)\,dt$. Denoting an approximation of I using the discretisation $(\Delta s, \Delta t)$ as $\tilde{I}(\Delta s, \Delta t)$ it was found that $\left|\frac{\tilde{I}(1.016,0.005) - \tilde{I}(0.508,0.001)}{\tilde{I}(0.508,0.001)}\right| = 0.019$. Hence, it was determined that the discretisation (0.508,0.001) lead to sufficiently converged solutions and that the disagreement in Figure

7.2 is not due to lack of convergence. This discretisation was used for the remainder of this Chapter.

7.1.4 Adjoint-based validation

In this section we compare the time-domain solutions validated in Chapter 5 with the results obtained using Algorithm 4. For comparison, the Long-Goland wing is used, from Chapter 5 Section 7.1.3, with the addition of a trailing edge flap. The properties of the control surface are

$$S^1_\beta(s) = \begin{cases} 0 & 0 \leq s < 0.8L, \\ \\ 1 & 0.8L \leq s \leq L, \end{cases} \qquad C_{L\beta} = 5.3768, \quad C_{M\beta} = -0.4340. \tag{7.7}$$

These values for $C_{L\beta}$ and $C_{M\beta}$ are chosen using linear lift theory, described in [37, Chapter 5], and choosing a flap size of $0.2b$ in the $\boldsymbol{e}_y$ direction, which was illustrated in Figure 5.1. Assuming (5.66) is linearly stable it will converge to an equilibrium state. This equilibrium state can therefore found by direct numerical simulation. The Matlab function `ode45` is employed here, with a time step $\Delta t = 0.001\,s$, to that effect. Specifically we use Algorithm 5 to find the equilibrium state using time-domain solutions of the state-space formulation from Chapter 5. Using Algorithm 5 with inputs $\epsilon = 0.1$, $\boldsymbol{q}_0 = \boldsymbol{0} \in \mathbb{R}^n$ and $t_f = 5\,s$ the equilibrium displacement in the $\boldsymbol{e}_3$ direction was calculated and compared in Figure 7.4 against that calculated using the adjoint method, detailed in Algorithm 4. Algorithm 5 was designed to facilitate calculation of an equilibrium state with no prior knowledge. The process of updating $\boldsymbol{q}_0$ helps reduce oscillations around the equilibrium when starting simulations from states significantly different to the equilibrium state. One can see, in Figure 7.4, both methods agree very well for a range of flap deflections. Figure 7.4 can be seen as further validation for the linearised time-domain modeling of the PDE (5.4) and validation

Algorithm 5 Finding equilibrium under forcing using time-domain solution

```
inputs $(\beta^l)_{l=1}^{n_{fl}}$; $\epsilon > 0$; $\boldsymbol{q}_0$; $t_f$.
repeat
    Solve (5.66) with ode45 from $t = 0\,s$ to $t = t_f\,s$ and initial condition $\boldsymbol{q}(0) = \boldsymbol{q}_0$ to obtain $q(t_f)$.
    $\boldsymbol{q}_0 \leftarrow \boldsymbol{q}(t_f)$
    .
until $\|\boldsymbol{q}_0 - \boldsymbol{q}(t_f)\|_2 < \epsilon$
return Deformed equilibrium $\boldsymbol{x}_1^{(*)}(s) = \sum_{g=1}^{n_{mo}} \varphi_{1g}(s) q_{1g}(t_f)$ and $\boldsymbol{x}_2^{(*)}(s) = \sum_{g=1}^{n_{mo}} \varphi_{2g}(s) q_{2g}(t_f)$.
```

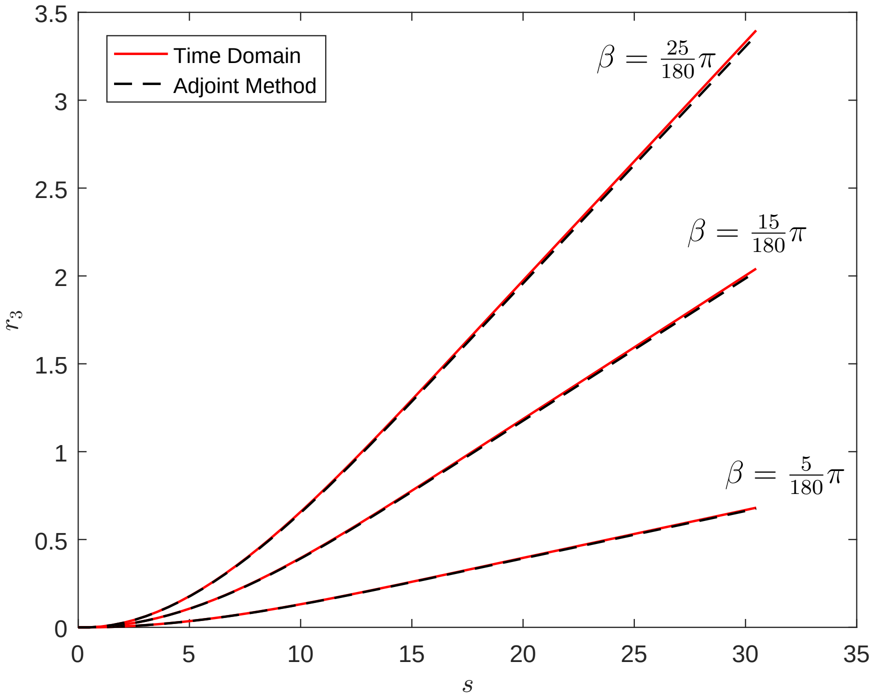

Figure 7.4: Steady state displacement in the $\boldsymbol{e}_3$ direction over the span of Long-Goland wing due to the control surface defined in (7.1.4) with deflection β.

for Algorithm 4—along with the gradients used in Theorem 6.2.4. It might seem unintuitive that results from Algorithm 5 and 4 should agree so well since the time-domain is a linearised ODE compared to the non-linear equilibrium solution obtained using the adjoint method. However, this is explained since some of the structural nonlinearities are in fact captured when integrating to recover $\boldsymbol{r}(s,t)$ and the local rotation matrix $\boldsymbol{T}(s,t)$. Furthermore, one can see that the agreement slightly worsens as β is increased. Since the geometric stiffening should be captured one would expect if a more complex flap deflection was inputed the disagreement might increase since the control surface forcing, defined in (5.34) is represented by a quadratic non-linearity. To investigate this claim an additional control surface has been considered, defined by

$$S_\beta^2(s) = \begin{cases} 0 & 0 \le s < 0.4L \\ 1 & 0.4L \le s < 0.6L \\ 0 & 0.6L \le s \le L \end{cases} \qquad C_{L\beta} = 5.3768, \quad C_{M\beta} = -0.4340. \tag{7.8}$$

We define *wing-1* as a wing with only one flap, S^1 with deflection angle $\beta^1 = \frac{1}{180}\pi$; and define *wing-2* as a wing with two flaps, S^1 and S^2 with deflection angles $\beta^1 = \frac{-5}{180}\pi$ and $\beta^2 = \frac{15}{180}\pi$, respectively. Comparing the two wings, in Figure 7.5, one can indeed see a larger relative difference in the methods for *wing-2*.

7.2 Acceleration from Adjoint-Based Method

In this Section, we demonstrate using *wing-1*, defined in Section 7.1.4, how adjoint-based methods can accelerate aeroelastic calculations. Firstly, we define the total elastic energy of the cantilever wing as

$$U = \int_0^L \boldsymbol{x}_2^\top C \boldsymbol{x}_2 \, ds, \tag{7.9}$$

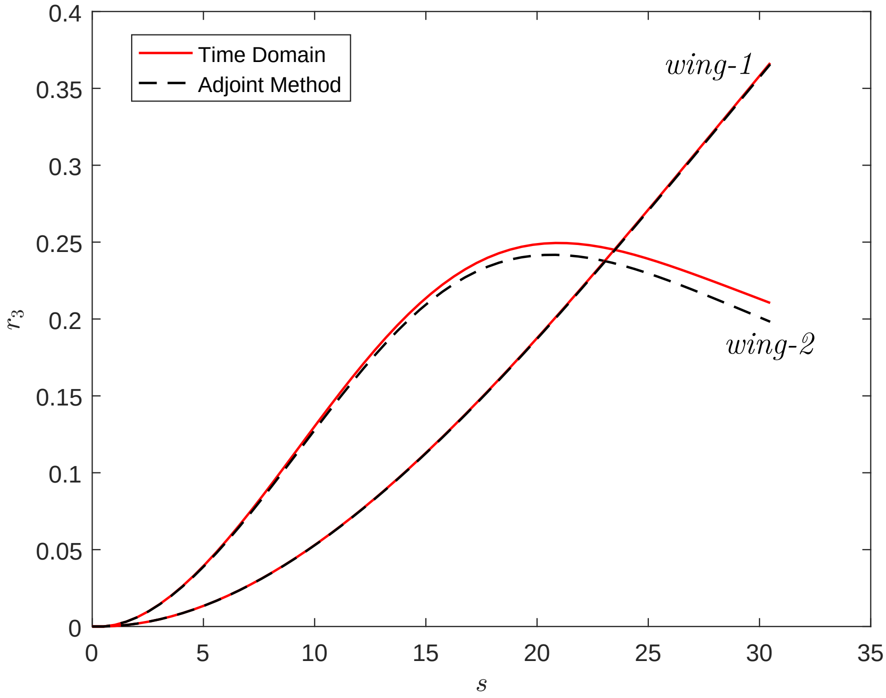

Figure 7.5: Steady state displacement in the $\boldsymbol{e}_3$ direction over the span of the Long-Goland *wing-1* and *wing-2*.

where $\boldsymbol{x}_2$ and C are the strains and compliance matrix, respectively, first introduced in Chapter 5, Section 5.1. Elastic energy arises as a structure deforms. Furthermore, all structures have a limit to how much they be deformed until their properties are irreversibly changed or at worst catastrophic failure occurs. Hence, a desire to measure the amount of deformation is often found in aeroelastic design optimisations. Here we compute the elastic energy of *wing-1* in its equilibrium deformation as a function of the deflection β in control surface S^1_β, defined in (7.1.4), i.e. a fixed deflection is chosen and the elastic energy of the subsequent steady state solution is found. The elastic energy was calculated over a range of deflections from $-10°$ to $10°$ using both the time-domain method described in Algorithm 5 and the adjoint based method described in Chapter 6, Algorithm 4. One can see, in Figure 7.6, the methods agree very well, however, as shown in Table 7.7 the adjoint-based method was able calculate the elastic energy in less time. Specifically, the time-domain method 2.4 times the time to

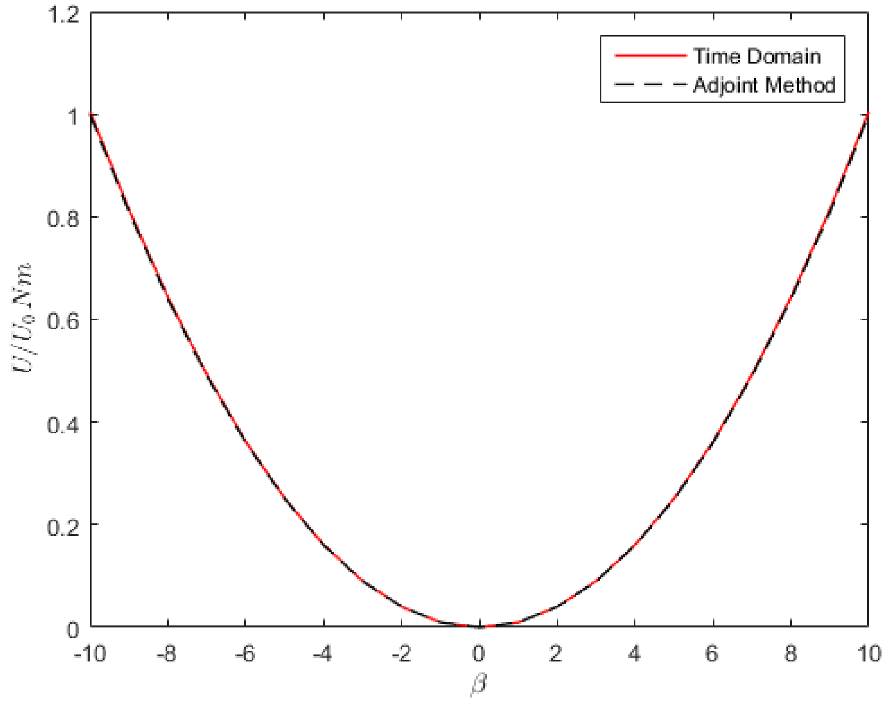

Figure 7.6: Elastic energy across *wing-1* given a flap deflection β in degrees—normalised by U_0 the elastic energy that occurs with $\beta = 10°$.

	Time-domain (s)	Adjoint-based (s)
Total time for Figure 7.6	30.9	13.1
Average time per deflection angle	2.8	1.2
Maximum time for a deflection angle	3.5	1.4

Table 7.7: Time differences between time-domain method and adjoint-based method.

calculate the elastic energy for each deflection angle in Figure 7.6. Hence, if a gradient-based design optimisation, with d design variables, required to numerically calculate the gradient of elastic energy choosing the adjoint-based method would be a factor of approximately $2d \times 2.4$ quicker than the time-domain method, due to at least 2 function evaluations being required per design variable for a gradient approximation.

7.3 Concluding Remarks

This Chapter has has shown both the state-space formulation, detailed in Chapter 5, and the adjoint-based method for solving the non-linear equilibrium equations have been verified. Verification of the state-space formulation was first achieved on the open-loop aeroelastic system with the linear stability analysis of the Goland wing. The aeroelastic state-space system, under the influence of a gust input, was then solved in the time-domain with root-strain and tip-displacement responses. The results agreed with the literature and any differences were explained by the differences in the aerodynamic model.

The adjoint-based method and the control surface input were verified by comparing the steady-state solutions calculated by the adjoint-based method to that computed using time-domain methods on the linear, state-space formulation. The equilibrium configurations matched well for the cantilever wing with only one control surface, especially for relatively smaller deflection angles. Yet, as the adjoint-based method was able to calculate the non-linear equilibrium states, which was not possible with the linearised state-space formulation, agreement worsened slightly when more control surface forcing was present. This is because the control surface forcing enters the problem with a quadratic term and hence during the linearisation of the state-space formulation some of this forcing is lost. Finally, we demonstrate how adjoint-based methods can accelerate aeroelastic computations and in this example were able to show computational time was more than halved when an adjoint-based method was chosen.

Chapter 8

Conclusion

We end on a chapter that outlines the accomplishments of this work. Firstly, a summary of this document is presented in Section 8.1. The key contributions from this work are then analysed in Section 8.2. While we have engaged with the open research questions proposed in Section 1.2 this work has also highlighted new unanswered questions. Hence, the chapter finishes with a discussion on relevant future work that would advance this research further.

8.1 Summary

A computationally minimalistic controlled aeroelastic model has been designed to facilitate a full aeroservoelastic design optimisation. Specifically, design variables were available from each sub-discipline, namely, the aerodynamics, structural mechanics and control architecture (including observer dynamics). This work defined simultaneous optimisation as concurrent optimisation of the plant, control hardware and control laws, as opposed to sequential optimisation that initially designs and fixes the plant, only to subsequently add the control design. We have exploited our minimalistic model as a test bed for aeroservoelastic design optimisation. Firstly, it was shown that simultaneous optimisation strategies did differ significantly with sequential strategies. However, interestingly, the benefits of a simultaneous optimisation were not guaranteed to outweigh the associate disadvantages, such as, the increase complexity and dimensionality of the design space. The model was also used to evaluate novel simultaneous optimisation strategies. A problem independent method for reparameterising and temporarily reducing the dimensionality of the design vector is investigated. It was observed that the optimisation trajectories were affected not only by the variable prioritisation technique but also the reparametrisation in isolation.

The aeroservoelastic system used in the first half of this work consists of a thin aerofoil that is mounted on springs. The aerodynamics are modeled as an unsteady two dimensional flow around a camberline that can undergo arbitrary deformations. The ability to approximate the force on a deforming camberline supports the modelling of a compliant trailing edge, which is used as a control surface. The introduction of aerodynamic states allows the unsteady forces to be projected onto a finite space and, hence, the equations of motion can be written in a state-space formulation. We also include an external vertical gust input that is used to initiate time-domain responses. The trailing edge control surface is used for observer based feedback regulated by pressure difference readings along the camberline. The control and observer gains are calculated from Riccati equations defined by a LQG problem, although, the control input is saturated to introduce a physical limit on the performance of the controller. This model allows the selection of optimisation variables from the three aeroservoelastic fields, specifically we chose: the shape of the trailing edge to allow for the design of the aerodynamic characteristics, which is not commonly possible with a camberline model; the structural properties of the supporting linear springs and the compliant trailing edge;

design of both the control hardware and software with the location of two pressure-difference sensors and the state-weightings withing the LQG definition.

Initially, after the aeroelastic system was verified, a reduced design optimisation problem was investigated that minimised a proxy for mass constrained to the system being open-loop stable. It was observed that the connectedness of the design space affected the performance of a gradient based optimiser. An ill-connected design space was also discovered to limit the efficacy of a frequency-domain constraint, used to reduce the number of designs with divergent responses due to the control saturation. This motivated the choice of using a cost-function with both a static metric and a time-domain metric that integrated over the heave and pitch responses caused by a series of discrete gusts. In addition to this cost-function the full aeroservoelastic design optimisation was finally defined with a constraint on the closed-loop linear stability and bounds on the design vector, such as pressure-difference sensors must be on the aerofoil. A comparison is made between simultaneous and sequential design optimisation strategies at different free-stream velocities. It was recorded that for higher velocities the simultaneous methodology was able to improve the cost-function by a further 8%, compared with the sequential method. However, it was observed that the simultaneous method took up to a factor of 7 times the number of cost-function evaluations to converge and also suffered from greater sensitivity to initial conditions. Furthermore, the simultaneous method was not guaranteed to outperform the sequential method. This was demonstrated at lower velocities where the simultaneous method was less beneficial. Specifically, at the lowest velocity tested the sequential method converged to designs with a lower cost-function than the simultaneous method and required fewer function evaluations. Since the available aerodynamic force the control surface can generate increases with the free-stream velocity this also corresponds to an increase in control authority, i.e. increase the control architecture's ability to affect the aerofoil's performance. Thus, at high velocities the benefits of including the control design immediately outweigh the negatives of increasing the dimensionality of the design optimisation. The higher velocity simultaneous designs were characterised by aerofoils with a centre of mass further aft, an attribute that causes a decrease in open-loop stability. Yet, with closed-loop control this decrease in stability increases performance since the controller is able to affect the system-states at a quicker rate, specifically, we demonstrate that such a design can reject a gust input faster. A sequential method would not have obtained this solution since it first optimises the open-loop system in which a more forward centre of mass would decrease open-loop performance.

The aerofoil model is finally used to investigate the parametrisation and variable selection methods based on proper orthogonal decomposition that were outlined in Chapter 2. In order to study these two methods, relatively large sets of random initial design vectors were generated so numerous optimisation trajectories could be compared. Both methods were able to reduce undesirable features of a simultaneous optimisation strategy, namely, they decreased the sensitivity to the initial conditions. Additionally, they converged to designs with better performance (cost-function reduction of 2% and 4% for the parametrisation and variable selection technique, respectively) while needing fewer cost-function evaluations (28.4% and 37.5% respectively).

In the second half of the work another, more physically realisable, aeroelastic model is introduced. The model includes a geometrically-nonlinear, slender-beam that can be displaced and rotated in three dimensional space; an unsteady two-dimensional flow over a thin, symmetric plate; trailing edge flaps that can be varied in number, size and position; and a vertical, quasi-steady gust input. The beam is clamped at one end and moves at a constant velocity. The equations of motion for the geometrically-nonlinear beam are written in the intrinsic formulation, i.e. the primary state-variables are the velocities and strains. This results in a PDE with, at most, quadratic nonlinearities, which was taken advantage of later in the work to efficiently compute analytic sensitivities. So that time-domain responses to gust inputs could be investigated the coupled aerodynamic and structural equation of motion are reduced into a state-space formulation. This is achieved by linearising the PDEs around a steady forward flight condition. Firstly, the solutions in the time-domain were compared, and verified, to responses in the literature. Subsequently, the time-domain solution was used to calculate forward flight equilibrium states, i.e. flights conditions, such as, free-stream velocity, control surface location and control surface deflection were fixed and the steady-state solution found. These equilibrium states were compared to those calculated via an adjoint-based method. The adjoint-based method was derived from the original, pre-linearised, PDEs that includes up to quadratic nonlinearities. Analytic expressions for the derivatives of each term in the PDEs were calculated and an expression for the sensitivity of the wing-tip strains was derived as a function of the wing-root strains. This expression allowed for efficient calculation of the nonlinear equilibrium states that agreed well with the time-domain solutions—with only slight divergence for increased control surface forcing. Finally, a demonstration of how adjoint-based methods can accelerate aeroelastic calculations is included. The total elastic energy of a wing in equilibrium is calculated, for a range of control surface deflections, via both the time-domain method and adjoint-based method. The results from these methods are in agreement but the adjoint-based methods required less than half the time for computation.

8.2 Significant Contributions

1. Minimalistic ASE model for simultaneous design optimisation investigations

At the start of this work, in Section 1.2, we introduced four *Open Research Questions*. In order to address **Question 1** a controlled aeroelastic model was created (and verified) that allows the design of variables from aerodynamics, structural mechanics and control theory. In order to minimise the computational burden we chose to model a simple aerofoil with a two dimensional, potential flow about a camberline. However, a balance between reducing model complexity and retaining a representative aeroservoelastic framework was sought so that results would still apply to more physically realistic models. We ensured that the aerofoil model remained representative to the subject of aeroservoelastic design optimisation by addressing the following:

- The inclusion of unsteady aerodynamics increased the model complexity as it required the introduction of additional aerodynamic states. However, it allowed the aeroelastic phenomena of flutter speed to be considered. Flutter is especially important to quantify in the context of studying controlled aeroelastic designs that replace structural stiffness via their control systems.
- It is not common for a design optimisation of a camberline model to include aerodynamic design variables. Yet, this was achieved in this work by the inclusion of a deforming complaint trailing edge. The trailing edge deformation is defined by the *shape function*, described in (3.52), which affects the aerodynamic forcing experienced by the aerofoil. This description allowed for the shape function to be included in the

design optimisation, allowing aerodynamic design variables to be considered. Furthermore, in-keeping with the goal to reduce computational costs we described a method to accelerate the design optimisation of the compliant trailing edge in Section 3.4.2. Note that this also pertains to **Question 5** as the modelling choice of the aerodynamics and shape function parameterisation made this acceleration possible.

- Saturation of the controller was included so nonlinear effects were present. An implication of this was that a design could be linearly stable but still have a divergent response. This necessitated the consideration of time-domain responses in the design optimisation. Note that, as mentioned in Chapter 1, more advanced time-domain methods were called for in the failure report of the 2004 NASA Helios prototype.

- Lastly, the aerofoil model permitted the design of control hardware placement via the optimisation of the location of pressure difference sensors. Normally, within the literature, control hardware considerations have only been investigated in the context of control surface position or sizing within wing models. Since calculation of the pressure difference over camberline was already a prerequisite for solving the equations of motion the addition of pressure difference sensors caused no additional computational burden but increased the number of control theory design variables available.

As stated in **Question 1**, the aerofoil model was primarily created to investigate simultaneous optimisation methods, however, it also contributed insight to **Question 2**. Upon comparisons between simultaneous and sequential optimisation methods it was established that performance improvements from using a simultaneous method, i.e. increasing the problem complexity, were not guaranteed — even though a sequential approach should be sub-optimal. This was demonstrated in Section 4.3.1 where simultaneous and sequential optimisation trajectories were compared over a range of free-stream velocities. For the highest velocities the simultaneous method did outperform the sequential method, converging on designs with a cost-function over 8% lower. Albeit, this came at the expense of requiring more cost-function evaluations and an increase to the variance in final designs. The trade-off for increasing problem complexity, using a simultaneous method as opposed to a sequential method, to gain improvements in performance was not seen for the lower velocities studied. In fact the sequential method outperformed the simultaneous method at the lowest velocities. This was likely due to the extra complexity and dimensionality of the simultaneous method meaning there were an increased number of local minima. This was especially true for lower velocities as the control variables had relatively little influence on the cost-function, i.e. the control design space was flat. But as the velocity is increased the cost-function becomes more sensitive to the control design, effectively steepening the design space so that less designs prematurely converged to low performing local minima.

2. Exploration of the use of proper orthogonal decomposition on preliminary gradient-based optimisations

Simultaneous optimisation strategies that incorporate proper orthogonal decomposition (POD) on preliminary optimisation trajectories are proposed, in Section 2.4.2, and subsequently tested, in Section 4.3, on the aerofoil model. The first strategy (Algorithm 3 with $\Lambda = 1$) results in an ordinary simultaneous optimisation but with a design vector that has been reparameterised, or more specifically rotated to align with the POD basic vectors. Section 4.3.3 is able to directly address **Question 3**, from Chapter 1, by demonstrating that improvements in optimisation trajectories are possible with our proposed POD-based reparameterisation strategy. Firstly, this method consistently converged, even for relatively lenient converging tolerances ϵ, on designs with a lower cost-function. We also showed that the reparametrisation strategy was able to reduce the number of cost-function evaluations required by 28.4% — this result is made more impressive considering that the reduction in the number of evaluations includes the extra optimisation trajectories require to form the POD *training-set*. Lastly, this method also achieves a reduction in the variance in the final designs of 22.4%. This attenuation in the sensitivity to the initial conditions could be due to the numerical conditioning, caused by aligning the design vector to the POD basis vectors, reducing optimisation trajectories prematurely terminating in local minima.

Investigation of **Question 4** was accomplished via the second POD-based strategy (Algorithm 3 with $\Lambda < 1$). This method uses POD on the same preliminary optimisation trajectories to rotate and re-order the design vector with a completely automated and problem independent manner. The new design variables are outputted in order of their priority with a weighted metric, λ_i defined in (2.13), of their importance. The dimensionality of an optimisation problem can hence be reduced by removing the least important variables. In order to reduce the dimensionality in a problem independent way our method requires an input of the minimum variance possible after removing dimensions Λ. This ensures the method is independent of the initial dimensionality. For example, the effect of reducing the dimensionality of a problem by one is likely to be significantly different in a design optimisation over three variables compared to one with fifty variables. More consistency is expected with our proposed method: removing dimensions such that an inputted fraction Λ of the variance encountered in preliminary optimisations is retained. Our reduction strategy first converges to an intermediate design, possibly only with a course tolerance condition, then restarts the optimisation from the intermediate design with the full design vector. This resulted in not only higher performing final designs but in a 37.5% reduction in the number of cost-function evaluations and a 35.3% reduction in the variance of the final designs.

3. A computational efficient procedure for nonlinear aeroelastic wing simulation

Equations of motion have been derived and verified for a cantilever wing from coupling a nonlinear-geometric beam with two dimensional potential flow models. The first formulation, described in Chapter 5, reduced the equations of motion to a state-space formulation with control surface and external gust inputs akin to the aerofoil model described and investigated in Chapter 3 and 4, respectively. We then chose to invest time on the aeroelastic solver to achieve faster solutions, further exploring **Question 5**. Our choice of the intrinsic beam formulation combined with the two dimensional aerodynamic model resulted in PDEs with at most quadratic nonlinearities. This was exploited to derive analytical expressions for the derivatives of the terms in the PDEs. As an example of the value of these analytic derivatives we devised a method for the efficient prediction of nonlinear equilibrium states. This adjoint-based method was able to accelerate aeroelastic calculation by a factor of two, compared to the time-domain method.

8.3 Recommendations for Future Work

In this final section we deliberate the author's opinion on possible future points of focus stemming from this work. Although this discussion is not exhaustive we aim to highlight and motivate several research directions that further our addition to the literature.

8.3.1 Continued exploration of POD based optimisation strategies

In answering **Question 2** we observed that one cannot guarantee that a simultaneous strategy will elicit an improvement in optimisation trajectories. Therefore, a method that could predict when a design optimisation will benefit from using a simultaneous optimisation method could save computational time and award valuable insight to the underlying model or design space. This could be possible by using the same initial steps of Algorithm 3, i.e. generated a random set of initial designs, perform optimisations from these points to create a set of optimisation trajectories, then employ POD on this training-set. This outputs the POD basis vectors $H \in \mathbb{R}^{d\times d}$ and the associated basis vector's eigenvalue λ_j, which is proportional to the variance encountered in the training-set in that direction. One could then truncate H, for example, one could use $\Lambda = 0.5$ to concentrate on the most important basis vectors $\bar{H} \in \mathbb{R}^{d\times r}$, where $r < d$. Finally, if we consider $s_i = \sum_{j=1}^{r} \bar{H}_{ij}$ for each i that is associated to a control design variable we should have a metric for how sensitive the problem is to control design. The closer s_i is to 1, since H is unitary, the more important the associated variable should be considered. Future work could investigate what practical thresholding values, for Λ and s_i, predict when a simultaneous optimisation will be beneficial.

The novel optimisation strategies we proposed could benefit from various algorithmic optimisations. However, the biggest inefficiency, in the author's opinion, is that from the preliminary optimisations only the trajectories are inputted into the POD then effectively discarded. Since a gradient-based optimiser has been used in the preliminary optimisations one also has access to global gradient information which could be used in conjunction with the POD strategy for sensitivity analysis.

Lastly, the POD strategies should be investigated on design optimisations of higher dimensionality to ensure the method scales well. Indeed the author suspects the strategies proposed will be more beneficial as the number of design variables increases. The increase in dimensionality should offer the variable prioritisation technique more freedom to identify superfluous directions of optimisation that can be at least temporarily ignored. A suitable model for increasing the number of design variables, while not significantly increasing the computational burden, is the cantilever model described in Chapters 5 and 6.

8.3.2 Design optimisation of cantilever model

Upon deriving the state-space formulation for the cantilever wing, in Chapter 5, we chose to devote time into improving the aeroelastic solver. Instead, one could have used the state-space description of a cantilever wing, from Chapter 5, for investigating aeroservoelastic design optimisation. One advantage of the cantilever model is that it allows a significant expansion of design variables, such as, the size and placement of control surfaces or the distribution of mass. A design optimisation similar to that defined in Chapters 4 and 5 could be created for the cantilever model, for example,

$$\min_{X} M_{tot}(X) + \int_{t=0}^{T} \int_{s=0}^{L} \boldsymbol{x}_2(X;s,t)^{\top} C(X) \boldsymbol{x}_2(X;s,t)\, ds dt \tag{8.1}$$

$$\text{such that } \dot{\boldsymbol{q}}(t) = A\left(X;V_\infty\right)\boldsymbol{q}(t) + \boldsymbol{B}_W(X;V_\infty)w(t) + V_\infty^2 \boldsymbol{B}_\beta(X)\boldsymbol{\beta}, \tag{8.2}$$

$$0.8V_\infty - V_F(X) \leq 0, \tag{8.3}$$

$$0 \leq X \leq 1, \tag{8.4}$$

where M_{tot} is a static metric of the total mass, (8.2) is the equation of motion for the cantilever wing derived in Section 5.6.3 and V_F is the flutter speed. An initial investigation could be to compare simultaneous and sequential methods over a range of free-stream velocities to check the results from Chapter 4 are repeatable. Furthermore, it would be interesting to obtain similar results by varying the number of control flaps rather than the free-stream velocity. Would a simultaneous optimisation strategy become more beneficial as one increased the number of control surfaces? One could then evaluate how the POD based variable prioritisation methods scale with a design optimisation of higher dimensionality.

Alternatively, further work on adjoint-based methods would also be constructive. In Section 7.2 we demonstrated how an adjoint-based method could accelerate aeroelastic calculations. Using the analytic derivatives derived in Section 6.1 this could be furthered to include more aeroelastic calculations and a framework for an adjoint-based design optimisation. One could begin by focusing on static problems, i.e. optimisation of the steady state solution, then advance to adjoint-based optimisation of dynamic problems. A basic static problem would be to minimise the root strain $\boldsymbol{x}_2(0)$ by optimisation of the deflection of given control surfaces. Using Lagrange multipliers one would constrain that the tip strain $\boldsymbol{x}_2(L) = 0$, as the cantilever boundary conditions dictate, and to physically realise the problem that the vertical component of strain was constant to model a fixed lift objective. This would require derivatives with respect to the flap deflection to be derived.

Bibliography

[1] Thomas E Noll et al. "Investigation of the Helios prototype aircraft mishap volume I mishap report". In: *Downloaded on* 9 (2004), p. 2004.

[2] Eli Livne. "Aircraft Active Flutter Suppression: State of the Art and Technology Maturation Needs". In: *Journal of Aircraft* 55.1 (Dec. 2017), pp. 410–452. ISSN: 0021-8669. DOI: `10.2514/1.C034442`. URL: `https://doi.org/10.2514/1.C034442`.

[3] Eli Livne. *Future of Airplane Aeroelasticity.* 2003. DOI: `10.2514/2.7218`.

[4] William F Milliken Jr. "Progress in dynamic stability and control research". In: *Journal of the Aeronautical Sciences* 14.9 (1947), pp. 493–519. ISSN: 1936-9956.

[5] Doug Richardson. *General Dynamics F-16.* Popular Culture Ink, 1990. ISBN: 0831714018.

[6] John David Anderson Jr. *Fundamentals of aerodynamics.* Tata McGraw-Hill Education, 2010. ISBN: 0070700125.

[7] David G Hull. *Fundamentals of airplane flight mechanics.* Springer, 2007. ISBN: 3540465715.

[8] Frederico Afonso et al. "A review on non-linear aeroelasticity of high aspect-ratio wings". In: *Progress in Aerospace Sciences* 89 (2017), pp. 40–57. ISSN: 0376-0421.

[9] Kenneth L Roger, Garold E Hodges, and Larry Felt. "Active flutter suppression-a flight test demonstration". In: *Journal of Aircraft* 12.6 (1975), pp. 551–556. ISSN: 0021-8669.

[10] Cisco. *Cisco Visual Networking Index: Global Mobile Data Traffic Forecast Update, 2016–2021 White Paper.* URL: `https://www.cisco.com/c/en/us/solutions/collateral/service-provider/visual-networking-index-vni/mobile-white-paper-c11-520862.html`.

[11] Frederic M Hoblit. *Gust loads on aircraft: concepts and applications.* Aiaa, 1988. ISBN: 1600860605.

[12] Christopher M Shearer and Carlos E S Cesnik. "Nonlinear flight dynamics of very flexible aircraft". In: *Journal of Aircraft* 44.5 (2007), pp. 1528–1545.

[13] Mayuresh Patil, Dewey Hodges, and Carlos Cesnik. "Nonlinear aeroelastic analysis of aircraft with high-aspect-ratio wings". In: *39th AIAA/ASME/ASCE/AHS/ASC Structures, Structural Dynamics, and Materials Conference and Exhibit.* Structures, Structural Dynamics, and Materials and Co-located Conferences. American Institute of Aeronautics and Astronautics, Apr. 1998.

[14] David M Schuster, D D Liu, and Lawerence J Huttsell. "Computational Aeroelasticity: Success, Progress, Challenge". In: *Journal of Aircraft* 40.5 (Sept. 2003), pp. 843–856. ISSN: 0021-8669. DOI: `10.2514/2.6875`. URL: `https://doi.org/10.2514/2.6875`.

[15] Mayuresh J Patil, Dewey H Hodges, and Carlos E S. Cesnik. "Nonlinear aeroelasticity and flight dynamics of high-altitude long-endurance aircraft". In: *Journal of Aircraft* 38.1 (2001), pp. 88–94.

[16] Carlos Cesnik and Weihua Su. "Nonlinear aeroelastic simulation of X-HALE: A very flexible UAV". In: *49th AIAA Aerospace Sciences Meeting including the New Horizons Forum and Aerospace Exposition.* 2011, p. 1226.

[17] Lars Krog et al. "Topology Optimisation of Aircraft Wing Box Ribs". In: *10th AIAA/ISSMO Multidisciplinary Analysis and Optimization Conference*. Multidisciplinary Analysis Optimization Conferences. American Institute of Aeronautics and Astronautics, Aug. 2004. DOI: `doi:10.2514/6.2004-4481`.

[18] George Keith Batchelor. *An introduction to fluid dynamics*. Cambridge university press, 2000. ISBN: 0521663962.

[19] Jeffrey P Thomas, Earl H Dowell, and Kenneth C Hall. "Modeling viscous transonic limit cycle oscillation behavior using a harmonic balance approach". In: *Journal of aircraft* 41.6 (2004), pp. 1266–1274. ISSN: 0021-8669.

[20] Chihiro Hayashi. *Nonlinear oscillations in physical systems*. Princeton University Press, 2014. ISBN: 1400852870.

[21] Joel H Ferziger and Milovan Peric. *Computational methods for fluid dynamics*. Springer Science & Business Media, 2012. ISBN: 3642560261.

[22] Wenbin Song and Andrew Keane. "A Study of Shape Parameterisation Methods for Airfoil Optimisation". In: *10th AIAA/ISSMO Multidisciplinary Analysis and Optimization Conference*. Multidisciplinary Analysis Optimization Conferences. American Institute of Aeronautics and Astronautics, Aug. 2004.

[23] Meng Wang and Parviz Moin. *Computation of trailing-edge flow and noise using large-eddy simulation*. 2000. DOI: `10.2514/3.14669`.

[24] Zhoujie Lyu, Gaetan K Kenway, and Joaquim Martins. "RANS-based Aerodynamic Shape Optimization Investigations of the Common Research Model Wing". In: *52nd Aerospace Sciences Meeting*. AIAA SciTech. American Institute of Aeronautics and Astronautics, Jan. 2014. DOI: `doi:10.2514/6.2014-0567`.

[25] Stephen B Pope. *Turbulent flows*. 2001.

[26] Shengyi Wang et al. “Turbulence modeling of deep dynamic stall at relatively low Reynolds number”. In: *Journal of Fluids and Structures* 33 (2012), pp. 191–209. ISSN: 0889-9746.

[27] Mayuresh J Patil, Dewey H Hodges, and Carlos E S Cesnik. “Limit-cycle oscillations in high-aspect-ratio wings”. In: *Journal of fluids and structures* 15.1 (2001), pp. 107–132. ISSN: 0889-9746.

[28] F Angrand. *Numerical methods for the Euler equations of fluid dynamics.* Vol. 21. SIAM, 1985. ISBN: 0898712009.

[29] Raymond M Hicks and Preston A Henne. “Wing Design by Numerical Optimization”. In: *Journal of Aircraft* 15.7 (July 1978), pp. 407–412. ISSN: 0021-8669. DOI: `10.2514/3.58379`. URL: `https://doi.org/10.2514/3.58379`.

[30] J L Hess. “Panel methods in computational fluid dynamics”. In: *Annual Review of Fluid Mechanics* 22.1 (1990), pp. 255–274. ISSN: 0066-4189.

[31] H Multhopp. *Methods for calculating the lift distribution of wings (subsonic lifting-surface theory).* Aeronautical Research Council London, 1950.

[32] P Frank Pai. *Highly flexible structures: modeling, computation, and experimentation.* AIAA (American Institute of Aeronautics & Ast, 2007. ISBN: 1563479176.

[33] Matthew Dillsaver, Carlos Cesnik, and Ilya Kolmanovsky. “Gust response sensitivity characteristics of very flexible aircraft”. In: *AIAA Atmospheric Flight Mechanics Conference.* 2012, p. 4576.

[34] Edward Albano and William P Rodden. “A doublet-lattice method for calculating lift distributions on oscillating surfaces in subsonic flows.” In: *AIAA journal* 7.2 (1969), pp. 279–285. ISSN: 0001-1452.

[35] Joseba Murua et al. “T-tail flutter: Potential-flow modelling, experimental validation and flight tests”. In: *Progress in Aerospace Sciences* 71 (2014), pp. 54–84. ISSN: 0376-0421.

[36] G D McBain. “The Vortex Lattice Method”. In: *Theory of Lift: Introductory Computational Aerodynamics in MATLAB®/OCTAVE* (2012), pp. 209–222. ISSN: 1118346165.

[37] J Katz and A Plotkin. “Low-Speed Aerodynamics Cambridge University Press”. In: *New York, NY, USA* (2001).

[38] C.-H. HSU and C E LAN. “Theory of wing rock”. In: *Journal of Aircraft* 22.10 (Oct. 1985), pp. 920–924. ISSN: 0021-8669. DOI: `10.2514/3.45225`. URL: `https://doi.org/10.2514/3.45225`.

[39] MMFC VAN GOOL, D T Mook, and A H Nayfeh. “Subsonic wing rock of slender delta wings”. In: *Journal of Aircraft* 22.3 (1985), pp. 223–228. ISSN: 0021-8669.

[40] Joseba Murua, Rafael Palacios, and J. Michael R Graham. “Applications of the unsteady vortex-lattice method in aircraft aeroelasticity and flight dynamics”. In: *Progress in Aerospace Sciences* 55 (2012), pp. 46–72.

[41] G Andersen, E Forster, and R Kolonay. “Multiple Control Surface Utilization in Active Aeroelastic Wing Technology”. In: *Journal of Aircraft* 34.4 (July 1997), pp. 552–557. DOI: `10.2514/2.2208`.

[42] Sohrab Haghighat, Joaquim R RA Martins, and Hugh H T. Liu. “Aeroservoelastic design optimization of a flexible wing”. In: *Journal of Aircraft* 49.2 (2012), pp. 432–443.

[43] Henrik Hesse and Rafael Palacios. “Reduced-order aeroelastic models for dynamics of maneuvering flexible aircraft”. In: *AIAA journal* 52.8 (2014), pp. 1717–1732. ISSN: 0001-1452.

[44] William P Rodden et al. *AERODYNAMIC INFLUENCE COEFFICIENTS FROM INCOMPRESSIBLE STRIP THEORY: ANALYTICAL DEVELOPMENT AND COMPUTATIONAL PROCEDURE*. Tech. rep. 1962.

[45] MARTIN R WASZAK and DAVID K SCHMIDT. “Flight dynamics of aeroelastic vehicles”. In: *Journal of Aircraft* 25.6 (June 1988), pp. 563–571. ISSN: 0021-8669. DOI: `10.2514/3.45623`. URL: `https://doi.org/10.2514/3.45623`.

[46] Dae-Kwan Kim et al. “An aeroelastic analysis of a flexible flapping wing using modified strip theory”. In: *Active and Passive Smart Structures and Integrated Systems 2008*. Vol. 6928. International Society for Optics and Photonics, 2008, 69281O.

[47] Enrico Cestino. “Design of solar high altitude long endurance aircraft for multi payload & operations”. In: *Aerospace Science and Technology* 10.6 (2006), pp. 541–550. DOI: `10.1016`.

[48] David A Peters, Swaminathan Karunamoorthy, and Wen-Ming Cao. “Finite state induced flow models. I-Two-dimensional thin airfoil”. In: *Journal of Aircraft* 32.2 (1995), pp. 313–322.

[49] D M Tang and E H Dowell. “Comments on the ONERA stall aerodynamic model and its impact on aeroelastic stability”. In: *Journal of Fluids and Structures* 10.4 (1996), pp. 353–366. ISSN: 0889-9746.

[50] Morten Hartvig Hansen, Mac Gaunaa, and Helge Aagaard Madsen. “A Beddoes-Leishman type dynamic stall model in state-space and indicial formulations”. In: (2004). ISSN: 8755030904.

[51] Theodore Theodorsen and W H Mutchler. “General theory of aerodynamic instability and the mechanism of flutter”. In: (1935).

[52] Herbert Wagner. “Über die Entstehung des dynamischen Auftriebes von Tragflügeln”. In: *ZAMM-Journal of Applied Mathematics and Mechanics/Zeitschrift für Angewandte Mathematik und Mechanik* 5.1 (1925), pp. 17–35. ISSN: 1521-4001.

[53] Donald L Kunz. “Survey and comparison of engineering beam theories for helicopter rotor blades”. In: *Journal of Aircraft* 31.3 (1994), pp. 473–479. ISSN: 0021-8669.

[54] Alejandro D Otero and Fernando L Ponta. “Structural analysis of wind-turbine blades by a generalized Timoshenko beam model”. In: *Journal of solar energy engineering* 132.1 (2010), p. 11015. ISSN: 0199-6231.

[55] Deman Tang and Earl H Dowell. “Experimental and theoretical study on aeroelastic response of high-aspect-ratio wings”. In: *AIAA journal* 39.8 (2001), pp. 1430–1441. ISSN: 0001-1452.

[56] Dewey H Hodges. “Geometrically exact, intrinsic theory for dynamics of curved and twisted anisotropic beams”. In: *AIAA journal* 41.6 (2003), pp. 1131–1137. ISSN: 0001-1452.

[57] Rafael Palacios, Joseba Murua, and Robert Cook. “Structural and Aerodynamic Models in Nonlinear Flight Dynamics of Very Flexible Aircraft”. In: *AIAA Journal* 48.11 (Nov. 2010), pp. 2648–2659. DOI: `10.2514/1.J050513`.

[58] Vineet Sahasrabudhe et al. “Integrated Rotor-Flight Control System Optimization with Aeroelastic and Handling Qualities Constraints”. In: *Journal of Guidance, Control, and Dynamics* 20.2 (1997), pp. 217–224. DOI: `10.2514/2.4034`.

[59] John T Batina. “Unsteady Euler algorithm with unstructured dynamic mesh for complex-aircraft aerodynamic analysis”. In: *AIAA journal* 29.3 (1991), pp. 327–333. ISSN: 0001-1452.

[60] Joseph A Garcia. “Numerical investigation of nonlinear aeroelastic effects on flexible high-aspect-ratio wings”. In: *Journal of Aircraft* 42.4 (2005), pp. 1025–1036. ISSN: 0021-8669.

[61] Dewey H Hodges. “Review of composite rotor blade modeling”. In: *AIAA journal* 28.3 (1990), pp. 561–565. ISSN: 0001-1452.

[62] Robert J Simpson et al. “Predictive control for alleviation of gust loads on very flexible aircraft”. In: *55th AIAA/ASMe/ASCE/AHS/SC Structures, Structural Dynamics, and Materials Conference*. 2014, p. 843.

[63] Weihua Su and Carlos E S. Cesnik. “Nonlinear aeroelasticity of a very flexible blended-wing-body aircraft”. In: *Journal of Aircraft* 47.5 (2010), pp. 1539–1553. ISSN: 0021-8669.

[64] Zahra Sotoudeh, Dewey H Hodges, and Chong-Seok Chang. “Validation studies for aeroelastic trim and stability of highly flexible aircraft”. In: *Journal of Aircraft* 47.4 (2010), pp. 1240–1247. ISSN: 0021-8669.

[65] Zhicun Wang et al. “Nonlinear aeroelastic analysis for a HALE wing including effects of gust and flow separation”. In: *48th AIAA/ASME/ASCE/AHS/ASC Structures, Structural Dynamics, and Materials Conference*. 2007, p. 2106.

[66] Pablo A Iglesias and Brian P Ingalls. *Control theory and systems biology*. MIT Press, 2010. ISBN: 0262013347.

[67] Suguru Arimoto. “Learning control theory for robotic motion”. In: *International Journal of Adaptive Control and Signal Processing* 4.6 (1990), pp. 543–564. ISSN: 1099-1115.

[68] Carlos E Garcia, David M Prett, and Manfred Morari. “Model predictive control: theory and practice—a survey”. In: *Automatica* 25.3 (1989), pp. 335–348. ISSN: 0005-1098.

[69] Suresh P Sethi and Gerald L Thompson. “Applications of mathematical control theory to finance: Modeling simple dynamic cash balance problems”. In: *Journal of Financial and Quantitative Analysis* 5.4-5 (1970), pp. 381–394. ISSN: 1756-6916.

[70] Alexandre Barbagallo, Denis Sipp, and Peter J Schmid. “Closed-loop control of an open cavity flow using reduced-order models”. In: *Journal of Fluid Mechanics* 641 (2009), pp. 1–50. ISSN: 1469-7645.

[71] Salvatore Maraniello, Robert J S Simpson, and Rafael Palacios. “Optimal manoeuvres with very flexible wings”. In: *57th AIAA/ASCE/AHS/ASC Structures, Structural Dynamics, and Materials Conference*. 2016, p. 1223.

[72] Jie Zeng et al. “Adaptive feedforward control for gust load alleviation”. In: *Journal of Guidance, control, and dynamics* 33.3 (2010), pp. 862–872. ISSN: 0731-5090.

[73] William L Garrard and John M Jordan. “Design of nonlinear automatic flight control systems”. In: *Automatica* 13.5 (1977), pp. 497–505. ISSN: 0005-1098.

[74] Mordechay Karpel. “Design for active flutter suppression and gust alleviation using state-space aeroelastic modeling”. In: *Journal of Aircraft* 19.3 (1982), pp. 221–227. ISSN: 0021-8669.

[75] Eli Livne. “Integrated aeroservoelastic optimization: status and direction”. In: *Journal of Aircraft* 36.1 (1999), pp. 122–145. ISSN: 0021-8669.

[76] Carlos E S Cesnik, Rafael Palacios, and Eric Y Reichenbach. “Reexamined Structural Design Procedures for Very Flexible Aircraft”. In: *Journal of Aircraft* 51.5 (2014), pp. 1580–1591. ISSN: 0021-8669.

[77] Achille Messac and James Turner. “Dual structural-control optimization of large space structures”. In: (1984).

[78] Hosam K Fathy et al. “Nested plant/controller optimization with application to combined passive/active automotive suspensions”. In: *American Control Conference, 2003. Proceedings of the 2003.* Vol. 4. IEEE, 2003, pp. 3375–3380. ISBN: 0780378962.

[79] Hosam K Fathy et al. “On the coupling between the plant and controller optimization problems”. In: *American Control Conference, 2001. Proceedings of the 2001.* Vol. 3. IEEE, 2001, pp. 1864–1869.

[80] George Platanitis and Thomas W Strganac. “Suppression of control reversal using leading-and trailing-edge control surfaces”. In: *Journal of guidance, control, and dynamics* 28.3 (2005), pp. 452–460. ISSN: 0731-5090.

[81] In Lee and Seung-Ho Kim. “Aeroelastic analysis of a flexible control surface with structural nonlinearity”. In: *Journal of Aircraft* 32.4 (1995), pp. 868–874. ISSN: 0021-8669.

[82] Miroslav Krstic, Ioannis Kanellakopoulos, and Peter V Kokotovic. *Nonlinear and adaptive control design.* Wiley, 1995. ISBN: 0471127329.

[83] Yinan Wang, Andrew Wynn, and Rafael Palacios. “Model-predictive control of flexible aircraft dynamics using nonlinear reduced-order models”. In: *57th aiaa/asce/ahs/asc structures, structural dynamics, and materials conference.* 2016, p. 711.

[84] A Da Ronch et al. “Nonlinear model reduction for flexible aircraft control design”. In: *AIAA Atmospheric Flight Mechanics Conference.* 2012, p. 4404.

[85] D Ray, R P Gokarn, and O P Sha. “A global optimization model for ship design”. In: *Computers in industry* 26 (1995), pp. 175–192.

[86] I.J. Ramirez-Rosado and J.L. Bernal-Agustin. *Genetic algorithms applied to the design of large power distribution systems.* 1998. DOI: `10.1109/59.667402`.

[87] Maria da Conceicao Cunha and Joaquim Sousa. “Water distribution network design optimization: simulated annealing approach”. In: *Journal of Water Resources Planning and Management* 125.4 (1999), pp. 215–221.

[88] A R Rao, J P Scanlan, and A J Keane. “Applying multiobjective cost and weight optimization to the initial design of turbine disks”. In: *Journal of Mechanical Design* 129.12 (2007), pp. 1303–1310.

[89] David S. Lee et al. “Aviation and global climate change in the 21st century”. In: *Atmospheric Environment* 43.22-23 (2009), pp. 3520–3537.

[90] Joyce E Penner. *Aviation and the global atmosphere: a special report of IPCC Working Groups I and III in collaboration with the Scientific Assessment Panel to the Montreal Protocol on Substances that Deplete the Ozone Layer*. Cambridge University Press, 1999.

[91] Sohrab Haghighat, Joaquim R RA Martins, and Hugh H T. Liu. “Aeroservoelastic design optimization of a flexible wing”. In: *Journal of Aircraft* 49.2 (2012), pp. 432–443. ISSN: 0021-8669.

[92] A Manan et al. “Optimization of aeroelastic composite structures using evolutionary algorithms”. In: *Engineering Optimization* 42.2 (2010), pp. 171–184. DOI: `10.1080/03052150903104358`.

[93] Changho Nam, Aditi Chattopadhyay, and Youdan Kim. “Optimal wing planform design for aeroelastic control”. In: *AIAA journal* 38.8 (2000), pp. 1465–1470.

[94] Ricardo M. Paiva, Curran Crawford, and Afzal Suleman. “Robust and Reliability-Based Design Optimization Framework for Wing Design”. In: *AIAA Journal* 52 (2014), pp. 711–724. DOI: `10.2514/1.J052161`.

[95] Peter D Dunning and H Alicia Kim. "Robust Topology Optimization: Minimization of Expected and Variance of Compliance". In: *AIAA Journal* 51.11 (Sept. 2013), pp. 2656–2664. DOI: `10.2514/1.J052183`.

[96] Shinji Suziki and Satoshi Yonezawa. "Simultaneous structure/control design optimization of a wing structure with a gust load alleviation system". en. In: *Journal of Aircraft* 30.2 (Mar. 1993), pp. 268–274.

[97] Jian Tu and Donald Jones. "Variable Screening in Metamodel Design by Cross-Validated Moving Least Squares Method". In: *44th AIAA/ASME/ASCE/AHS/ASC Structures, Structural Dynamics, and Materials Conference*. Structures, Structural Dynamics, and Materials and Co-located Conferences. American Institute of Aeronautics and Astronautics, Apr. 2003.

[98] Tiziano Ghisu et al. "Adaptive polynomial chaos for gas turbine compression systems performance analysis". In: *AIAA Journal* 48.6 (2010), pp. 1156–1170. ISSN: 0001-1452.

[99] Boris Moulin, Moshe Idan, and Mordechay Karpel. "Aeroservoelastic Structural and Control Optimization Using Robust Design Schemes". In: *Journal of Guidance, Control, and Dynamics* 25.1 (2002), pp. 152–159. DOI: `10.2514/2.4860`.

[100] Dhanaraja Kasinathan and Kirsten Morris. "Convergence of \mathcal{H}_\infty-optimal actuator locations". In: *IEEE Conference on Decision and Control and European Control Conference* (2011), pp. 627–632.

[101] Michael A Demetriou. "Robust sensor location optimization in distributed parameter systems using functional observers". In: *Decision and Control, 2005 and 2005 European Control Conference. CDC-ECC'05. 44th IEEE Conference on*. IEEE, 2005, pp. 7187–7192.

[102] Sean Wakayama. "Multidisciplinary design optimization of the blended-wing-body". In: *7th AIAA/USAF/NASA/ISSMO Symposium on Multidisciplinary Analysis and*

Optimization. Multidisciplinary Analysis Optimization Conferences. American Institute of Aeronautics and Astronautics, Sept. 1998.

[103] Wesley W Li and Chan-gi Pak. “Aeroelastic Optimization Study Based on the X-56A Model”. In: *AIAA Atmospheric Flight Mechanics Conference.* American Institute of Aeronautics and Astronautics, June 2014.

[104] Wei Shyy et al. “Recent progress in flapping wing aerodynamics and aeroelasticity”. In: *Progress in Aerospace Sciences* 46.7 (2010), pp. 284–327.

[105] Jacob J Broughton-Venner, Andrew Wynn, and Rafael Palacios. “Aeroservoelastic Optimisation of Cantilever Wings via Reparameterization and Variable Selection”. In: *under preparation* (2018).

[106] Jacob J Broughton-Venner, Andrew Wynn, and Rafael Palacios. “Aeroservoelastic Optimisation of Aerofoils with Compliant Flaps via Reparameterization and Variable Selection”. In: *AIAA Journal* 56.3 (Dec. 2017), pp. 1146–1157. ISSN: 0001-1452. DOI: `10.2514/1.J056141`. URL: `https://doi.org/10.2514/1.J056141`.

[107] Jacob J Broughton-Venner, Andrew Wynn, and Rafael Palacios. “Aeroservoelastic optimisation of an aerofoil with active compliant flap via reparametrisation and variable selection”. In: *58th AIAA/ASCE/AHS/ASC Structures, Structural Dynamics, and Materials Conference.* 2017, p. 572.

[108] Jacob J Broughton-Venner, Andrew Wynn, and Rafael Palacios. “Aeroservoelastic Optimisation of an Aerofoil with Active Compliant Flap via Reparametrisation and Variable Selection”. In: *17th AIAA/ISSMO Multidisciplinary Analysis and Optimization Conference.* 2016, p. 3511.

[109] Peter Constantin and Ciprian Foias. *Navier-stokes equations.* University of Chicago Press, 1988. ISBN: 0226115496.

[110] Björn Hübner, Elmar Walhorn, and Dieter Dinkler. "A monolithic approach to fluid–structure interaction using space–time finite elements". In: *Computer methods in applied mechanics and engineering* 193.23-26 (2004), pp. 2087–2104. ISSN: 0045-7825.

[111] Jeffrey W Banks, William D Henshaw, and Donald W Schwendeman. "An analysis of a new stable partitioned algorithm for FSI problems. Part I: Incompressible flow and elastic solids". In: *Journal of Computational Physics* 269 (2014), pp. 108–137. ISSN: 0021-9991.

[112] Hermann G Matthies and Jan Steindorf. "Partitioned strong coupling algorithms for fluid–structure interaction". In: *Computers & structures* 81.8-11 (2003), pp. 805–812. ISSN: 0045-7949.

[113] Matthias Heil, Andrew L Hazel, and Jonathan Boyle. "Solvers for large-displacement fluid–structure interaction problems: segregated versus monolithic approaches". In: *Computational Mechanics* 43.1 (2008), pp. 91–101. ISSN: 1432-0924. DOI: `10.1007/s00466-008-0270-6`. URL: `https://doi.org/10.1007/s00466-008-0270-6`.

[114] Salvatore Maraniello and Rafael Palacios. "Co-design of very flexible actuated structures". In: (2015).

[115] Isaac Tetzloff and William Crossley. "An allocation approach to investigate new aircraft concepts and technologies on fleet-level metrics". In: *9th AIAA Aviation Technology, Integration, and Operations Conference (ATIO) and Aircraft Noise and Emissions Reduction Symposium (ANERS)*. 2009, p. 6979.

[116] J K S Dillinger et al. "Stiffness optimization of composite wings with aeroelastic constraints". In: *Journal of Aircraft* 50.4 (2013), pp. 1159–1168. ISSN: 0021-8669.

[117] Yinan Wang, Wynn Andrew, and Rafael Palacios. "Nonlinear Model Reduction for Aeroelastic Control of Flexible Aircraft Described by Large Finite-Element Models". In: *55th AIAA/ASMe/ASCE/AHS/SC Structures, Structural Dynamics, and Materi-*

als Conference. AIAA SciTech. American Institute of Aeronautics and Astronautics, Jan. 2014.

[118] Brian P Danowsky et al. “Incorporation of Feedback Control into a High-Fidelity Aeroservoelastic Fighter Aircraft Model”. In: *Journal of Aircraft* 47.4 (2010), pp. 1274–1282. DOI: `10.2514/1.47119`.

[119] Jeffrey P Thomas, Earl H Dowell, and Kenneth C Hall. “Three-Dimensional Transonic Aeroelasticity Using Proper Orthogonal Decomposition-Based Reduced-Order Models”. In: *Journal of Aircraft* 40.3 (May 2003), pp. 544–551. DOI: `10.2514/2.3128`.

[120] Piergiovanni Marzocca, Liviu Librescu, and Walter Silva. “Volterra series approach for nonlinear aeroelastic response of 2-D lifting surfaces”. In: *19th AIAA Applied Aerodynamics Conference*. Fluid Dynamics and Co-located Conferences. American Institute of Aeronautics and Astronautics, June 2001. DOI: `doi:10.2514/6.2001-1459`.

[121] M Berci et al. “Multifidelity metamodel building as a route to aeroelastic optimization of flexible wings”. In: *Proceedings of the Institution of Mechanical Engineers, Part C: Journal of Mechanical Engineering Science* 225.9 (Sept. 2011), pp. 2115–2137. DOI: `10.1177`.

[122] Taehyoun Kim. “Efficient Reduced-Order System Identification for Linear Systems with Multiple Inputs”. In: *AIAA Journal* 43.7 (July 2005), pp. 1455–1464. DOI: `10.2514/1.11225`.

[123] L. Liu, E. H. Dowell, and J. P. Thomas. “A high dimensional harmonic balance approach for an aeroelastic airfoil with cubic restoring forces”. In: *Journal of Fluids and Structures* 23.3 (2007), pp. 351–363.

[124] David J Lucia, Philip S Beran, and Walter A Silva. “Aeroelastic System Development Using Proper Orthogonal Decomposition and Volterra Theory”. In: *Journal of Aircraft* 42.2 (Mar. 2005), pp. 509–518.

[125] NK-R Kevlahan, J C R Hunt, and J C Vassilicos. “A comparison of different analytical techniques for identifying structures in turbulence”. In: *Applied scientific research* 53.3-4 (1994), pp. 339–355. ISSN: 0003-6994.

[126] Lawrence Sirovich and Michael Kirby. “Low-dimensional procedure for the characterization of human faces”. In: *Josa a* 4.3 (1987), pp. 519–524. ISSN: 1520-8532.

[127] Thiemo Kier. “Comparison of unsteady aerodynamic modelling methodologies with respect to flight loads analysis”. In: *AIAA Atmospheric Flight Mechanics Conference and Exhibit.* 2005, p. 6027.

[128] Mac Gaunaa. *Unsteady 2D potential-flow forces on a thin variable geometry airfoil undergoing arbitrary motion.* 2006.

[129] T H Von Karman. “Airfoil Theory for Non-Uniform Motion”. In: *Journal of the Aeronautical Sciences* 5.10 (Aug. 1938), pp. 379–390.

[130] Robert F Stengel. *Optimal control and estimation.* Courier Corporation, 2012. ISBN: 0486134814.

[131] Thomas A Zeiler. “Results of Theodorsen and Garrick Revisited”. In: *Journal of Aircraft* 37.5 (Sept. 2000), pp. 918–920. DOI: `10.2514/2.2691`.

[132] Stanley M Shinners. *Modern control system theory and design.* John Wiley & Sons, 1998. ISBN: 0471249068.

[133] Murad Abu-Khalaf, Jie Huang, and Frank L. Lewis. *Nonlinear H2/H [infinity] constrained feedback control: a practical design approach using neural networks.* Springer Science & Business Media, 2006, p. 203. ISBN: 978-1-84628-349-9 978-1-84628-350-5.

[134] Rafael Palacios, Yinan Wang, and Moti Karpel. “Intrinsic models for nonlinear flexible-aircraft dynamics using industrial finite-element and loads packages”. In: *53rd AIAA/ASME/ASCE Structures, Structural Dynamics and Materials Conference 20th AIAA/ASME/AHS Adaptive Structures Conference 14th AIAA*. 2012, p. 1401.

[135] Rafael Palacios and Bodgan Epureanu. “An intrinsic description of the nonlinear aeroelasticity of very flexible wings”. In: *52nd AIAA/ASME/ASCE/AHS/ASC Structures, Structural Dynamics and Materials Conference 19th AIAA/ASME/AHS Adaptive Structures Conference 13t*. 2011, p. 1917.

[136] Willi-Hans Steeb and Yorick Hardy. *Matrix Calculus and Kronecker Product: A Practical Approach to Linear and Multilinear Algebra Second Edition*. World Scientific Publishing Company, 2011. ISBN: 981310807X.

[137] Martin Goland. “The flutter of a uniform cantilever wing”. In: *Journal of Applied Mechanics-Transactions of the Asme* 12.4 (1945), A197–A208. ISSN: 0021-8936.

[138] Yinan Wang, Rafael Palacios, and Andrew Wynn. “Robust aeroelastic control of very flexible wings using intrinsic models”. In: *54th AIAA/ASME/ASCE/AHS/ASC Structures, Structural Dynamics, and Materials Conference*. 2013, p. 1485.

[139] Zhicun Wang et al. “Time Domain Nonlinear Aeroelastic Analysis for HALE Wings”. In: *47th AIAA/ASME/ASCE/AHS/ASC Structures, Structural Dynamics, and Materials Conference*. Structures, Structural Dynamics, and Materials and Co-located Conferences. American Institute of Aeronautics and Astronautics, May 2006.

[140] Joseba Murua, Rafael Palacios, and John Michael Graham. “Modeling of nonlinear flexible aircraft dynamics including free-wake effects”. In: *AIAA Atmospheric Flight Mechanics Conference*. 2010, p. 8226.

Appendices

Appendix A

Transfer function from gust input to flap input

From Chapter 4 we have the closed-loop system (3.58) and observer dynamics (3.65) that we write below as

$$\begin{pmatrix} \dot{\boldsymbol{x}} \\ \dot{\hat{\boldsymbol{x}}} \end{pmatrix} = \begin{pmatrix} A & -B_uK \\ LC & A - LC - B_uK \end{pmatrix} \begin{pmatrix} \boldsymbol{x} \\ \hat{\boldsymbol{x}} \end{pmatrix} + \begin{pmatrix} B_w \\ 0 \end{pmatrix} w. \tag{A.1}$$

Performing a Laplace transformation, so that $X(s) = \mathcal{L}\{\boldsymbol{x}(t)\}$, $U(s) = \mathcal{L}\{\boldsymbol{u}(t)\}$ and $W(s) = \mathcal{L}\{\boldsymbol{w}(t)\}$, and rearranging gives

$$\begin{pmatrix} sI - A & -B_uK \\ LC & sI - (A - LC - B_uK) \end{pmatrix} \begin{pmatrix} X \\ \hat{X} \end{pmatrix} = \begin{pmatrix} B_w \\ 0 \end{pmatrix} W. \tag{A.2}$$

A final rearrangement and a pre-multiplication by $\begin{pmatrix} 0 & -K \end{pmatrix}$ gives the desired result of

$$\begin{aligned} U &= \begin{pmatrix} 0 & -K \end{pmatrix} \begin{pmatrix} sI - A & -B_u K \\ LC & sI - (A - LC - B_u K) \end{pmatrix}^{-1} \begin{pmatrix} B_w \\ 0 \end{pmatrix} W, && \text{(A.3)} \\ &:= T_{uw}(s) W. && \text{(A.4)} \end{aligned}$$